Subglacial Processes and Subglacial Hydrology

Pierre-Marie Lefeuvre

Dissertation submitted for the degree of Philosophiae Doctor (PhD)

Department of Geosciences
Faculty of Mathematics and Natural Sciences
University of Oslo

Oslo, Norway
February 2016

© Pierre-Marie Lefeuvre, 2016

Series of dissertations submitted to the
Faculty of Mathematics and Natural Sciences, University of Oslo
No. 1719

ISSN 1501-7710

All rights reserved. No part of this publication may be
reproduced or transmitted, in any form or by any means, without permission.

Cover: Hanne Baadsgaard Utigard.
Print production: Reprosentralen, University of Oslo.

Abstract

The hydrology of glaciers is known to have a significant influence on glacier dynamics. Rapid variations in dynamics can occur due to changes in the glacial and subglacial hydrology. However, our understanding of the subglacial drainage system is based on few direct and usually short-term observations.

In this thesis, two decades of pressure measurements at the glacier bed are investigated. The measurements were carried out at the Svartisen Subglacial Laboratory in Northern Norway where load cells installed at the ice-rock interface under $\sim$200 m of glacier ice record normal stress. A statistical study of the records for the period 1992-2014 demonstrates that the glacier bed response depends strongly on surface melt and the routing of subglacial water. Changes in subglacial hydrology cause several types of mechanical response at the glacier base. Water increases basal connectivity in summer whereas local processes, such as local ice flow, dominate the pressure signal in winter.

The comparison of two summers with high, but contrasting connectivity (correlated vs anti-correlated pressure signal) demonstrates that fluctuations in meltwater input force a load transfer from the connected hydrological system to the unconnected part of the drainage system. Modelling of load transfer near a pressurised channel simulates the observed anti-correlated response in normal stress at the glacier bed.

Daily pressure events are also investigated and characterise the response in pressure of the unconnected system, which differs from daily fluctuations in water pressure as measured in boreholes. The peak and decay in pressure that comprise these events are inferred to be a result of the stress bridging effect that occurs during the contraction of the drainage system. The peak in pressure is reproduced with an experiment where an artificial cavity contracts over the load cell and with a stress bridging model that incorporates shear stress transfer near a subglacial cavity.

Observations from load cells and boreholes are not contradictory; instead they complement each other and help us characterise the mechanical and hydrological dynamics occurring at the glacier bed.

Sammendrag

Det er bred enighet om at hydrologien har stor innvirkning påen isbres dynamikk. Raske variasjoner i breens dynamikk kan forekomme pågrunn av endringer av hydrologiske forhold både på, i og under breen. Vår forståelse av det subglasiale dreneringssystemet er basert på få observasjoner ofte målt i korte tidsperioder. I denne doktorgradsavhandlingen har to tiår med subglasiale trykkmålinger blitt analysert. Resultatene fra trykksensorene viser at endringer i hydrologien under breen skaper flere typer av mekaniske prosesser mellom breen og underlaget. Disse undersøkelsene har blitt gjort ved Svartisen Subglasiale Laboratorium i Nord-Norge. Under den 200 m tykke breen har trykksensorer blitt installert for å måle trykket mellom isen og berggrunnen. En statistisk analyse av trykksensordata fra perioden 1992-2014 viser at responsen langs brebunnen er sterkt påvirket av bresmelting på overflaten og hvordan dette vannet drenerer ned til bunnen. Smeltevannet øker den subglasiale responsen under breen om sommeren, men om vinteren er det lokale prosesser, for eksempel lokal bevegelse i isen, som er mest dominerende. To somre viste svært ulike trykksignaler mellom sensorene med godt korrelerte signaler en sommer og anti-korrelerte signaler den neste sommer. Dette demonstrerer at det kan utvikles ulike dreneringssystemer ved brebunnen. Smeltevannet kan både drener i et sammenkoblet system og i et mer separert, isolert, system. Modellering av trykkfordelingen nær en dreneringskanal med høyt vanntrykk kan simulere denne observerte anti-korrelerte responsen i normaltrykket fra isen mot brebunnen. Daglige istrykkvariasjoner viser en respons å vanntrykkvariasjoner i det isolerte dreneringssystemet. Trykkvariasjonene tolkes som et resultat av ”stress-bridging” (forhøyet trykk nær kanalen) som et resultat av at kanalene trekker seg sammen ved avtagende vannføring. Denne trykkøkningen nær kanalen er også observert der en kunstig utsmeltet kanal trakk seg sammen ved isdeformasjon over en trykksensor. Dette er å vist med en ”stress-bridging” modell som inkluderer skjærspenninger nær kanalen.

Observasjoner fra trykksensorer langs bunnen av breen og vanntrykkmogsålinger i borehull fra overflata er ikke motsigende, men komplementerer hverandre og hjelper oss med å beskrive mekaniske og hydrologiske prosesser ved brebunnen.

Acknowledgements

Je voudrais tout d'abord remercier ma famille qui m'a toujours soutenu et aidé pendant ses neuf longues années d'études. Vous comptez beaucoup pour moi, merci Papa, Maman, Papy, Mamy et les frérôts. Je vous dois tout.

This thesis would never have been written without the supervision and help of Miriam Jackson. I am very grateful for the time you gave me and thank you for your patience, especially at the end of the thesis. During the PhD, I have enjoyed collaborating with Thomas Zwinger. Although you were not one of my supervisor on paper, I felt that you were like one. Your advice and support during my visits to Finland and also at conferences stimulated me and boosted my work, as well as my interest for continuing modelling in the future. I also would like to express my gratitude to Jon Ove Hagen for his support and for giving me fantastic opportunities to collaborate with Scandinavian researchers and travel, I mean, work around the world. My work greatly benefited from Gaute Lappegard's research and his volunteered supervision. Our meetings substantially helped me understand the complexity of subglacial hydrology and brought me back in the right direction.

My PhD has been a long journey, and would not have been achieved without the help and friendship of my PhD fellow Alexandra Messerli. The last four years, we have stood together against the unfairness of studying a capricious nature, shared happiness and frustration of doing research, and enjoyed the PhD and outside PhD life. I owe you a lot. Two other amazing people are my PhD officemate Solveig Havstad Winsvold and PhD officemate(?) Chris Duffield. You always have been present when I needed to talk, relax, party, and work. A daily care that means a lot to me. I should not forget the magic Thomas Schellenberger (he has the talent of disappearing), the best and nicest chilled mate. Thanks also to Bas Altena, Paul Leclercq, Felix Matt, and all the others from the physical geography group at the University of Oslo, and the ones sitting in the basement.

I also would like to acknowledge the assistance of Ken Mankoff, Bas Altena, Mathieu Tachon and Luc Girot for helping me with the Kinect and point cloud processing. Fieldwork has been an important part of my work and my grateful thanks extend once more to Alex and Miriam, as well as my assistants Mathieu Tachon, Coline Mollaret, Thomas Schellenberger, Paul Serail, Sofie Vej Ugelvig, Erik Johnson, helicopter pilot Bård and accompanying journalists: Magne Myrvold, Ib Salomon, and Alister Doyle.

As part of the SVALI project, I had the chance to collaborate with a warm, helpful, insightful and brilliant Nordic community. My special thanks goes to my SVALI colleagues and friends: Alexandra Messerli, Bergur Einarsson, Tómas Johannesson, Aslak Grinsted, and all the other SVALI students. I am very happy to have worked in a great academic environment and would like to thank Chris Nuth, Thomas Schuler, Olivier Gagliardini, and Andy Kääb for lively discussions and continuous encouragements. My PhD was shared between the University of Oslo and the Norwegian Water Resources and Energy Directorate, which was a fantastic working place. My colleagues at NVE have been substantial to my Norwegian integration. Thank you for offering me the opportunity to experience Julebord and Hemsedal(!), for the long chats about snow conditions, snow avalanches and getting me into off-ride and randonnée skiing.

The life in Oslo has been an absolute blast, as they'd say on the other side of the pond. I'll remember the amazing cross-country and downhill skiing, innebandy, frisbeegolf and quizbeegolf. I would like to thank all my former flatmates: the fantastic Agnar, Chris, Tobi, Sergi, Alex, Thomas, Luc and Bas, all you guys from Oslo: Christophe, Emma, Elisabeth, Sergi, Anna, Mathieu, Myra, Olivier, Caroline, Jonas, Solène, Lena, Anja, Jonas, Kirsty, Elvar, Azhar, Pedro, Robert, Sebastian and from my visits in Europe: Line, Felicia, Dorothée, Heidi, Mauro, Bill, my friends from home and Sheffield.

At last but not the least, thank you, Danka.

Contents

Abstract i

Acknowledgements v

I Overview 1

1 Introduction 2
1.1 Motivation . . . 2
1.2 Aim and Objectives . . . 3
1.3 Outline . . . 4

2 Background 8
2.1 Subglacial Hydrology . . . 8
  2.1.1 Subglacial Water Flow . . . 8
  2.1.2 Subglacial Drainage Systems . . . 10
  2.1.3 Interaction between Drainage Systems and Ice Dynamics . . . 11
2.2 Mechanical Response to Hydrological Changes . . . 12
2.3 Review of Direct Subglacial Measurements . . . 13

3 Field Site and Data 24
3.1 Engabreen and Svartisen Subglacial Laboratory . . . 24
  3.1.1 Engabreen . . . 24
  3.1.2 Svartisen Subglacial Laboratory . . . 26
3.2 Data Overview . . . 30
  3.2.1 Load Cells . . . 30
  3.2.2 Load Cell Experiment . . . 34
  3.2.3 Hydrological Data . . . 36
  3.2.4 Meteorological Data . . . 38

4 Temporal Variations in Subglacial Conditions from Load Cell Records 44
4.1 Paper I: Seasonal Variation of Basal Connectivity 46
4.2 Paper II: Anti-Correlation in Pressure by Load Transfer 48
4.3 Pressure Events 49
4.3.1 Manual Identification and Classification 49
4.3.2 Automatic Detection of Pressure Events 51
4.3.3 Seasonal Distribution of Intensity and Duration of Pressure Events 54
4.3.4 Timing and Shape of Daily Pressure Events 56
4.3.5 Daily Pressure Events and Discharge 59
4.3.6 Conclusions 61
4.4 Spring Melt Events 63
4.4.1 Simple Glacier Bed Response: Spring 2010 63
4.4.2 Complex Glacier Bed Response: Spring 2013 66
4.4.3 Conclusions 71

5 Mapping the glacier bed 76
5.1 Introduction 76
5.2 Techniques 77
5.2.1 Short-Range LiDAR: The Kinect™ 77
5.2.2 Structure from Motion 78
5.3 Methods 80
5.3.1 Kinect™ 80
5.3.2 Structure from Motion 84
5.4 Results 86
5.4.1 Mapping near LC97 86
5.4.2 Mapping near LC1e 88
5.5 Discussion 91
5.5.1 Kinect errors 91
5.5.2 Structure from Motion errors 92
5.5.3 Map comparison 94
5.6 Conclusion 95

6 Effect of cavity contraction on basal pressure 98
6.1 Background 98
6.2 The Contraction of an Artificial Cavity 99
6.2.1 Measurement of Closure Rate from Markers 101

6.2.2 Short-Range LiDAR and Closure Rate 101
6.2.3 Results and Interpretation 105
6.2.4 Experiment Conclusions 108
6.3 Modelling Cavity Contraction 109
6.3.1 Model Equations 109
6.3.2 Boundary conditions 110
6.3.3 Finite Element Discretisation 110
6.3.4 Effect of Cavity Geometry 111
6.3.5 Effect of Bed Slope and Sliding 113
6.3.6 Effect of Linear Rheology 113
6.4 Discussion 115
6.5 Summary 116

7 Conclusions **120**

References **125**

II Journal Publications **137**

Paper I: Interannual variability of glacier basal pressure from a 20 year record **139**

Paper II: Anti-correlated response at the glacier bed explained by load transfer **153**

III Appendices **179**

A Map of the SSL **180**

B Data Overview **181**

C Pressure Events **183**

D Spring Melt Events **186**

E Mapping Bedrock **190**

F Cavity Closure and Stress Bridging **196**

Part I

Overview

1 Introduction

1.1 Motivation

The hydrology of glaciers plays a key role in their dynamics, yet remains one of the greatest uncertainties in current predictions of glacier contribution to sea level rise. In the future, global warming will increase surface melt on the glacier and directly affect the glacier hydrology. The response of the subglacial drainage system and ice dynamics to these changes is complex and poorly understood but of great importance (e.g. IPCC, 2013; Dunse et al., 2015). This thesis contributes to our understanding of the effect of changes in subglacial hydrology on the response at the glacier bed.

Our current understanding of the subglacial hydrological system is based mainly on water pressure measurements in glacier boreholes (Hubbard et al., 1995; Murray and Clarke, 1995; Harper et al., 2007; Fudge et al., 2008; Schoof et al., 2014), and dye tracing (Nienow et al., 1998). It is assumed that the seasonal evolution of the hydrological system is characterised by a distributed system in winter from which channels develop as surface melt input increases in spring. The channelised system efficiently accommodates meltwater except for periods when the enlargement of channels is not fast enough to adapt to rapid melt or a rainfall event. The hydrological system contracts during low melt events and in autumn when the distributed drainage system again dominates.

However, understanding the nature of this evolution is limited because there are few observations of the subglacial hydrological system. Existing observations are usually short-term and reveal the high spatial variability of the drainage system that further limits a correct interpretation of the data. There is also poor understanding of the interaction between different parts of the hydrological system (e.g. distributed and channelised), that is assumed to cause annual changes in ice dynamics (Iken and Truffer, 1997). A thorough understanding of what causes changes in subglacial hydrology of glaciers is also pertinent to the hydrology of ice-sheets (Bartholomew et al., 2010; Sundal et al., 2011; Chandler et al., 2013).

1.2 Aim and Objectives

The aim of the thesis is to:

Understand the role of the subglacial hydrological system and mechanical processes in controlling the temporal and spatial variation in pressure at the glacier bed

In order to address this issue, three main topics have been investigated.

- What is the effect of variations in meltwater input on normal stress measured by the load cells?

  The objective is to identify what the load cell measures (e.g. ice, water, sediments) and investigate the relationship between meltwater production and pressure changes at the glacier bed. The mapping of the bedrock topography is also essential in order to better characterise the area surrounding the load cell and potential effects on normal stress at the glacier bed.

- What is the role of the basal hydraulic system in diurnal and seasonal variations in subglacial hydrology?

  This topic focuses on understanding the pressure signal at different temporal scales. Daily pressure events that characterise the pressure signal are examined. The seasonal and annual variations in the characteristics of these events are then quantified. These characteristics reflect the connectivity at the glacier bed and illustrate conditions that affect glacier dynamics.

- What is the role of higher order stresses on the subglacial hydraulic system?

  Spatial variations in the basal pressure at the glacier bed demonstrate the importance of mechanical processes. This topic combines observations, experiments, and modelling to help understand the role of stress transfer during pressurisation and contraction of the hydrological system. A full Stokes numerical model is used to examine the effect of stress bridging and load transfer on normal stress at the glacier bed.

1.3 Outline

This thesis primarily examines the effect of subglacial hydrology on the glacier bed response using records of normal stress from load cells installed at the Svartisen Subglacial Laboratory. The thesis is structured as follows:

Background
The basics of subglacial hydrology are discussed to help understand the implications of the thesis. The flow of water at the bed and the control of the hydraulic potential gradient are included. The different types of drainage system and the effect of each system on ice dynamics are shown. A review of direct observations at the glacier bed places the thesis in the context of earlier work.

Field Site
This chapter introduces the field site Engabreen and the Svartisen Subglacial Laboratory located in Norway. It also provides an overview of the data used in this thesis, including load cell, hydrological and meteorological data. Additionally, a key sensitivity experiment performed on the the load cells is described.

Response in pressure at the glacier bed
This chapter represents the core of the thesis, and summarises two articles that are attached after the manuscript. The first article is on seasonal and annual variations in pressure conditions and periods with contrasting spatial connectivity at the glacier bed. The second article examines the pressure signal that characterises the unconnected drainage system and the effect of mechanical stress redistribution (i.e. load transfer) on pressure at the glacier base. The rest of the chapter investigates daily pressure events and the role of subglacial hydrology in controlling the form of these events. Finally, the characteristics of the pressure signal during spring melt events are discussed.

Mapping
The bedrock around the load cells was mapped using innovative techniques: Kinect™ and Structure From Motion - SFM. The methodology and challenges are presented. The topography of the bedrock is described and the implications of the bedrock geometry for pressure measurements are considered.

Stress Bridging Effect

This chapter investigates the stress bridging effect during the contraction of the drainage system and describes observations of peaks in pressure that reach twice the overburden pressure. An experiment of contraction of a man-made cavity over the load cells reproduces the peak in pressure. A full Stokes model of a subglacial cavity is used to examine the controls on stress bridging and the peak in pressure.

Chapter 2
Background

The glacier base
sliding over a bedrock bump

2 Background

2.1 Subglacial Hydrology

2.1.1 Subglacial Water Flow

The subglacial hydrology is a unique system. Water is able to flow uphill under a glacier because subglacial water flows from zones of high pressure to zones of low pressure, in contrast with surface water that simply follows the surface slope. A simple analogue of subglacial water flow is a network of pipes fed by a water tower. Water flows from the high-pressure water tower towards parts of the network with lower pressure. The same is true for glaciers.

Water flow beneath glaciers depends on the gradient of the hydraulic potential, $\nabla\phi_{\text{subglacial}}$, which is balanced by the potential energy from the elevation difference of bedrock and the water pressure gradient as follows:

$$
\begin{aligned}
\nabla\phi_{\text{surface}} &= \rho_{\text{water}}\, g\, \nabla z_{\text{bedrock}} && (2.1)\\
\nabla\phi_{\text{subglacial}} &= \rho_{\text{water}}\, g\, \nabla z_{\text{bedrock}} + \nabla p_{\text{water}} && (2.2)
\end{aligned}
$$

ρ_{water} is the density of water, g the gravitational acceleration, and $\nabla z_{\text{bedrock}}$ the bedrock slope. Following Shreve (1972), pressure in subglacial channels is in balance with ice pressure, hence $p_{\text{water}} = p_{\text{ice}} = \rho_{\text{ice}}\, g\, h_{\text{ice}}$ with $h_{\text{ice}} = z_{\text{surface}} - z_{\text{bedrock}}$. Substituting for water pressure in Eq. (2.2) gives:

$$\nabla\phi_{\text{subglacial}} = \rho_{\text{ice}} g \left(\nabla z_{\text{surface}} + \frac{\rho_{\text{water}} - \rho_{\text{ice}}}{\rho_{\text{ice}}} \nabla z_{\text{bedrock}} \right) \tag{2.3}$$

Computing the density ratio in this equation with $\rho_{\text{ice}} = 910$ kg.m^{-3} and $\rho_{\text{water}} = 1000$ kg.m^{-3} shows that the slope of the glacier surface is $\sim$ 10 times more important than the bedrock slope in controlling water flow. Figure 2.1b shows examples of profiles of hydraulic potential gradient $\nabla\phi$ for a simple glacier surface geometry and a sinusoidal bed topography (Fig. 2.1a). The bedrock affects the direction of water flow, indicated as a change in sign of the hydraulic potential gradient, only when water pressure is $\leqslant 80$ % of the ice overburden pressure (dashed line and red arrow). The glacier surface slope causes water at the glacier bed to flow uphill even for bedrock with a steep reverse slope. If the glacier was absent, the water would follow the steepest bedrock slope as indicated by the blue arrows. Hence, the bed geometry appears to have little importance in subglacial water flow. However, this relation assumes that water pressure in the subglacial drainage system, especially pressure in R-channels, equals ice pressure and this condition is only true for steady-state conditions (Shreve, 1972).

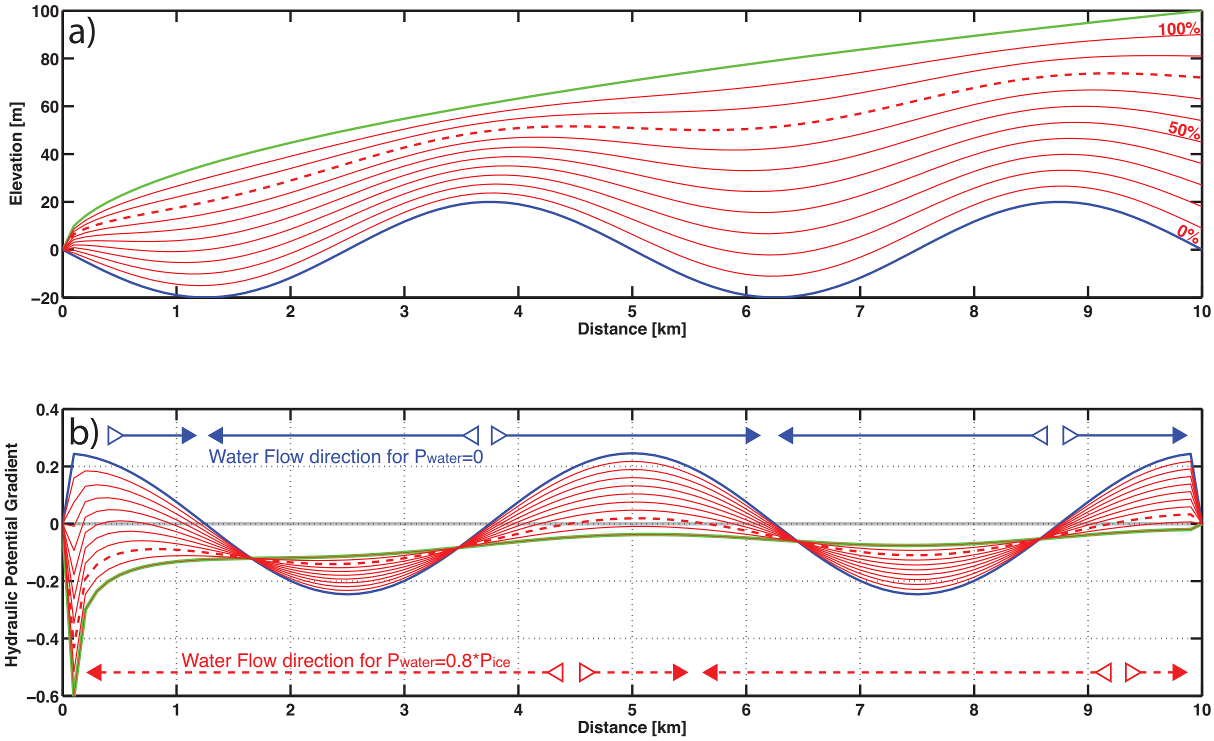

Figure 2.1: a) Glacier surface (green), bed (blue) and hydraulic potential (red) for water pressure equal to 0-100 % ice pressure. b) Direction of water flow (arrows) governed by the sign of the gradient of the hydraulic potential. The gradients given for water pressure equal to 0 % and 80 % of ice pressure are highlighted in blue and dashed red, respectively.

2.1.2 Subglacial Drainage Systems

The variation in water pressure is driven by the type of subglacial drainage system. The hydrological system under the glacier can be of two different types: an efficient channelised type and an inefficient distributed type (Fig. 2.2).

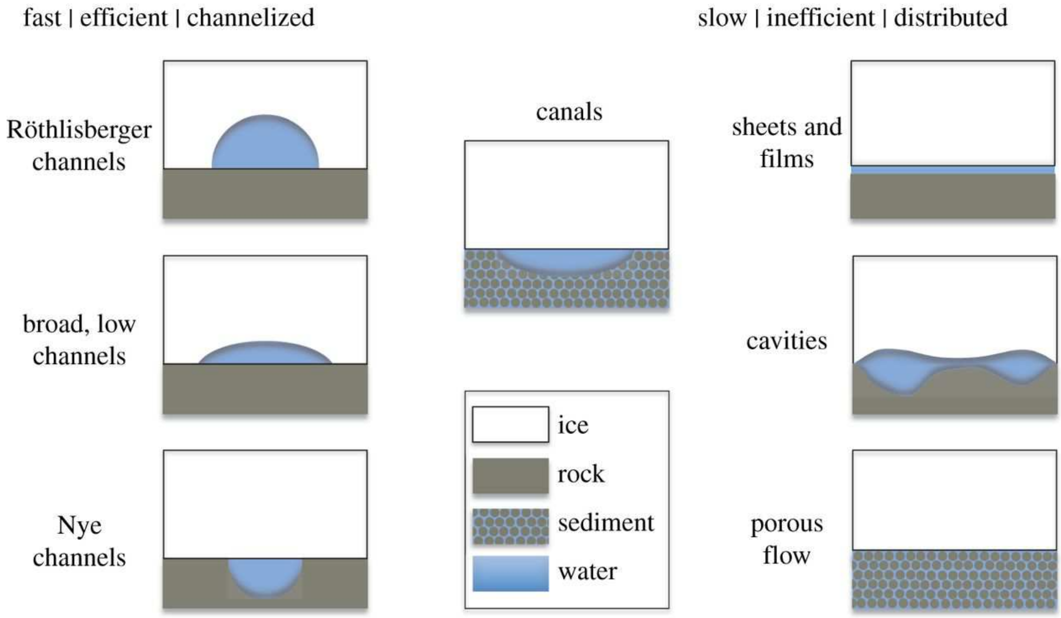
fast | efficient | channelized
slow | inefficient | distributed
Röthlisberger channels
broad, low channels
Nye channels
canals
sheets and films
cavities
porous flow
ice
rock
sediment
water

Figure 2.2: Types of subglacial drainage system (Flowers, 2015).

For hard-bedded glaciers, channels take the form of 1) Röthlisberger channels, semi-circular channels incised in the ice (Röthlisberger, 1972), 2) Hooke channels that are in the ice, low and broad (Hooke et al., 1990) and 3) Nye channels, that are incised in bedrock (Nye, 1976). The opening or melting of conduits incised in the ice (types 1 and 2) is determined by the flow of subglacial water originating from surface/subglacial melt or subglacial storage. This opening opposes ice creep that leads to the contraction of the channel. The channelised system is characterised by fast, efficient drainage. A steady-state condition between water pressure and ice pressure in channels exists when channels grow/contract at the same rate (Shreve, 1972). In practice, channel melt usually occurs much faster than ice deformation. This frequent imbalance leads to low-pressure channels ($p_{\text{water}} < p_{\text{ice}}$) when the capacity of the drainage system is greater than meltwater input (Lappegard, 2006a, Paper II). However, if the increase in meltwater input is rapid (e.g. during rainfall events), melting of channels may not occur fast enough and the channels will not be able to accommodate subglacial discharge. This causes over-pressurisation of the drainage system ($p_{\text{water}} > p_{\text{ice}}$) (Bartholomaus et al., 2008; Schoof, 2010) and this has a significant effect on the hydromechanical response of the glacier base as discussed in section 2.2.

The distributed drainage system is controlled primarily by ice pressure and basal sliding that can decrease the pressure melting point and enhance basal melting, thus increasing production of subglacial water. In essence, the distributed drainage system is not driven by the rate of water flow, and is seen as a porous medium where porosity and gradient in hydraulic potential regulates water flux. In this system, water flows either within a thin water film or sheet or through a linked cavity system (Weertman, 1972; Lliboutry, 1976; Fountain and Walder, 1998). The sliding of ice over bumps mechanically opens cavities on their lee side where normal stress is reduced and water pressure is high. The distributed drainage is slow as subglacial water follows bedrock topography (i.e. normal stress distribution). As water is not evacuated efficiently, subglacial water is stored in this system and water pressure increases to near-overburden pressure (Schoof et al., 2014). Drainage from this reservoir may occur during rapid decoupling events or floods at the glacier base that reduce the extent of the pressurised, distributed drainage system under the glacier (Harper et al., 2007).

2.1.3 Interaction between Drainage Systems and Ice Dynamics

The distributed drainage system comprises most of the glacier bed whereas channels are localised phenomena. The interaction between the channelised and distributed drainage system is complex, but can be simplified as follows. The theory of subglacial water flow predicts that during over-pressurisation in conduits, water flows from the channelised part to the distributed part (Hubbard et al., 1995). Alternatively, when water is drained from the channel and water pressure is low, then water is drained from the distributed drainage system into channels. However, low pressure channels may be sealed from the rest of the hydrological system as ice creep is enhanced at the channel edge due to the stress bridging effect (Lappegard et al., 2006). It is proposed that increased ice deformation can isolate channels from their surroundings and parts of the subglacial hydrological system, thus increasing storage of water at the glacier bed.

Effective pressure, the difference between ice pressure and water pressure, has a substantial effect on basal sliding that affects the opening rate of subglacial cavities (Hoffman and Price, 2014). This feedback between water pressure and ice dynamics leads to a complicated non-linear response of glacier hydrology and flow. Nevertheless, it is understood that it is the over-pressurisation within channels that causes glacier speed-up (i.e. forcing), and that the distributed system has the role of amplification/dampening depending on the extent of areas with high water pressure (Murray and Clarke, 1995; Andrews et al., 2014).

2.2 Mechanical Response to Hydrological Changes

Glacier flow is generally considered non-Newtonian, but glaciers may also exhibit elastic response, e.g. during over pressurisation of the subglacial drainage system (Cuffey and Paterson, 2010). Figure 2.3 shows the subdivisions of continuum mechanics; ice deformation may be defined by the laws of fluid or solid mechanics, depending on the conditions and time scale. This is one of the most intriguing properties of ice - that it is both a viscous (fluid) and elastic (solid) material under natural conditions (Fig. 2.3). The effect of each ice property can be differentiated because the ice deforms viscously on long time scales, whereas elastic displacement occurs almost instantaneously and for small stresses.

The visco-elastic response of ice is very important for subglacial hydrology (Pimentel and Flowers, 2011). Observations of surface velocity and hydrology show that uplift of the glacier surface or reverse motion can be a response to hydraulic jacking at the glacier bed (Bartholomew et al., 2012). Hydraulic jacking can occur due to rainfall events, intense melt, outburst floods or lake drainage. Under these circumstances, the growth of the channelised drainage system is slower than the meltwater input. This imbalance leads to an intense increase in water pressure. Although hydraulic jacking is often observed, modelling shows that the elastic and visco-elastic properties of ice do not entirely explain the surface response and connected basal response (Murray and Clarke, 1995; Riesen, 2011). Based on a simplified viscoelastic model, Sugiyama et al. (2007) suggest that this discrepancy may be due to a too high Young's modulus for ice (5.1 GPa). Nevertheless, it is surprising that viscoelastic models do not successfully reproduce the surface response from changes in hydrology, but can successfully reproduce tidal flexure of ice-shelves (Anandakrishnan and Alley, 1997). This may be due to several different processes, not only subglacial jacking. The opening and closing of cavities may dominate the lifting of the glacier surface (Iken and Bindschadler, 1986; Harper et al., 2007) and sediment deformation may contribute to some extent (Murray and Clarke, 1995).

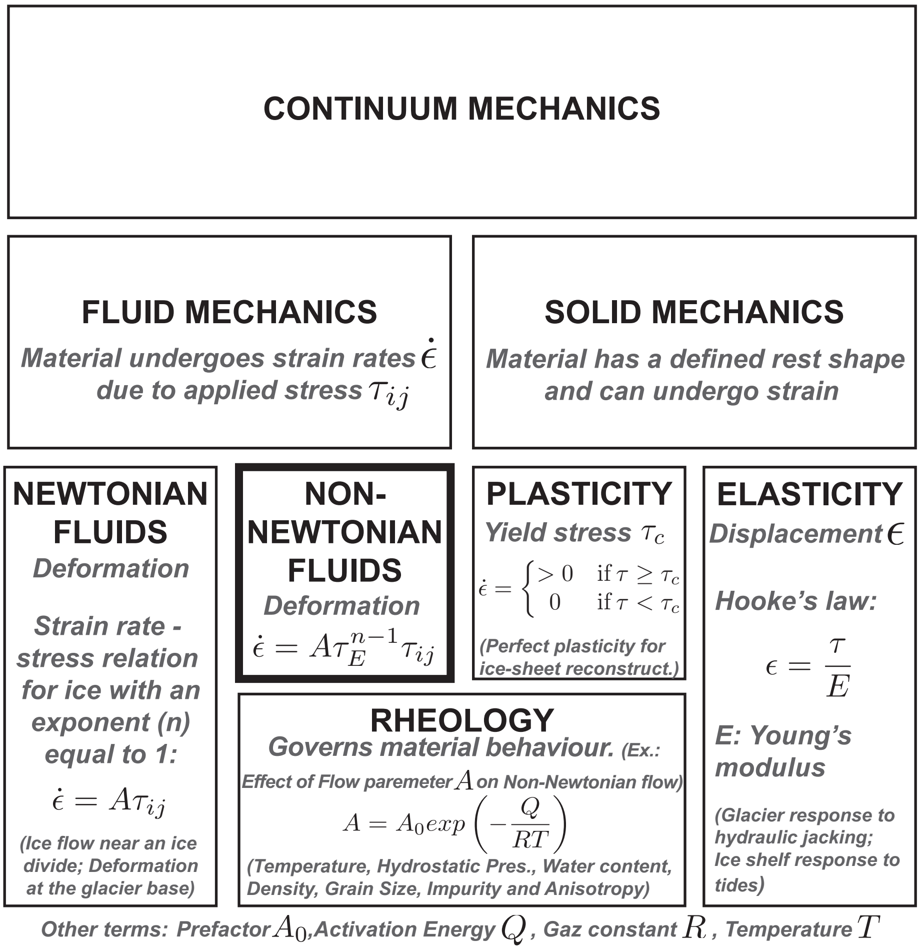
CONTINUUM MECHANICS
FLUID MECHANICS
Material undergoes strain rates $\dot{\epsilon}$ due to applied stress τ_{ij}
SOLID MECHANICS
Material has a defined rest shape and can undergo strain
NEWTONIAN FLUIDS
Deformation
Strain rate - stress relation for ice with an exponent (n) equal to 1:
$\dot{\epsilon} = A\tau_{ij}$
(Ice flow near an ice divide; Deformation at the glacier base)
NON-NEWTONIAN FLUIDS
Deformation
$\dot{\epsilon} = A\tau_E^{n-1}\tau_{ij}$
PLASTICITY
Yield stress τ_c
$\dot{\epsilon} = \begin{cases} > 0 & \text{if } \tau \geq \tau_c \\ 0 & \text{if } \tau < \tau_c \end{cases}$
(Perfect plasticity for ice-sheet reconstruct.)
ELASTICITY
Displacement ϵ
Hooke's law:
$\epsilon = \frac{\tau}{E}$
E: Young's modulus
(Glacier response to hydraulic jacking; Ice shelf response to tides)
RHEOLOGY
Governs material behaviour. (Ex.: Effect of Flow paremeter A on Non-Newtonian flow)
$A = A_0 exp\left(-\frac{Q}{RT}\right)$
(Temperature, Hydrostatic Pres., Water content, Density, Grain Size, Impurity and Anisotropy)
Other terms: Prefactor A_0, Activation Energy Q, Gaz constant R, Temperature T

Figure 2.3: Subdivisions of continuum mechanics, adapted from wikipedia and Cuffey and Paterson (2010).

2.3 Review of Direct Subglacial Measurements

This review examines the importance of previous direct, subglacial and englacial observations in glaciology and is summarised schematically in figure 2.4. Direct observations are defined as direct measurements of subglacial or englacial processes that were conducted at the glacier bed or deep inside the glacier using englacial tunnels, marginal cavities or subglacial hydropower infrastructures (Fig. 2.5). The definition is broad in order to include englacial studies made from ice tunnels in the 1950s that were important for the validation of Glen's flow law. The rest of the research analysed focuses on processes occurring at or near the ice-bedrock interface and includes observations from three subglacial laboratories: one in operation since 1966 under Glacier d'Argentière, France, one under

Bondhusbreen, Norway between 1978 and 1982, and one that was established in 1992, the subject of this thesis, under Engabreen, Norway (Fig. 2.4).

In this review, I start with the first observations related to a subglacial intake. Direct observations are then shown to have had a crucial role in the development of the flow law of glaciers and in understanding ice deformation at the glacier base (i.e. basal facies). Measurements of sliding at the glacier bed were also key in validating the sliding theory of regelation, cavitation, till deformation and in sub-freezing conditions. Afterwards, the effect of erosion observations on the validation of quarrying and abrasion models is covered and I finish with recent developments in subglacial hydrology based on direct subglacial investigations.

The first documented, direct observations of the glacier bed were made for hydropower purposes at Glacier de Tré-La-Tête, France in 1940s (Waeber, 1944). The aim was to tap subglacial water of this glacier at high elevation and complement the summer input of a reservoir that fed an industrialised river catchment. This pioneer study described for the first time the existence of a subglacial channel at the glacier bed. It also showed that the diversion of a subglacial channel was possible, although Waeber (1944) admitted that the phenomena occurring at the glacier bed remained 'a bit mysterious'.

After the second world war, a growing interest in the research of glacial processes guided the first attempts in finding a generalised flow law of glaciers. The need to validate Glen's flow law based on his 1952 experiments motivated studies to monitor the deformation of englacial tunnels such as those bored into Z'Mutt glacier and Mont Collon glacier in Switzerland (Haefeli, 1951, 1952), and Vest-Skautbreen glacier in Norway (McCall, 1952, 1954). These direct observations of ice creep confirmed that ice deforms as a viscous material (Nye, 1953). The ice tunnel experiments exhibited Non-Newtonian flow with a flow law exponent of 3, whereas observations of borehole deformation at Jungfraufirn (Switzerland) showed that the exponent was closer to 1.5 for low shear stresses (Perutz, 1950; Gerrard et al., 1952). Although Nye's (1953) theory of ice flow failed to explain this difference, Glen (1955) unified the direct and borehole observations based on an experiment of compression of ice. He proposed that the viscous nature of ice creep and the difference in exponent describes a transition of ice creep, thus explaining both cases. Glen (1956) also conducted an experiment of tunnel contraction below the ice fall of Austerdalsbreen glacier, Norway. He observed deformation rates much higher than the other tunnel experiments and inferred that it was caused not only by the overburden pressure, but by increased longitudinal compressive stresses as predicted by the generalised flow law of ice (Nye, 1953; Glen, 1955).

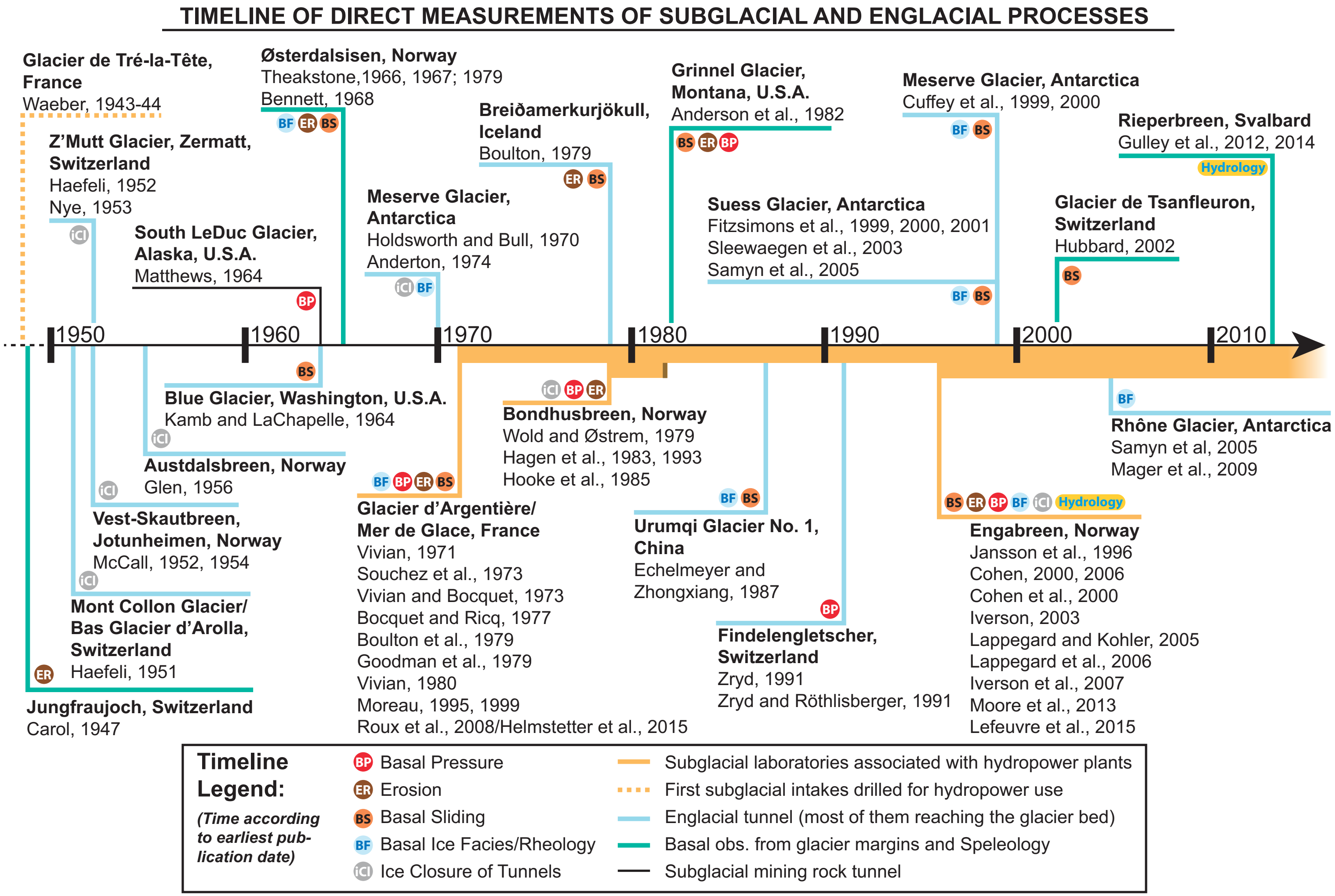
TIMELINE OF DIRECT MEASUREMENTS OF SUBGLACIAL AND ENGLACIAL PROCESSES
Glacier de Tré-la-Tête, France
Waeber, 1943-44
Østerdalsisen, Norway
Theakstone,1966, 1967; 1979
Bennett, 1968
BF ER BS
Z'Mutt Glacier, Zermatt, Switzerland
Haefeli, 1952
Nye, 1953
iCl
South LeDuc Glacier, Alaska, U.S.A.
Matthews, 1964
BP
Breiðamerkurjökull, Iceland
Boulton, 1979
ER BS
Meserve Glacier, Antarctica
Holdsworth and Bull, 1970
Anderton, 1974
iCl BF
Grinnel Glacier, Montana, U.S.A.
Anderson et al., 1982
BS ER BP
Suess Glacier, Antarctica
Fitzsimons et al., 1999, 2000, 2001
Sleewaegen et al., 2003
Samyn et al., 2005
BF BS
Meserve Glacier, Antarctica
Cuffey et al., 1999, 2000
BF BS
Rieperbreen, Svalbard
Gulley et al., 2012, 2014
Hydrology
Glacier de Tsanfleuron, Switzerland
Hubbard, 2002
BS
1950
1960
1970
1980
1990
2000
2010
BS
Blue Glacier, Washington, U.S.A.
Kamb and LaChapelle, 1964
iCl
Austdalsbreen, Norway
Glen, 1956
iCl
Vest-Skautbreen, Jotunheimen, Norway
McCall, 1952, 1954
iCl
Mont Collon Glacier/ Bas Glacier d'Arolla, Switzerland
Haefeli, 1951
ER
Jungfraujoch, Switzerland
Carol, 1947
BF BP ER BS
Glacier d'Argentière/ Mer de Glace, France
Vivian, 1971
Souchez et al., 1973
Vivian and Bocquet, 1973
Bocquet and Ricq, 1977
Boulton et al., 1979
Goodman et al., 1979
Vivian, 1980
Moreau, 1995, 1999
Roux et al., 2008/Helmstetter et al., 2015
iCl BP ER
Bondhusbreen, Norway
Wold and Østrem, 1979
Hagen et al., 1983, 1993
Hooke et al., 1985
BF BS
Urumqi Glacier No. 1, China
Echelmeyer and Zhongxiang, 1987
BP
Findelengletscher, Switzerland
Zryd, 1991
Zryd and Röthlisberger, 1991
BS ER BP BF iCl Hydrology
Engabreen, Norway
Jansson et al., 1996
Cohen, 2000, 2006
Cohen et al., 2000
Iverson, 2003
Lappegard and Kohler, 2005
Lappegard et al., 2006
Iverson et al., 2007
Moore et al., 2013
Lefeuvre et al., 2015
BF
Rhône Glacier, Antarctica
Samyn et al, 2005
Mager et al., 2009
Timeline Legend:
(Time according to earliest publication date)
BP Basal Pressure
ER Erosion
BS Basal Sliding
BF Basal Ice Facies/Rheology
iCl Ice Closure of Tunnels
Subglacial laboratories associated with hydropower plants
First subglacial intakes drilled for hydropower use
Englacial tunnel (most of them reaching the glacier bed)
Basal obs. from glacier margins and Speleology
Subglacial mining rock tunnel

Figure 2.4: Timeline of direct observations of subglacial and englacial processes.

Observations from ice tunnels at the glacier bed complemented our knowledge of basal ice facies and deformation obtained from laboratory experiments and ice cores. The advantages of tunnels are the spatial coverage of the observations compared with point measurements in boreholes, as well as the possibility of monitoring in-situ subglacial processes over time (Budd and Jacka, 1989; Moore, 2014). Investigation of basal facies is a common theme at the glacier bed (Fig. 2.4) and there has been much research on this topic in the dry valleys of Antarctica (Holdsworth, 1974; Cuffey et al., 2000; Fitzsimons et al., 2001; Samyn et al., 2005), where drilling of tunnels is facilitated by the vertical walls of the glacier fronts. The glacier base is shown to be highly heterogenous and composed of folded debris-rich and clean ice layers in both cold-based (Holdsworth, 1974) and temperate glaciers (Vivian and Bocquet, 1973). Monitoring of in-situ creep of the tunnel demonstrated that debris-rich layers and amber ice, a layer with high salt concentration, fine debris and air bubbles, deform faster than clean ice (Holdsworth and Bull, 1970; Echelmeyer and Zhongxiang, 1987; Cohen, 2000). Several mechanisms were suggested as causes of the enhanced strain. Holdsworth and Bull (1970) suggested either a preferred orientation in ice crystals or impurities from direct observations at Meserve glacier in the dry valleys of Antarctica. Echelmeyer and Zhongxiang (1987) hypothesised that softening of debris-rich layers at Urumqi n.1 glacier in China is due to inter-granular water, as increased stresses between particles reduce the temperature melting point and the ice melts. In contrast, high debris concentration were shown to stiffen the glacier base at Suess glacier, Antarctica (Fitzsimons et al., 2001). Although tunnels are often located below thin ice (low shear stress) and in marginal areas, these observations have important consequences for cold-based glaciers as enhanced deformation may explain a significant part of the glacier motion. In tunnels reaching deeper ice such as at Glacier d'Argentière, Bondhusbreen and Engabreen, the ice exposes elongated water pockets that are thought to soften the basal ice even more (Vivian and Bocquet, 1973; Hagen et al., 1993; Jansson et al., 1996). These direct observations show that ice rheology and basal structures have strong effects on the relation between shear stress and ice deformation. These processes that cause ice to deform at low shear stress (i.e. at the glacier bed) lead Glen's flow law to have a high flow parameter A (Cohen, 2000) and an exponent closer to 1 than 3 (Holdsworth and Bull, 1970).

Investigations in ice tunnels also determined the significant role of sliding in glacier dynamics. Direct observations were crucial for the development and validation of theories of glacier sliding (Fig. 2.4). After the acceptance of Glen's flow law, observations showed that sliding can contribute up to 80 % of the glacier flow (Glen, 1956) and Weertman

(1957) developed the first sliding theory. His theory is based on the combination of plastic flow over a small bump and heat transfer through the bump due to phase changes of water and ice. The stress concentration on the stoss side of the bump reduces the pressure melting point leading to melting of the ice. The liquid water flows to the lee side where stresses are lower and causes regelation of water. The hypothesised results of the sliding law were observed in an ice tunnel reaching the bed of Blue Glacier, USA (Kamb and LaChapelle, 1964). They observed in-situ the two processes associated with Weertman sliding: 1) regelation layers identified by air bubble structure and debris content and 2) plastic flow by foliation structure in the ice. Kamb and LaChapelle (1964) furthered their analysis by performing an experiment where a wire passed through a block of ice by regelation and plastic flow, thus confirming earlier findings. Goodman et al. (1979) suggested that regelation processes also affect sliding by causing ice to freeze on the bedrock on the lee-sides of bumps, which would explain jerky variations in strain measured at the bed of Glacier d'Argentière, France.

Direct observations thus validated the sliding theory of glaciers by regelation, but also inspired examination of the role of cavitation in sliding (Lliboutry, 1968). Observations of bed decoupling on the lee-sides of bumps (Carol, 1947; McCall, 1952; Nye, 1953; Theakstone, 1967) suggested that cavitation and variations in water pressure (Mathews, 1964) may explain sliding of glaciers. Direct observations later confirmed the widespread extent of cavities (Vivian and Bocquet, 1973; Theakstone, 1979). Lliboutry (1968) proposed that the opening of cavities is controlled by a reduction in normal stress on the lee side of bumps and effective pressure. This decrease in normal stress was observed using pressure sensors installed on artificial bumps at the bed of Bondhusbreen in Norway (Hagen et al., 1983) and Findelengletscher in Switzerland (Zryd, 1991). The opening of a cavity was even observed visually on the lee-side of a man-made bump at Engabreen, Norway (Cohen et al., 2000). The cavitation theory also argues that the development of cavities and balance of friction at the glacier base can explain fast changes in sliding (Lliboutry, 1968) Short-term measurements of sliding in a marginal cavity showed the existence of rapid irregular slip at Glacier de Tsanfleuron (Hubbard, 2002). Monitoring of the seismicity has helped identify comparable rapid and short sliding events also called stick-slip motion. A new development in the investigation of sliding is the installation of seismometers in rock tunnels beneath glaciers in order to get closer to the source. The obtained measurements helped to precisely localise stick-slip events and were performed at both Glacier d'Argentière and Engabreen (Roux et al., 2008; Moore et al., 2013; Helmstetter et al., 2015).

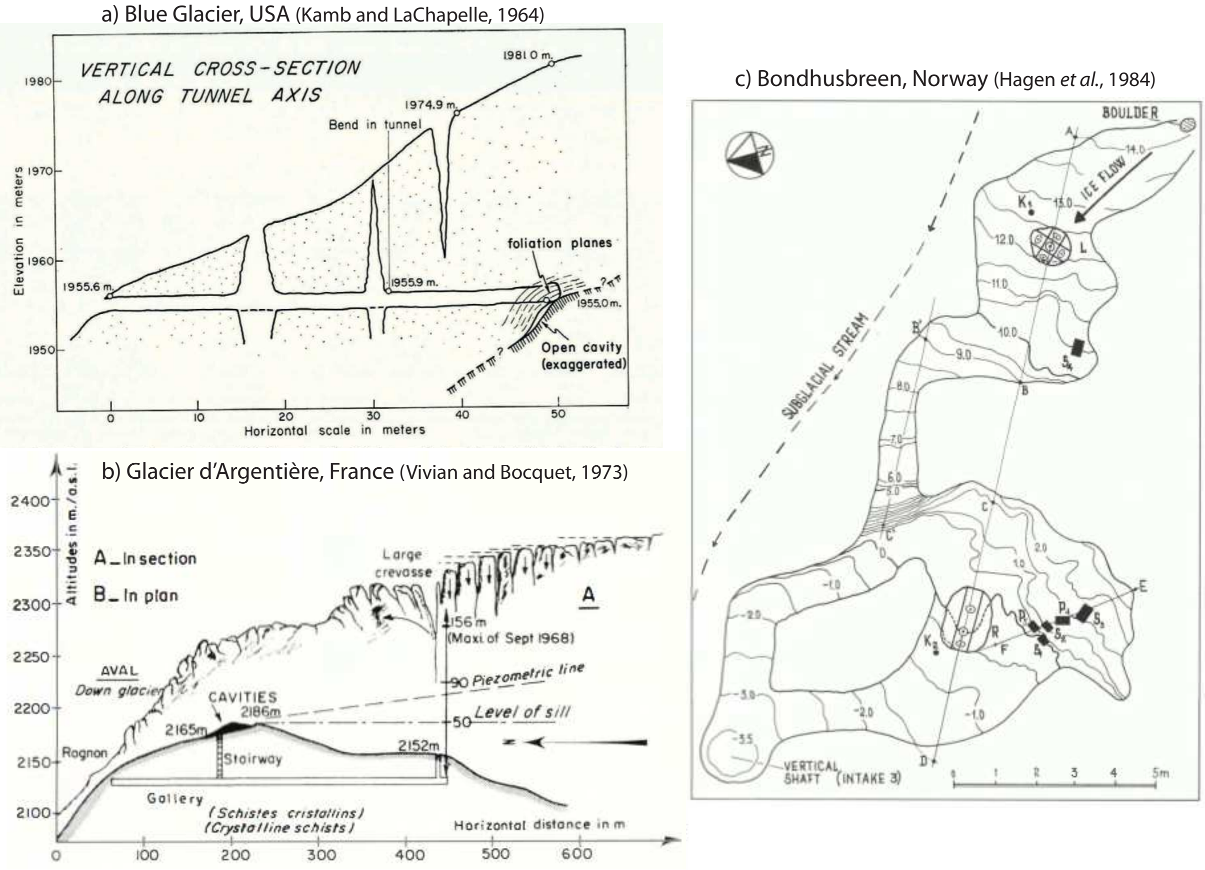

a) Blue Glacier, USA (Kamb and LaChapelle, 1964)

b) Glacier d'Argentière, France (Vivian and Bocquet, 1973)

c) Bondhusbreen, Norway (Hagen *et al.*, 1984)

VERTICAL CROSS-SECTION
ALONG TUNNEL AXIS
1981.0 m
1974.9 m
Bend in tunnel
foliation planes
1955.6 m
1955.9 m.
1955.0 m.
Open cavity
(exaggerated)
Elevation in meters
1980
1970
1960
1950
0
10
20
30
40
50
Horizontal scale in meters
Altitudes in m./a.s.l.
2400
2350
2300
2250
2200
2150
2100
A_In section
B_In plan
Large
crevasse
A
156 m
(Maxi of Sept 1968)
90 Piezometric line
50 Level of sill
AVAL
Down glacier
CAVITIES
2186m
2165m
Rognon
Stairway
2152m
Gallery
(Schistes cristallins)
(Crystalline schists)
Horizontal distance in m
0
100
200
300
400
500
600
BOULDER
ICE FLOW
SUBGLACIAL STREAM
K1
K2
L
A
B
B'
C
C'
D
E
F
R
P1
S1
S2
S3
S4
14.0
13.0
12.0
11.0
10.0
9.0
8.0
7.0
6.0
5.0
2.0
1.0
0
-1.0
-2.0
-3.0
-3.5
VERTICAL
SHAFT (INTAKE 3)
0
1
2
3
4
5m

Figure 2.5: Examples of subglacial ice tunnels. a) Important observations of regelation processes were made from tunnels drilled into the ice fall of Blue Glacier, U.S.A.. b) Major subglacial investigations were conducted from hydropower tunnels located under Glacier d'Argentière, France c) After drilling a subglacial tunnel from a hydropower intake, artificial bumps were installed to monitor ice pressure and flow at Bondhusbreen, Norway.

Sliding also occurs through the deformation of a basal sediment layer, as tested in an artificial tunnel drilled in the margins of Breðamerkurjöskull, Iceland (Boulton and Hindmarsh, 1987). In this tunnel, the till was instrumented with vertical segments of a rod that deformed with the till. The experiment showed that the sediment layer deforms as a function of depth after reaching a yield stress. This visco-plastic relation for till creep was generalised for use in ice-sheet models (Boulton and Jones, 1979). However, this relation has been debated and the reliability of this experiment has been questioned based on further laboratory experiments (Iverson et al., 1998). Nevertheless, Iverson et al. (2007) demonstrated that water-pressurised till installed under 200 metres of ice at Engabreen reproduces a similar increase in till deformation from the bedrock to the ice-debris interface. The contact between the debris-rich ice and the till prism at the base of Engabreen was also shown to significantly increase the shear stress at the bed (Iverson et al., 2003). Friction at the interface is thus consequently higher than generally assumed and should not be neglected as is often the case in models of sliding.

Direct observations of the bed showed that sliding is also possible at sub-freezing temperatures, as predicted by Shreve (1984). Sliding was thought to exist for temperate glaciers only, but monitoring of ice flow in tunnels showed velocities faster than caused by ice deformation only at the interface between ice and rocks at Urumqi n. 1 glacier in China, and at Meserve and Suess glaciers in Antarctica (Echelmeyer and Zhongxiang, 1987; Cuffey et al., 1999; Fitzsimons et al., 2000). The measured sliding at the bed of these cold-based glaciers was an order of magnitude greater than the estimate given in Shreve (1984). Direct observations confirmed the presence of water at the interface between ice and rocks. The water layer is generated by the concentration of stresses upstream of particles that reduces the pressure melting point, as observed in regelation. This interfacial water explains the existence of sliding at sub-freezing temperatures, which contradicts the absence of erosion at the glacier bed and so the preservation role of cold-based glaciers as assumed in geomorphology (Cuffey et al., 2000). Direct observations at Meserve glacier in Antarctica demonstrated that not only does sliding occur at the glacier bed, but cold-based glaciers erode the landscape by abrasion.

A better understanding of erosion was obtained through the description and measurement of processes directly at the glacier bed and from the glacier margins. Subglacial erosion is particularly important in the design of hydropower plants in order to estimate the rate of sediment input to a reservoir (Wold and Østrem, 1979). Observations at the bed led to the hypothesis that quarrying may dominate subglacial erosion (Carol, 1947; Bennett, 1968; Anderson et al., 1982). Quarrying occurs due to stress concentration at the edge of cavities and fracture propagation. In an experiment at Engabreen, the fatigue of a crack and failure was shown to depend on the variation of water pressure and growth of a cavity (Cohen et al., 2006), which differs from abrasion that is mostly controlled by sliding. The rate of abrasion has never been measured directly at the glacier bed, but the role of stress concentrations at the contact point between particles and bedrock has been estimated (Boulton et al., 1979; Iverson, 1991). Rocks transported along the bed can cause a rapid increase in normal stress on bedrock due to their small contact surface. At Bondhusbreen, Norway, an increase of several times the overburden pressure was measured at a load cell placed on the stoss side of an artificial bump (Hagen et al., 1983). Vivian (1997) also suggests from observations at the base of Glacier d'Argentière and Mer de Glace, France that subglacial erosion is dominated by fluvial processes of subglacial channels. In this case, rock transport in subglacial rivers will cause hard collisions between rocks and bedrock leading to its fatigue. This neglected theory may get more interest as new models coupling ice dynamics and subglacial hydrology investigate the role of water in eroding the bed (Beaud et al., 2014).

In recent years, there has been more focus on direct measurements of the hydrological system at or near the glacier bed (Fig. 2.4). At Engabreen, the hydrological system was described using a unique setup where connectivity between rock boreholes is assessed as water is pumped from the rock tunnel to the glacier bed (Lappegard and Kohler, 2005). This experiment showed that the capacity of the drainage system is low in winter and high in summer as connections with the efficient drainage system are made. The thin water film was also hypothesised to be observed in pressure measurements at load cells (Lappegard et al., 2006). Recent theory of development of subglacial hydrology built on these rare and valuable direct observations (Schoof, 2010; Hewitt, 2011). Observations of water flow in channels also indicate that models are sensitive to the roughness of subglacial channels, which can vary significantly. Access to subglacial conduits in winter by speleology is used to map their geometry and measure variations in roughness (Gulley et al., 2012, 2014). Direct observations of subglacial hydrology are presently the focus of much study as subglacial hydrological models are becoming more sophisticated. Subglacial laboratories offer a unique opportunity to study this part of the glacier system under conditions more representative of glaciers compared with englacial and marginal access because the ice above the subglacial access is thicker (60-210 m).

Chapter 3
Field Site and Data

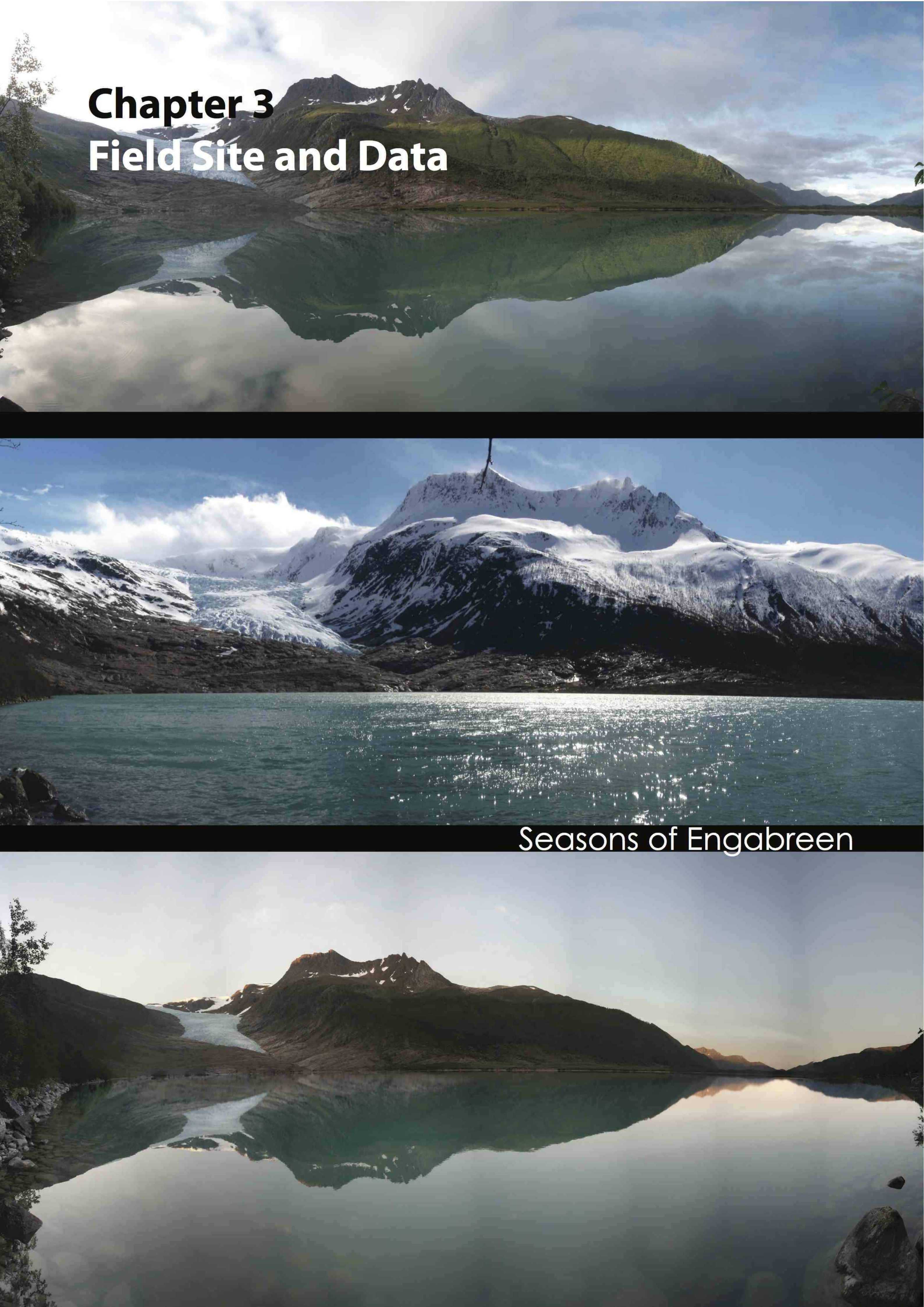

Seasons of Engabreen

3 Field Site and Data

3.1 Engabreen and Svartisen Subglacial Laboratory

3.1.1 Engabreen

Engabreen is a hard-bedded valley outlet glacier of the Western Svartisen ice cap, the second largest ice cap in continental Europe (Fig. 3.1). It is located in northern Norway just north of the arctic circle (66°40’ N, 13°50’ E). This temperate glacier drains an area of 36 km^2, and has a mean slope of 6°(Andreassen et al., 2012). The ice flows from a flat high accumulation area that has a maximum elevation of 1581 m a.s.l., into a crevassed plateau around 1175 m a.s.l, and then into an ice fall from ∼900 m a.s.l., below which is situated the Svartisen Subglacial Laboratory. Above the laboratory, the glacier surface has an elevation of 825 m a.s.l. (DEM from 2013, Messerli, 2015), a slope exceeding 20° and is 1.5 km wide. The glacier flows westward near the icefall, and northward at lower elevation. Shading provided by the peak Midnattssoltinden (1091 m a.s.l.) protects the lower tongue (Fig. 3.1) from high surface melt, which contributes to making Engabreen the lowermost glacier in Europe. The glacier front went down to the proglacial lake Engabrevatnet (10 m a.s.l) in 1999 as a result of an advance in the 1990s. Since 2000, the glacier tongue has continuously retreated (Winsvold et al., 2014), and the front reaches in 2013 an elevation of 114 m a.s.l..

The topography of the underlying bedrock is known at a low resolution (Kennett et al., 1993) because radar penetration is limited in temperate ice with high water content and signal scattering is high in crevassed areas. The sparse measurements indicate a deeper bed on the western side of the valley glacier, a possible riegel near the Svartisen Subglacial Laboratory (630 m a.s.l.) and a deeper trough (> 600 m deep) on the plateau. The geology of the bedrock may explain the little erosion above the glacier bend because a major divide between garnet mica schist and granitic gneiss occurs above the icefall and is roughly orientated East-West (Geological map from Norges Geologiske Undersøkelse). In the lower part, the bed is characterised by intensely folded metamorphic rocks. Their

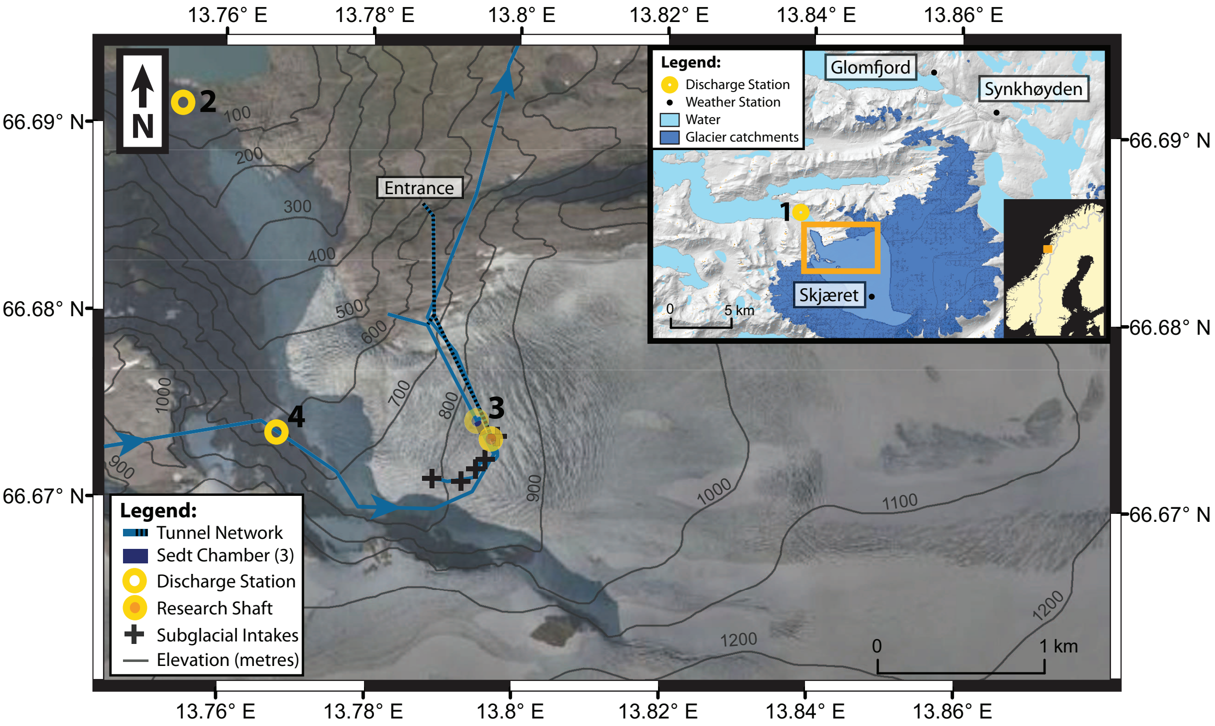
13.76° E
13.78° E
13.8° E
13.82° E
13.84° E
13.86° E
66.69° N
66.68° N
66.67° N
N
2
4
3
Entrance
100
200
300
400
500
600
700
800
900
1000
1100
1200
Legend:
Tunnel Network
Sedt Chamber (3)
Discharge Station
Research Shaft
Subglacial Intakes
Elevation (metres)
0
1 km
Legend:
Discharge Station
Weather Station
Water
Glacier catchments
Glomfjord
Synkhøyden
Skjæret
1
0
5 km

Figure 3.1: Satellite image of Engabreen from 2009 (source: Kartverket) with 100 m elevation contour lines, location of the rock tunnel network, research shaft and hydrological stations (2-4). The inset shows glacierised areas, Engabreen's catchment (lighter blue), hydrological (1) and meteorological stations (Glomfjord, Synkhøyden, and Sjkæret).

structure and layering are preferentially orientated east-west and their dip is sub-vertical (Sørensen, 1955). On the eastern side of the Western Svartisen ice cap, the orientation turns northeast-southwest (Geological map from Norges Geologiske Undersøkelse).

Engabreen has a strong maritime climate characterised by high precipitation and melt. Annual mass balance has been measured since 1970 (Fig. 3.2) and shows that the winter balance is between 1.5 and 4.6 m.w.e. (metres water equivalent), and the summer balance is from -4.0 to -1.2 m.w.e. (Kjøllmoen et al., 2011, and Climate Indicator product by NVE). The net mass balance was positive during the 1990s following changes in atmospheric circulation pattern in the Northern Atlantic (Chinn et al., 2005), which caused increase in precipitation and the glacier to advance in the 1990s. After 1998, Engabreen shows a slight negative trend in net balance, which led to retreat of the glacier front and increase in elevation of the annual Equilibrium Line Altitude (ELA). The height of the ELA, interpolated from stake measurements, ranges from 840 to 1581 m (i.e. the maximum elevation of the glacier) for the period 1970-2014 and has a mean value of 1086 m a.s.l. (Kjøllmoen et al., 2011).

Surface velocity at Engabreen is controlled primarily by the glacier ice thickness and bedrock slope. The upper plateau flows at a speed lower than 5 cm day^{-1}. The velocity increases to 50 cm day^{-1} on the lower plateau between 900 and 1175 m a.s.l (Jackson et al., 2005), which coincides with the presence of a bedrock trough and the thickest ice ($\sim$ 600 m, Solgaard et al., 2014; Andreassen et al., 2015). In the steepest part close to the icefall, maximum annual surface velocity reaches 70 cm day^{-1} in 2013-2014 (Messerli, 2015), and can seasonally exceed 100 cm day^{-1} (Kohler, 1998, Schellenberger, personal communication). Dragspool measurements performed at the glacier base in winter/spring give a sliding speed of 15 $\pm$7 cm day^{-1} (Cohen et al., 2005) with a maximum recorded value of 27 cm day^{-1} sustained for a 2 hour period (Lappegard, 2006a, p. 43). Thus, sliding contributes to less than 25% of surface velocity. This is significantly lower than the assumed sliding contribution presented in classic glaciological books (Cuffey and Paterson, 2010; Benn and Evans, 2010), but may be caused by differences in measurement period and uncertainty.

3.1.2 Svartisen Subglacial Laboratory

The Svartisen Subglacial Laboratory (SSL) provides direct access to the glacier base since 1992 and offers the unique opportunity to conduct repeated subglacial experiments (Cohen et al., 2000; Iverson et al., 2003; Lappegard and Kohler, 2005) as well as long term monitoring of the subglacial system (Lappegard et al., 2006; Lefeuvre et al., 2015). The laboratory and its living facilities are built in a hydropower rock tunnel beneath Engabreen as shown in Figure 3.1. The tunnel network is divided into two parts: the 'dry' part for carrying out maintenance and research work, and the 'wet' part for the drainage of water. Seven intakes were drilled from the main tunnel (600 m a.s.l.) to the base of Engabreen: six of them in order to capture subglacial water that feed the hydropower plant and the last intake (630 m a.s.l.) to be used for research purpose. The largest volume of subglacial water comes from the three westernmost intakes ($\sim$670 m a.s.l.) that are located 110, 160 and 420m from the load cells (Fig. 3.1). They are situated in the Spiral tunnel that was extended in 1994, after the three other intakes, built in 1992-1993, failed to capture subglacial streams. This was due to the asymmetry of the glacier bed, which differs from classic U-shape glacial valley and what was expected during the boring of the intakes. Engabreen's bedrock is deeper on its western margin.

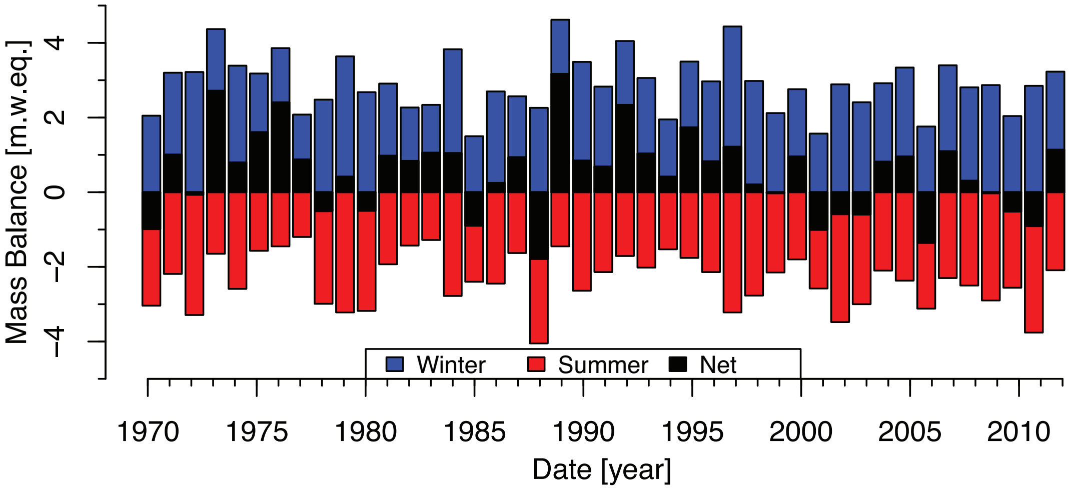

Figure 3.2: Net mass balance of Engabreen (black) with winter and summer components for the period 1970-2012.

The research access is located below about 200 m of ice and is composed of a vertical and horizontal research shaft as shown in Figures 3.3 and 3.4. Both entries to the glacier bed are sealed off to prevent intrusion of ice in the tunnel. The horizontal shaft is blocked with removable metal bars, and the vertical shaft is closed with a table that can slide down a supporting steel structure consisting of four pillars (Cohen et al., 2000). After removal of the bars, it is possible to melt an artificial cavity at the glacier base with hot water (∼ 60°C) heated up with a hot water drilling system. The electric heater of 600 kW at the SSL is similar in power to ice drill systems used in Antarctica to melt boreholes through several kilometres of ice (Blythe et al., 2014). Hot water is pumped from the laboratory to the research shafts and projected with a fire hose at the basal ice in order to clear out parts of the bedrock. The melted artificial cavity varies in size and is usually between 5 and 25 m long, 5 and 10 m wide and exceeding 3 m high. The contraction of the cavity occurs at a mean rate of 0.25 m day^{-1} that is controlled by ice overburden pressure (∼1.8 MPa), and geometry of the cavity. The cavity is also transported downstream due to basal sliding at a rate of 15 ±7 cm d^{-1} (Cohen et al., 2005). Before complete closure of

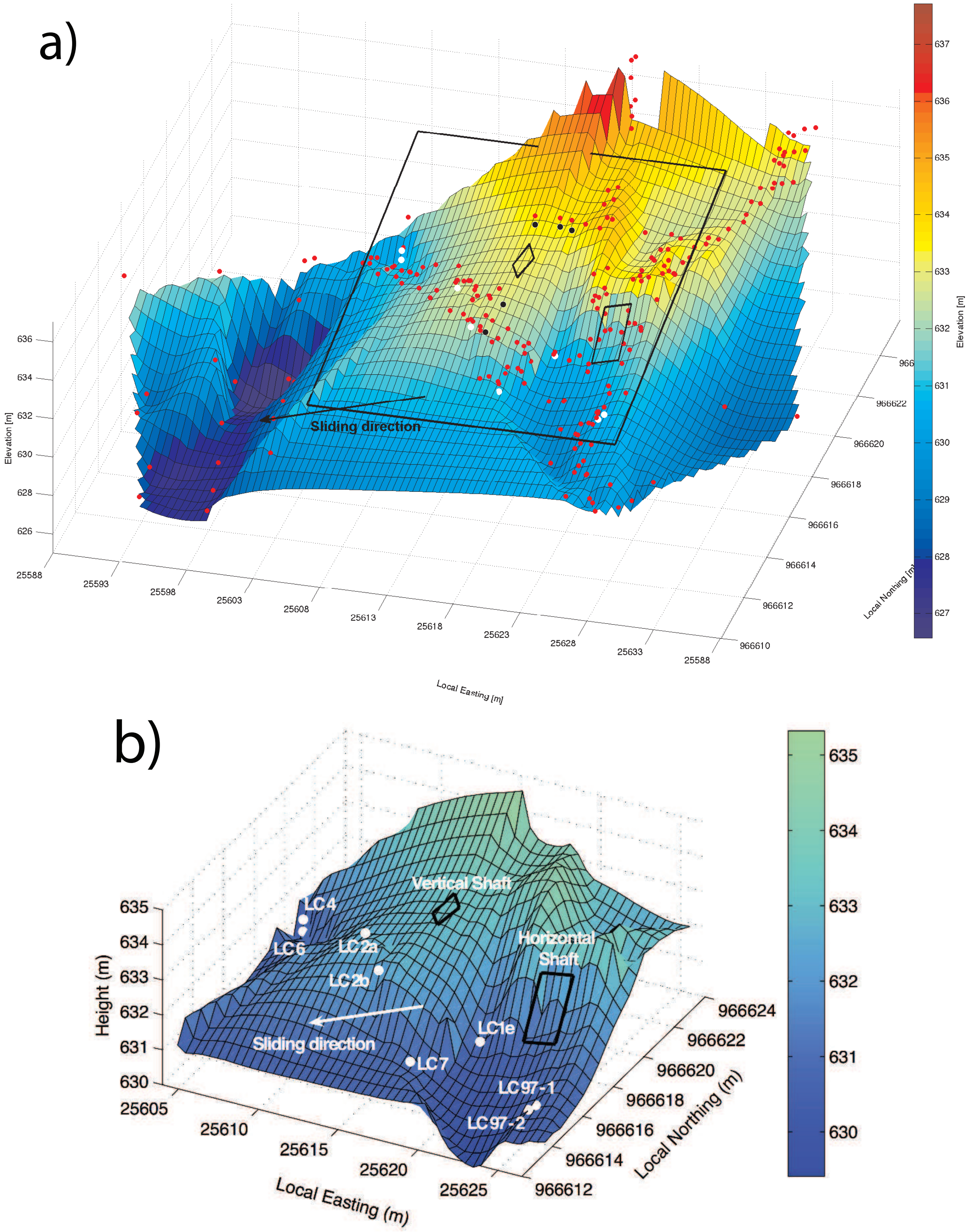

Figure 3.3: a) Map of the bedrock surrounding the research shafts with location of the load cells (white points), boreholes (black points) and shaft accesses (small frames). The red points are topography measurements which elevation is increased by 0.5 m for visualisation purposes. b) The map published in Lappegard et al. (2006) (black frame) is generated from a cubic interpolation of the topographic measurements.

the cavity, work is conducted to install sensors/instrumented panels flush in the bedrock, collect basal ice samples and survey the bedrock topography.

The bedrock surrounding the research shaft was mapped using land surveying techniques in 1992 (e.g. theodolites), and complemented by airborne radar (Kennett et al., 1993). Figure 3.3a shows that the bedrock was mapped along three melted tunnels (aligned red dots) and the elevation of their surrounding is constrained by a few aligned radar points. Local observations indicate that the bed topography is characterised by metre-scale bumps of 1-10 m wavelength more or less perpendicular to the sliding direction. The general slope is about 10°, although melting of ice tunnels showed that the bed topography varies greatly on short distances (e.g. steps of different heights). A vertical cliff separates LC1e located on an almost flat surface at 630 m and the access of the vertical shaft situated on a gently sloping plateau at 633 m. Another cliff, about 4 m high and potentially over-hanging, constrains ice flow 11 m north of the shafts and to the north-west of LC4 and LC6 (Cohen et al., 2000). The cliffs are nearly parallel to the main ice flow direction that is 240°. Striations on the load cells and panels show that flow direction can vary by about 10°(Cohen et al., 2000), although this variation may be due to the closure of melted cavities. The geometry of the cavity may change the local sliding direction producing this variability.

Natural cavities have not been directly observed at the glacier base, but bed separation is seen in time-lapse videos that monitor the closure (and displacement) of the artificial cavity. All melting campaigns are undertaken in early spring and late autumn when natural cavities are not yet opened or already closed. The bedrock exposed near the glacier front shows evidences of cavitation such as carved oxidised scallops and decimetre scale troughs on the lee side of bumps. It is accompanied with carbonate deposits similar to other deglaciated areas (Hallet et al., 1978) created by regelation-sliding processes (Ng and Hallet, 2002) as well as small scale Nye-channels undercutting the undulating bed, and orientated in the direction of former ice flow (Messerli, 2015).

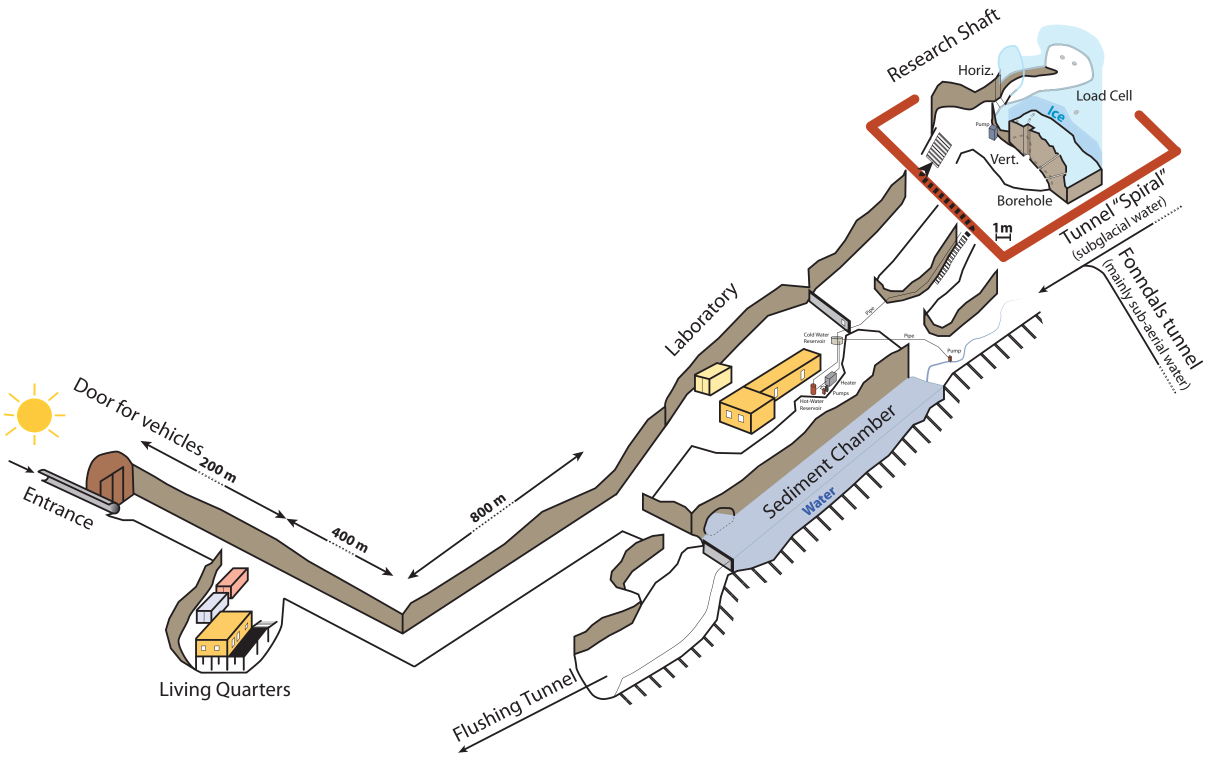
Research Shaft
Horiz.
Load Cell
Ice
Pump
Vert.
Borehole
1m
Tunnel "Spiral"
(subglacial water)
Fonndals tunnel
(mainly sub-aerial water)
Laboratory
Pipe
Cold Water Reservoir
Pipe
Pump
Heater
Pumps
Hot-Water Reservoir
Sediment Chamber
Water
Door for vehicles
200 m
400 m
800 m
Entrance
Living Quarters
Flushing Tunnel

Figure 3.4: Sketch of the Svartisen Subglacial Laboratory (not to scale) showing the entrance to the tunnel (Fig. 3.1) on the left hand side, the living facilities, the laboratory beside the sediment chamber, and a zoom of the research shaft on the top right corner.

3.2 Data Overview

This work investigates the relationship between the surface and base of Engabreen with a focus on load cell data for the period 1993-2013. The pressure data from the load cells are analysed in relation to the hydro-meteorological data (i.e. discharge, air temperature and precipitation) measured at three stations inside the tunnel network and six surface stations close to Engabreen (Fig. 3.5). The location and behaviour of the load cells including a laboratory test on load cell response to distributed forces are discussed in the first part. Then, the characteristics of the hydrological and meteorological stations as well as the data are presented.

3.2.1 Load Cells

Nine load cells are installed flush with bedrock since the end of 1992 in order to monitor the pressure at the base of Engabreen. Load cells are very robust long term sensors that

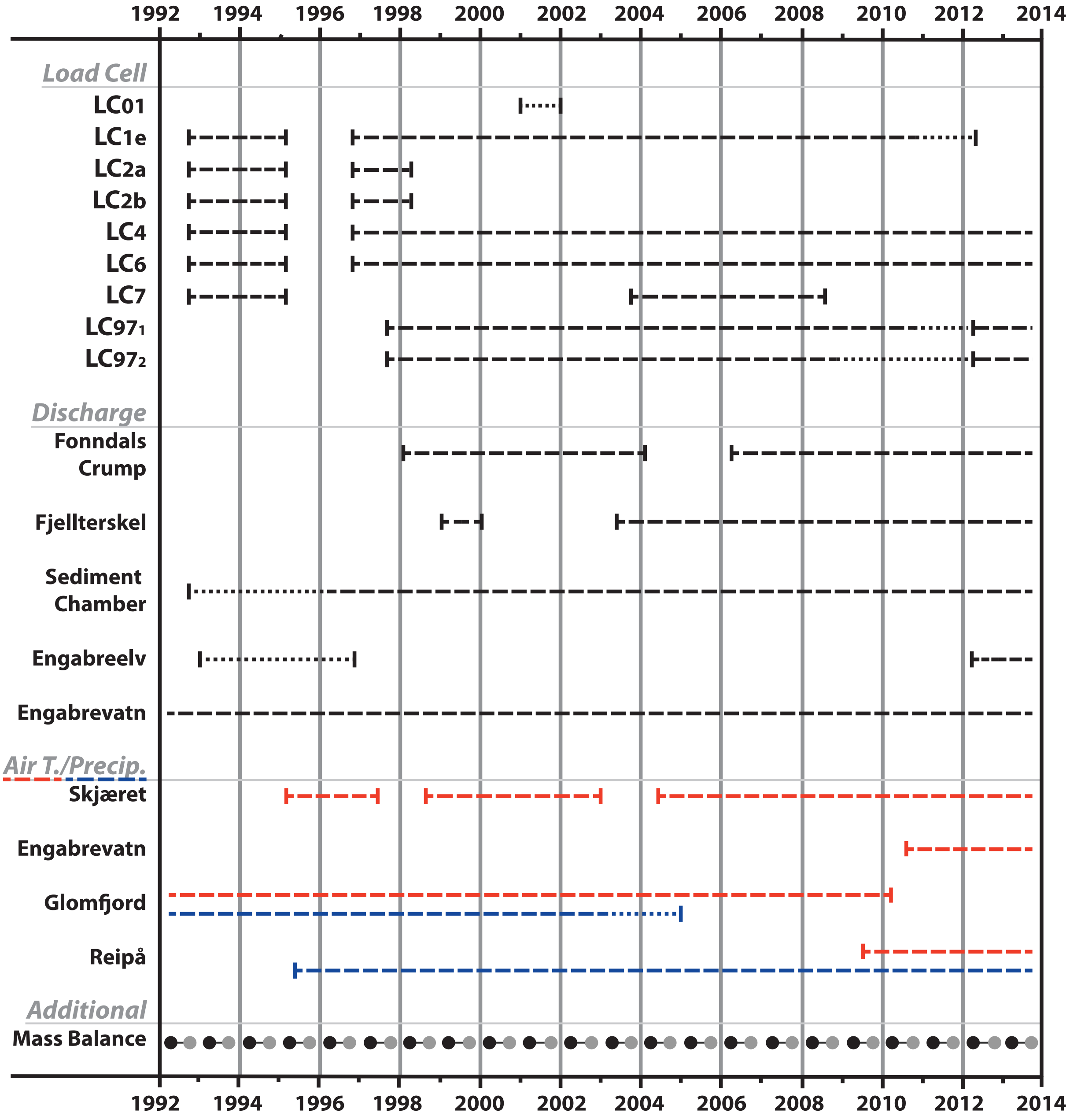

Figure 3.5: Overview of existing pressure, hydrological, meteorological and mass balance data. Dotted line indicate data with poor quality. Red and blue lines represent air temperature and precipitation, respectively. The winter and summer components of the mass balance are shown with black and grey points.

are usually used to monitor earth pressure (water/sediments) within dam and offshore infrastructure. The pressure measured by the load cell corresponds more precisely to the pressure applied normal to the surface of the cell (i.e. normal stress). Since the load cells at the SSL are placed at the ice/rock interface, the normal stress on the load cell is controlled by ice overburden pressure, local slope, ice flow including sliding, and the presence of water and rocks (Cohen et al., 2000; Lappegard et al., 2006; Lefeuvre et al., 2015).

The load cell is composed of an encased plate under which a wire is maintained under tension between two vertical pins. The wire vibrates at a frequency that depends on the distance between the two pins and the load. As load increases the plate bends inward and the two pins below bend outward, increasing the distance in between them and thus the frequency. The load cells are individually calibrated by the manufacturer (Geonor A.S., Oslo) over a range of 0-5 MPa at a temperature of 1°C, with a non-linear error less than 1 % and tested for pressure up to 9 MPa. The two used models are P-100 and P-105, which have a plate diameter of 10 and 15 cm, respectively. Orientation, location and model type of the load cells are given in Table 3.1.

Environmental noise affecting the load cells at the glacier bed depends on the exposure of the load cells to an active subglacial drainage, and the intensity of subglacial hydrological changes. The magnitude of the error created by the noise is estimated to be less than 0.05 MPa for LC97_1 and LC97_2 and to 0.001 MPa for LC4 and LC6 over a week in July 2003 (Paper II). The other type of observed noise in the load cell data is due to deterioration of the state of the load cell, mainly caused by overloading, frequency of loading cycles, fatigue of the wire, and stress concentration (DiBiagio, 2003). This instrumental noise increases over time for several load cells due to their location and exposure to seasonal changes in pressure. Rapid and strong variations in pressure can reach the limit that the load cell can withstand, thereby affecting the quality of the signal. For instance the noise in LC97_1 signal increased after it underwent an overloading of >8 MPa on 26th August 2004, possibly due to a rock dragged across the load cell.

All load cells, except LC01, monitored changes in normal stress at the glacier bed over years as shown in Figure 3.5 and Paper I (Fig. 3). The load cell are installed within an area of 20 m long and 5 m wide with the longest axis approximately perpendicular to the general sliding direction of 240°. Their location was determined by the existence of rock boreholes connecting the rock tunnel to the glacier bed, and drilled during construction to assess the distance from the ice. The load cells are installed flush with the bedrock close to these boreholes that are used to exit the 50 m long load cell cables. The cables

Load Cell	**Orientation [°]**		**Dist. from LC6 [m]**		**Tech. details**	
	Azimuth (±10°)	Tilt	Horizontal	Vertical	Model	Number
LC1e	180	31	15.3	0.1	P-105	36892
LC01	-	-	-	-	P-105	37892
LC2a	170	13	7.2	2.0	P-100	34892
LC2b	-	0	10.1	1.9	P-105	36792
LC4	170	125	0.4	1.1	P-100	34792
LC6	140	12	0	0	P-100	34992
LC7	190	13	13.6	0.2	P-105	36992/37992
LC97_1	250	9	21.3	0.1	P-105	37692/37092
LC97_2	250	14	21.1	0	P-105	38292/38092

Table 3.1: Load cell characteristics

are then wired to a single Campbell CR10 data logger located in the laboratory. The load cells are preferentially placed on the lee sides of the uneven bedrock, although LC7, LC2a and LC2b are more exposed and their plates have an azimuth parallel to the sliding direction (Table 3.1). The sampling rate is generally 15 min and the value is stabilised for 8 sec before being recorded. Data were sampled at a 2 min interval for periods shorter than two weeks when experiments were in progress and in 2012-2014. Problems with the power supply and data logger malfunctions caused gaps affecting all load cell time series as shown in Figure 3 of Paper I.

Load cells of vibrating-wire type offer the advantage of reduced long-term drift (DiBiagio, 2003) and, compared to instrumented ice boreholes, of fixed location at the glacier base thereby disregarding problems caused by ice flow and surface melt. The transport of boreholes can modify the height of the borehole water column (i.e. controlled by water pressure at the glacier bed) by conveying boreholes over bedrock with different levels of basal connectivity and thus pressure. Basal water pressure in boreholes is also affected by surface and englacial inflow of surface melt (Gordon et al., 2001; Harper et al., 2010), which surface contribution stops when the top of boreholes freezes up because of negative air temperature or cold ice. These effects are often neglected, although they have an effect on water pressure measured in boreholes. The installation of load cells at the glacier base avoids these issues and show instead some sensitivity to the long term drift of the zero frequency. This drift can be estimated at Engabreen while the load cells are uncovered

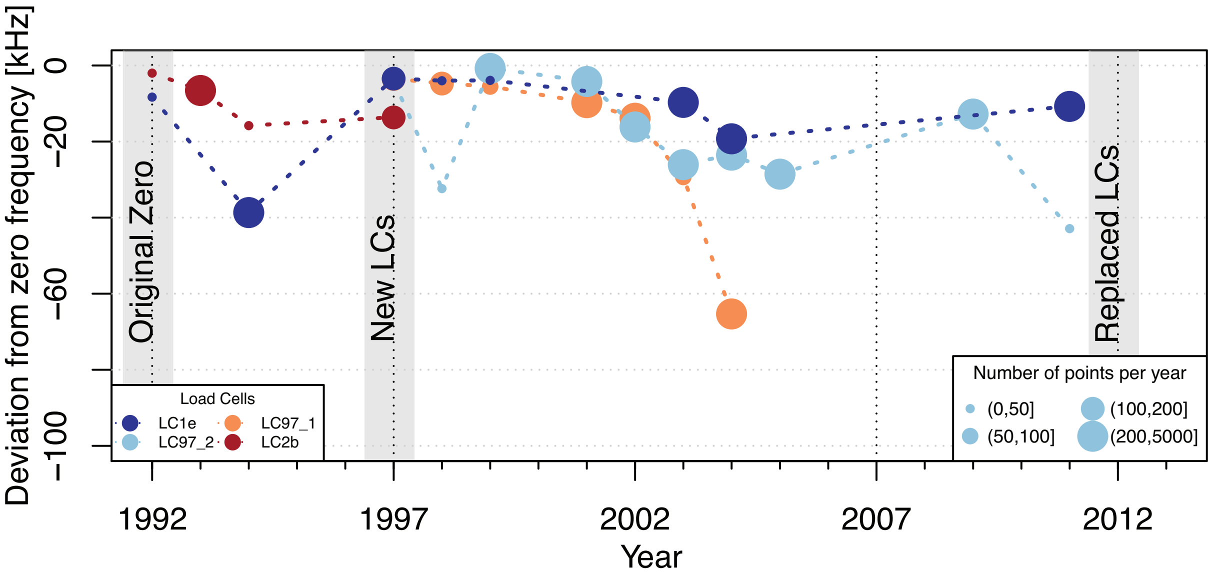

Figure 3.6: Temporal variation in annual drift of the zero frequency (median values) for four load cells: LC1e, LC2b, LC97_1 and LC97_2. The size of the points reflect the number of used values from the 15 min interval records. The grey boxes highlight the installation of LC1e and LC2b in 1992, and of LC97_1 and LC97_2 in 1997 as well as their replacement in 2012.

after melting a man-made cavity or during the presence of an atmospheric pressure cavity or channel. However, only load cells the closest to the horizontal research shaft, located on the lee-side and in a hydrologically active zone (e.g. LC 97_1, LC97_2, LC1e and LC2b), have been uncovered. Frequencies lower than the zero frequency are extracted, and filtered to exclude periods showing drops in frequency >100kHz (up to 2000 kHz) either caused by data logger problems or failure of the load cells. The median of the annual values for the period 1993-2013 show a roughly linear decrease in zero frequency that accelerated slightly after 2003 for unknown reasons as shown in Figure 3.6. This rough estimate of the drift is not accounted for in the following analysis, but it does not impact this study as the primarily interest is to understand short-term variations in pressure, when the drift in zero frequency can be neglected.

3.2.2 Load Cell Experiment

A laboratory experiment was conducted to assess the effect of heterogeneously distributed forces on the load cell plate, and to understand what the load cells really measure. The aim is also to test whether the load cells can measure negative pressure (frequency lower than the zero frequency), a question raised by Lappegard (2006a). It is suggested that negative pressure can also be caused by a drift in zero frequency.

An hydraulic press was used to apply a load of 500 kg on the load cell with three different contact areas. This experiment consisted in applying the load over the entire 15 cm diameter plate of the load cell, then at 5 locations on the plate using a 5 cm diameter piston and finally at 37 points on the load cell plate with a bolt of 5 mm diameter. The results, presented in Figure 3.7a, show that the pressure recorded by the load cell varies by one order of magnitude, when the load is not homogeneously distributed (i.e. for the point applied force in colour and piston applied one in grey circles) and can even give negative pressure. The local highs of the standard deviation of the measurements highlight the problem (Fig. 3.7b). The variability is concentrated at two points, which are inferred to correspond to the positions of the two vertical pins fixed below the plate. For a force applied at points in between the pins, the result is positive because the plate bends inward and the distance between the pins and the frequency of the wire increases (inset in Fig. 3.7). However, as the force is applied to the periphery of the load cell plate, the frequency and calibrated pressure decreases and even produces negative values along the axis of the wire (Fig. 3.7). This describes the sensitivity of the uniaxial wire instrument that was built to measure hydrostatic pressure homogeneously distributed over the plate. At the SSL, the ice is inferred to be resting uniformly at the bed, but occasionally debris dragged along the bed concentrates the force and may affect the load cell measurements in a similar way to that shown by this experiment. Opening cavities and channels are supposed to affect larger areas than the 10-15 cm plate of the load cell, and thus their effect is not significant.

The load cell experiment and the drift in zero frequency show that the measurement of magnitude of the normal stress is not straightforward. The magnitude given by the load cell also varies with bedrock slope, presence of water, and stress transfer when the glacier bed is not fully in contact with bedrock. Despite these issues, the load cell data still provide a wealth of information about the temporal changes in bed conditions. Synchronous variations in pressure across the load cell network are of particular interest as they can identify the cause of subglacial changes, the extent of their impact, and the proximity of the involved processes based on spatial correlation in pressure between the load cells (Paper I and II).

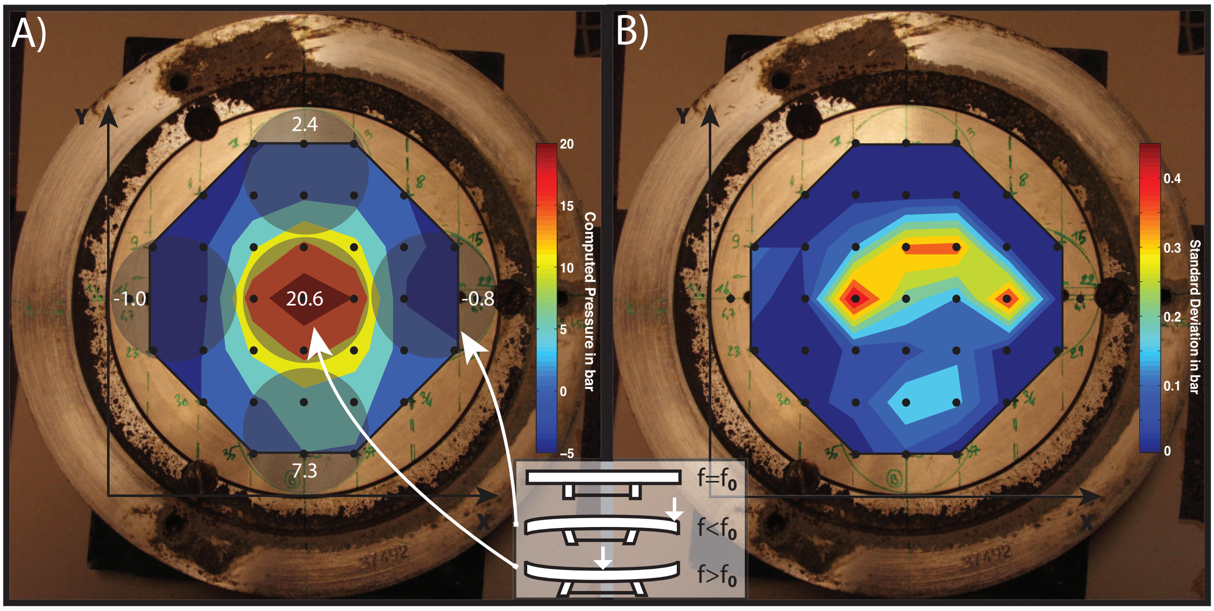

Figure 3.7: a) Results for point-applied (colour) and piston-applied (shaded circles and numbers) 500 kg force. When the force is applied over the whole plate, the load cell measures a pressure of 18 bars. b) Standard deviation from three repeated measurements for each point.

3.2.3 Hydrological Data

Hydrological discharge is measured at four stations, which are operated by the Norwegian Water Resources and Energy Directorate (NVE). Two stations are located in the proglacial area of Engabreen, one at the proglacial lake, Engabrevatn (station 1), and one at the proglacial stream, Engabreelv (station 2). The two other stations are installed inside the tunnel network underneath Engabreen one at the sediment chamber (station 3) and one inside Fonndals tunnel, upstream of the sediment chamber (station 4).

The water level of the proglacial lake Engabrevatn (8 m a.s.l., lake elevation is 10 m a.s.l.) has been monitored with a sub-daily resolution since 1969 and a hourly resolution since 1994. The water level is calibrated to the discharge from the northwest outlet stream (NVE, Station 1 in Fig. 3.1). The drainage catchment is 53 km^2 and is 73 % glaciated (NVE's database Hydra2).

The discharge at Engabreelv (15 m a.s.l.) was measured between 1993 and 1997 before the discharge station was overrun by Engabreen glacier during its readvance. The station was re-installed in 2012 at the same location as before about 300 m downstream from the glacier front, and records at an hourly interval as shown in Figure 3.1 (station 2). The rating curve for discharge is accurate for low to medium discharge. However, high discharge is over-estimated because the geometry of the river at the station changes significantly and few measurements are available to constrain the rating curve (Astrid Vatne, NVE, personal communication). Discharge at this station responds greatly to melt occurring on the tongue of Engabreen and is used to identify the timing of spring speed-up events (Messerli, 2015).

Station 3 measures discharge flowing through the Sediment Chamber (609 m a.s.l.). The chamber collects sediment and meltwater mostly from Engabreen between 825 and 1581 m a.s.l. of surface elevation and over an area of 33 km^2. Water is captured through three intakes (Section 3.1.2), and is then routed through the 'wet' part of the rock tunnel network (Spiral tunnel) to the Sediment Chamber. A smaller volume of water comes from a 17 km^2 catchment located west of Engabreen and 83% glaciated. It is routed to Fonndals tunnel, where is installed station 4, and then to the Sediment Chamber downstream. The low flowing water in the Sediment Chamber allows sediment to settle there and thus prevent them from being transported to the turbines of the hydropower plant. Discharge data was first recorded in 1992, and is continuous only from the end of 1996 with an hourly sampling rate. The rating curve was constructed from measurements conducted in the 'wet' tunnel between the junction of Fonndals-Spiral tunnels and the start of the Sediment Chamber (Fig. 3.4). The rating curve is uncertain for discharge >30 m^3 sec^{-1} due to the geometry of the outflow from the sediment chamber that is composed of an exit tunnel and a flushing tunnel (Fig. 3.1 and 3.4). The rating curve accounts only for the exit tunnel that leads water to the power plant, however the capacity of this tunnel is not large enough to accommodate large volume of water when the discharge is >30 m^3 sec^{-1}. Water, then, backs up in the sediment chamber and flows into both tunnels, the exit tunnel that is overwhelmed, and the flushing tunnel that evacuates the excess. This configuration is not taken into account in the rating curve, thus discharge data >30 m^3 sec^{-1} are ignored. The discharge from the Sediment Chamber is used to estimate the subglacial contribution from Engabreen, as described below.

Two stations are installed in Fonndals tunnel: Crump at an elevation of 615 m a.s.l. and Fjellsterkel at an elevation of 614 m a.s.l. located 225 m downstream from Crump. The discharge there originates from the catchment west of Engabreen. The rating curve is constructed from data collected at low discharge, when these stations are accessible. Nevertheless, the simple geometry of the tunnel leads to relatively good hydraulic calculations for higher discharge (NVE). A single continuous time series for station 4 is created by merging the 1-2 hour interval data from these two stations because of their proximity and no change in hydrology inside Fonndals tunnel. It also enables to fill gaps (instrument/battery failure) at one station using the other for the measurement period 1998-present. Crump lacks data for 2002, and the period 2004-2006, whereas Fjellsterkel lacks data for 1998, 2000-2002, and 2012. During overlapping measurement periods, the difference in discharge between the two stations is 67% between -0.25 and 0.25 m^3 s^{-1}, and 28 % between 0.25 and 1 m^3 s^{-1}, with discharge measured at Crump generally being higher than Fjellsterkel. When discharge is measured concurrently at the two stations, an average discharge is used. Hence, 95% of the difference in discharge measured is < 1 m^3 s^{-1} and this constructed series is suitable for this study.

Two tunnels contribute to the discharge at the Sediment Chamber, Spiral and Fonndals tunnel, that collect water from the subglacial intakes under Engabreen and from the catchment west of Engabreen, respectively (Fig. 3.1 and 3.4). The subglacial discharge of Engabreen is calculated by subtracting the discharge measured at the Sediment Chamber (station 3) and at Fonndal (station 4), thus giving the discharge coming from Spiral tunnel. The discharge at stations 3 and 4 are highly correlated (0.7) for discharge <12 m^3 s^{-1} at station 3 and <4 m^3 s^{-1} at station 4 because they both collect meltwater from highly glaciated catchments that are adjacent. The catchment size, delay due to transport and rating curve issues, mentioned earlier, explain the decrease in correlation for high discharge. Fonndal's contribution to the discharge measured at the Sediment Chamber is approximately 33% in summer and 67% from December to May. This difference expresses a greater contribution to discharge from Engabreen's catchment in summer perhaps due to a glaciated catchment twice as large as the catchment collected in Fonndals tunnel. Another cause could be the delay in discharge peak due to transport of meltwater through the subglacial system (i.e. changes in drainage efficiency) or the tunnel network. A running auto-correlation with one day window for the 1998-2014 period demonstrates that discharge at Fonndal increases 1-2 hour earlier than the discharge at the Sediment Chamber in winter whereas it is 1 hour delayed in summer and synchronous in spring and autumn. As presented and discussed in Paper II, it is still possible to postulate that Fonndal is partially dependent on variations in subglacial discharge, however the magnitude may not be correct. This remains, during periods of high discharge, a complement to the 1-2 hour resolution computed subglacial discharge that spans from 1998 to 2014.

3.2.4 Meteorological Data

Hourly air temperature and daily precipitation data are available from five meteorological stations near Engabreen (Fig. 3.5). As shown in Figure 3.1, the station at Skjæret (1364 m a.s.l.) is located on a nunatak in the accumulation area of Engabreen; the station at Engabrevatn (8 m a.s.l.) lies on the north side of the proglacial lake, the stations in Glomfjord (39 m a.s.l.) and at Synkhøyden (800 m a.s.l.) are both 18 km northeast of the SSL at the end of a fjord and inland (see fig. 3.5); and Reipå (9 m a.s.l.) is 27 km northwest and near the coast.

Skjæret is an automatic weather station installed in 1995 by the Norwegian Water Resources and Energy Directorate (NVE). It records air temperature at an hourly interval, but has data gaps in 1997-1998, 2003-2004 and 2012. The precipitation record, covering the period 1999-2008, is not reliable. It is challenging to measure precipitation because the station is on a nunatak and because of the high winds there. Moreover, snow is strongly redistributed by the wind on the upper plateau of Engabreen (Kjøllmoen et al., 2011). Thus, the precipitation data are not used in this study. An additional air temperature sensor was added in Skjæret in September 2008 with an overlap period of a few months with the older sensor. During the overlapping period, the histogram of the difference in temperature is centred around -0.3 °C and follows approximately a gaussian distribution. The two time series are averaged for the overlapping period and merged otherwise in order to produce a continuous hourly time series covering the period 1995-present.

Glomfjord is the closest weather station maintained by the Norwegian Meteorological Institute (NMI) and has temperature records from 1916 to 2010 as well as precipitation records from 1916 to 2004. For the period 1992-2014, the temperature data are mainly at an hourly resolution, except prior to 1997 that have a sampling rate of a day. Precipitation data was recorded until 2004, although the quality deteriorates after 2003 when a new precipitation station was installed (NMI's database, eKlima). The measurements consist of total precipitation over a period of 24 hour and are made at a daily interval, and at an hourly interval since 1997. Due to large variation in topography, it was not known how representative the meteorological station was, and the station in Glomfjord was fully discontinued by NMI in 2010, although it had an exceptionally long time series starting back in 1916.

The weather station at Synkhøyden records air temperature at an elevation of 800 m a.s.l., which is approximately equal to the height of the glacier surface above the SSL. The station is maintained by the hydropower company Statkraft, which provided mean daily air temperature since 1997 for this study, although the station records at hourly interval. Data gaps in the data are filled from spatially extrapolated air temperature measured at neighbouring stations (Statkraft). Most of the affected periods are only hours to days in length.

The station at Reipå has recorded daily precipitation since 1995, then it was upgraded to an automatic weather station in 2009 by NMI. Air temperature and precipitation are presently recorded hourly and daily, respectively. This station has the most reliable precipitation data over the past 20 years and thus is the primary source of the precipitation data used in this study, even though it is located 27 km from Engabreen. The weather is assumed similar if wind and precipitation come from the Atlantic Ocean because their distribution is likely to be homogeneous before it reaches Engabreen and Reipå. If wind and precipitation come instead from the interior of the country, precipitation will be more variable due to local topography that affects their spatial distribution. The difference in precipitation at Reipå and Glomfjord between 1996 and 2003 shows that station in Reipå underestimates by half the precipitation in Glomfjord. Nevertheless, their correlation is high (0.8) and the mismatch of rainfall event occurring when a station measures rain and the other does not indicate a mean error of 0.5 mm and maximum of 24 mm. Thus, the precipitation recorded at Reipå station can be used as a first order estimate for the timing in precipitation at Engabreen, although the magnitude is likely underestimated by half.

The discharge station at the proglacial lake Engabrevatn was added an air temperature sensor in May 2012. The data are recorded at an hourly resolution and provided local air temperature measurements of interest for field campaigns conducted at the glacier surface between 2012 and 2014 (Messerli, 2015).

Chapter 4

Temporal Variations in Subglacial Conditions from Load Cell Records

Load cells,
after 15 years
at the glacier bed

4 Temporal Variations in Subglacial Conditions from Load Cell Records

The stress regime at the glacier bed varies according to changes in driving stress, subglacial hydrology, ice dynamics and contact between basal debris and bedrock (Clarke, 2005). These factors control the response of the load cells on different time scales: annual, seasonal and daily. These temporal changes are investigated in order to characterise and determine the cause of pressure variations based on the shape and the magnitude of pressure events, the timing of fluctuations in pressure, spatial variations across the load cell network and production/routing of surface meltwater.

A load cell measures normal stress acting perpendicular to the plate and the bed surface. It differs from ice hydrostatic pressure because the load cells are inclined and flush with the bedrock. The normal stress on the bed also responds to changes in the glacier stress regime that depend on sliding and deformation. The variation in normal stress measured by the load cells represents a combination of effects caused by ice, water and debris. Ice is assumed to cover the load cells when pressure is higher than the mean local overburden pressure (Lefeuvre et al., 2015). The presence of water is deduced when the load cells measure rapid decrease in pressure or exact same pressure. The transit of clasts over the load cell network leads to temporally and spatially isolated events that are not correlated with hydrological changes.

Load cells respond differently depending on their location relative to the efficient part of the drainage system and proximity to subglacial cavities. The characteristics of the pressure change reflects whether the load cells are located in an isolated or connected hydrological drainage system. Although the response in the two systems is different, the cause may be the same (Murray and Clarke, 1995, Paper II). Pressurisation in the connected subglacial drainage system can, for example, lead to an anti-correlated pressure response in the unconnected system. Moreover, this response is controlled by the connectivity and capacity of the subglacial hydrological drainage system thereby causing each event to be different in shape and intensity (Iken and Truffer, 1997; Lappegard et al., 2006; Andrews et al., 2014; Lefeuvre et al., 2015).

Directly linking the load cell response to these hydrological processes is challenging as several processes act simultaneously. Hydrological processes, basal sliding, opening of cavities and stress redistribution in the ice produce comparable pressure signals due to the feedback between subglacial hydrology and ice flow (Iken and Bindschadler, 1986; Schoof, 2010). The feedback arises as water pressure at the glacier bed increases, decreasing basal friction and increasing basal sliding, which leads to opening of subglacial cavities and a decrease in water pressure at the glacier bed. This chapter investigates the relationship between subglacial hydrology and ice mechanics from the perspective of time series of basal pressure at the load cells. The aim is to identify the processes causing variations in pressure.

Lappegard et al. (2006) studied the pressure data from the load cells for the period 1993-2003 and characterised qualitatively the general temporal variations of the response of the glacier bed. The main observations and findings can be summarised thus:

1. The pressure time series are characterised by pressure events that are divided into ”global” and ”local” events. The types of pressure events define the degree of connectivity in response across the load cell network and are described as follows:
    a) **Pressure events** are ”distinct, short-duration pressure minima, usually followed by sharp peaks” and are concurrent with the input of surface melt either during warm stable weather or from rainfall. In summer they usually commence in the middle of the afternoon, the minimum is reached 4-5 hours later and a peak in pressure at midnight is followed by a gradual decrease until pressure returns to its background level in the early morning.
    b) **”Local” events** are pressure events that are observed at a few load cells only, and mainly in summer.
    c) **”Global” events** are pressure events that are measured at all load cells. Global events dominate the winter and spring regime.
2. Seasonal variation in pressure is characterised by the length of delay between surface melt and load cell response, change in subglacial hydrology, and amplitude and frequency of pressure events.
    a) **The Winter regime** has few high-intensity events, which lag melt or rain at the glacier surface. Usually, all the load cells respond simultaneously (i.e.

”global” events). This behaviour and generally high pressure indicate that the load cells measure a system isolated from the drainage system, which is composed of a linked cavity system and thin water film at this time of the year.

b) **The Summer regime** is characterised by high activity at the glacier base recorded at the load cells and linked to surface melt. Daily pressure events are often of low amplitude and triggered synchronously with the daily maximum in discharge gradient. This indicates that the critical capacity of subglacial channels is reached (flooding of the bed and over-pressurisation). The intensity in the load cell response depends on the degree of interconnectivity between channels and the unconnected system.

This study analyses the same data as Lappegard et al. (2006), but extends the dataset by 10 years and statistically quantifies the temporal distribution of pressure variations. I investigate pressure events at an inter-annual, annual and seasonal scale (Paper I) as well as at an event scale (Paper II). The statistical analysis of pressure variations recorded at the glacier bed provides a quantitative estimate of the behaviour of the glacier bed and is presented in the following section (section 4.3).

4.1 Paper I: Seasonal Variation of Basal Connectivity

Subglacial changes are usually investigated based on specific pressure events and melt periods. However, the glacier bed response shows persistent spatial variability across the load cell network over the course of a season that demonstrates the importance of subglacial connectivity as shown in Paper I (Lefeuvre et al., 2015). Connectivity defines parts of the bed that are connected hydrologically via the subglacial drainage system (e.g. linked cavity system or channelised system) or that respond synchronously to mechanical stress transfer within the ice caused by pressurisation of the hydrological system. These spatial variations and the importance of the melt season are investigated in Paper I (Lefeuvre et al., 2015) by applying a running correlation to the load cell data in order to assess the temporal variation and control of subglacial connectivity regardless of specific pressure and melt events.

The study provides a comprehensive continuous assessment of the spatial connectivity in pressure across the load cell network on a seasonal scale. A running correlation is computed between LC6, the reference load cell, and the other load cells over the entire measurement period. The correlation and connectivity between sensors show that:

1. The monthly distribution of the correlation coefficient (Fig. 6 in Paper I) differentiates the winter and summer regimes. The winter regime is defined by a high variability in correlation coefficient as well as low correlation values. In contrast, summer is characterised by highly correlated pressure between load cells and little loss in signal coherence. The glacier bed response is homogenised during melt season due to an increase in hydrological connectivity, transfer of stress from the efficient drainage system to the unconnected system, or an increase in bed decoupling and basal sliding. These phenomena enhance synchronous variations in pressure at the glacier bed, and reduce the effect of debris and local ice flow on basal pressure. The hydrological connectivity probably dominates as variations in connectivity and discharge are shown to be strongly related.

2. The transition in connectivity from winter to summer regime (i.e. spring) is more gradual than in autumn. The hydrological system develops slowly in spring as meltwater is stored in the snowpack at the glacier surface and is not efficiently routed to the glacier base. The transition in autumn is more abrupt. It reflects the lack of surface storage of meltwater, and the contraction of the efficient drainage system as melt decreases. The closure of the drainage system leads to a rapid return of a winter regime dominated by local processes.

3. The correlation in pressure across the load cell network increases in summer. However, anti-correlated variations in pressure between load cells are seen during pressurisation of the efficient drainage system. Two contrasting summers are examined: summer 2000 with highly correlated pressure (Fig. 7 in Paper I) and summer 2003 with an anti-correlated pressure signal (Fig. 8 in Paper I).

    a) The anti-correlation in 2003 (Fig. 8 in Paper I) is caused by pressurisation in the efficient drainage system and stress redistribution in the hydrologically isolated surroundings. The cause of the anti-correlated pressure signal is due either to load transfer or passive opening of cavities. Load transfer occurs when a pressurised channel supports the load of the overlying ice and thus decreases the pressure on the bed in the immediate surrounding (Paper II). Opening of passive cavities originates from a transmission of basal sliding generated by a pressurised efficient system that decreases normal stress on the lee sides of bumps, where a cavity forms (Andrews et al., 2014).

    b) The correlation in 2000 is instead characterised by a homogenous response in pressure over the entire network (high positive correlation). The process of load

> transfer, identified in 2003, explains this behaviour assuming that all load cells are located in the unconnected drainage system and respond to a pressurisation of the nearby efficient system. A low and continuous summer melt enhances a stable drainage system that is in balance with the production of meltwater. Pressurisation of channels occurs repeatedly as they are close to steady-state, and do not migrate over the load cells, thus increasing basal connectivity.

The basal connectivity is controlled primarily by the extent and intensity of the melt season. Melt water homogenises the response of the load cells regardless of the sign in correlation (i.e. connection to subglacial channels). Anti-correlated spatial variation in pressure shows that stress transfer in the ice causes mechanical connectivity at the glacier base. This enhanced homogenisation in basal pressure across the load cell network extends the spatial representation of the pressure measurements by decreasing the effect of local processes. However, pressure response can still vary over distances shorter than a few metres due to the variations in correlation of the pressure signal and high pressure gradient.

4.2 Paper II: Anti-Correlation in Pressure by Load Transfer

Anti-correlation in pressure between load cells is a recurrent feature in the pressure records. However, this feature occurs irregularly over time and may last for only one day or as long as several weeks. This distinct behaviour at the glacier base holds critical information for identifying the processes that control basal pressure.

The aim of Paper II is to test whether load transfer explains the observed spatial anti-correlation in pressure. The study examines one month of pressure variations and hydro-meteorological data in July 2003 during which successive anti-correlation episodes occur. The cause of the anti-correlation is inferred to be a pressurised efficient system that redistributes the stress at the glacier base between the efficient and unconnected drainage system. A full Stokes model of viscous ice reproduces variations in pressure of about 10 kPa as observed during periods of diurnal melt. It simulates the anti-correlation in pressure at the glacier bed by creating a compression regime between two pressurised subglacial channels that support the load of the ice in between them.

The results are a preliminary model of load transfer which successfully reproduces anti-correlation in pressure at the glacier base. Several critical simplifications are made, including the assumption of a flat bed, absence of hydraulic jacking, viscous flow of ice instead of elastic displacement for short timescales and the sensitivity to the lateral boundary conditions. Nevertheless, the timing and out-of-phase response are reasonable and the analysis demonstrates that this is a worthwhile approach for investigating anti-correlation at the glacier bed. Rapid triggering of a pressure event was not investigated using this model. This is a more complicated process, and would need a more complex model to faithfully reproduced the observed response. This modelling suggests several promising directions for future work such as the relationship between pressurisation in the cavity and subglacial hydrology.

4.3 Pressure Events

Pressure events are short-term perturbations from the background level of normal stress and are characteristic of load cells measuring the isolated drainage system (e.g. LC4 and LC6). These observations are valuable in understanding how unconnected parts of the glacier bed respond to the input of surface melt and to the development of the hydrological system.

The pressure events are first identified manually and classified qualitatively to give an understanding of the complexity and diversity of the response of the subglacial system. A process for automatic identification of the pressure events is then developed based on the characteristics of the manually extracted events, and applied to the entire measurement period of the data from LC6 and LC4. Variations in timing as well as amplitude of the events are quantified and discussed. Finally, the typical shape of the pressure events is determined from a principal component analysis.

4.3.1 Manual Identification and Classification

The manual identification of pressure changes recorded by the load cells includes pressure events as defined by Lappegard et al. (2006), as well as events where the pressure fluctuates rapidly (Fig. 4.1). A broader spectrum of events is thus investigated. The manual identification is conducted on only part of the data record from LC6: the 1996-1998 period that overlaps with the data examined by Lappegard et al. (2006), and the most recent data from 2008-2012.

The pressure perturbations are classified visually following geometrical criteria (Fig. 4.1). The nine event types are defined as follows: 1) a drop and sharp rise of strong

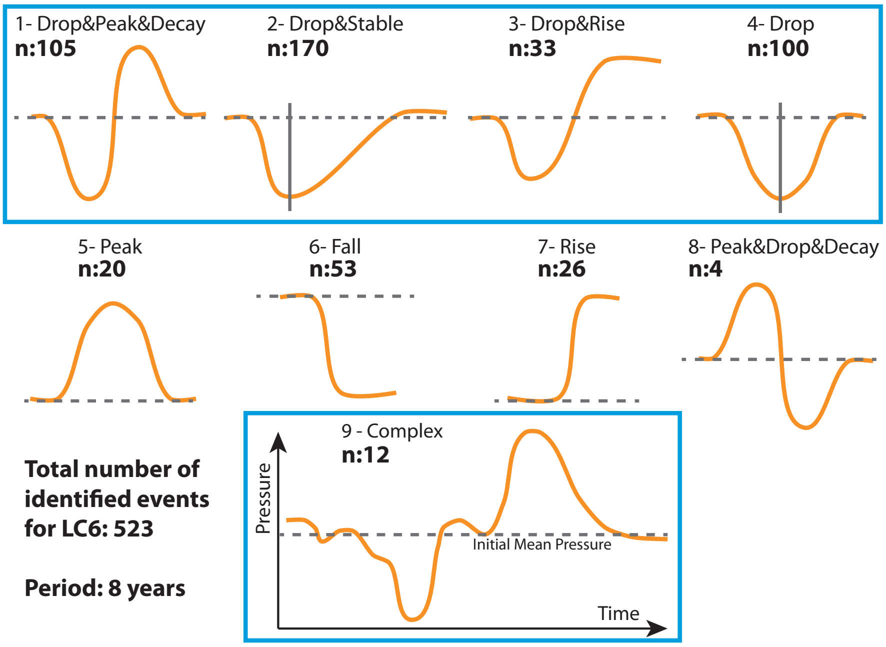
1- Drop&Peak&Decay
n:105
2- Drop&Stable
n:170
3- Drop&Rise
n:33
4- Drop
n:100
5- Peak
n:20
6- Fall
n:53
7- Rise
n:26
8- Peak&Drop&Decay
n:4
Total number of identified events for LC6: 523
Period: 8 years
9 - Complex
n:12
Pressure
Initial Mean Pressure
Time

Figure 4.1: Qualitative classification of types of pressure events (blue rectangles) and other observed perturbations. The abundance of each type is based on visual examination of the records from load cell LC6 and covers a period of eight years between 1996 and 2013.

intensity followed by an exponential decay in pressure, 2) a modest asymmetric drop with the absence of a sharp maximum, 3) a drop and a rise reaching higher pressure than at the start of the event, 4) a symmetric drop and rise, 5) a peak in pressure only, 6) a sharp fall in pressure, 7) a rapid rise in pressure, 8) a peak followed by a drop and 9) a complex event with several drops and one or more peaks, usually lasting more than one day. Only types 1 to 4 and 9 are in agreement with the definition of pressure events in this study. The other types (5-8) are distinct disturbances of pressure at the glacier bed, and are discussed in relation to the spring melt events in section 4.4.

In total, 523 events were manually picked and classified. The pressure events defined by a drop and rise in pressure (blue rectangles in Fig. 4.1) are composed of 105 high-intensity events of type 1, and 203 low-intensity events of types 2 and 3 (170 and 33 events, respectively). Type 1 is characteristic of the largest events, which occur mainly in spring and autumn. Types 2 and 3 are similar to type 1, but with a less pronounced or absent maximum. Type 4 is composed of a single minimum; the 100 identified type 4 events often succeed each other and are sometimes superimposed on larger pressure events. Event types 1-4 are assumed to be triggered by the same process that leads to a drop in pressure. However, the occurrence and intensity of the peak or maximum varies.

It appears to be influenced by the magnitude of the preceding pressure minimum as well as the frequency of pressure events. The absence of a maximum in type 4 can be due to a rapid succession of pressure events that inhibits a relaxation of stresses at the glacier bed and a peak in pressure. Event types 5 to 8 are more unstable and not as common, only 103 events out of 523 in an eight-year period. They occur outside the summer season and rarely consecutively. When pressure events (1-4) and perturbations (5-8) cannot be clearly distinguished due to several events happening in succession (amalgamation), they are classified as type 9 (nine events). These events persist about a week and are typical of the bed response to spring melt events and autumn rainfall events (section 4.4). Type 9 is defined as a complicated form of pressure events instead of a type of perturbation because it features relatively pronounced type 2-4 events and terminates with pressure events of type 1. The timing and distribution of the identified pressure events are investigated in section 4.4. These include the onset of pressure events, and the timing of the minimum and the maximum in pressure. Their distribution is investigated in section 4.3.4 and compared with the results of the automatically identified events. This visual identification reveals the complexity of the pressure response, and the manual classification aids in the understanding of the usual process(es) causing pressure events.

4.3.2 Automatic Detection of Pressure Events

The automatic identification method is designed specifically for detecting pressure events that exhibit a drop followed by a rise over the course of a day (types 1-4 and the complex type 9, Fig. 4.1) and are characteristic of the glacier bed response (Lappegard et al., 2006). The method consists of determining minima and maxima as well as the pressure variance within a running window. The events are then filtered based upon a variance threshold and when there is a minimum and maximum associated. The developed method is applied to the whole measurement period and complements the manual extraction of pressure events.

Valleys and peaks are determined by computing the local minimum and maximum values in a 20-hour running window and accepting them as extrema only if the position of the minimum/maximum is at the centre point of the time window, such as:

$$F(t) = \begin{cases} 1 & \text{for } f(t) = \max\limits_{t' \in [t-\Delta t; t+\Delta t]} f(t') \\ 0 & \text{otherwise} \end{cases} \tag{4.1}$$

$F(t)$ is a binary output that contains the position of the extrema and $f(t)$ the pressure data at time t. $f(t')$ is the pressure data within the running window, which is centred at t and has a span of $t - \Delta t < t < t + \Delta t$, with $\Delta t = 10$ hours. The concept of the method is based on the robustness of the position of a minimum or maximum value in an overlapping running window, but doesn't allow for multiple pressure events within the time window. If an extremum is pronounced, the running window detects it as a minimum/maximum point and its position within the time window moves as the overlapping window is shifted. The minimum/maximum is then detected when its position is at the centre of the window or 10 hours from the start of the window, meaning that the extremum is robust. This condition will not be fulfilled when there is low variance in pressure or strong noise because the extremum will vary in position as the window moves and is less likely to be detected at the centre of the running window. The length of the time window is $2\Delta t$ or 20 hours to ensure that daily pressure events do not overlap.

This technique identifies many extrema that are filtered assuming that a trough is followed by a peak, as seen in events of types 1-4 (section 4.3.1) and that there is a high degree of variance between them. For LC4 and LC6, the filter retains minima and maxima that have a variance greater than 4×10^{-6} MPa for the period of seven hours following the valley and preceding the peak, respectively. The time window of the filter corresponds approximately to the typical time between a valley and a peak (section 4.3.4). Finally, a pair filter keeps pressure events where a trough and peak are observed within a running window of 30 hours, longer than the span of daily pressure events, and thus rejects single extrema as well as pressure disturbances of types 5-8 (Fig. 4.1).

The automatic method for the detection of pressure events of types 1-4 and 9 is applied to the load cell data, which has been resampled to a one-hour interval in order to reduce background noise. The algorithm identifies 1282 and 935 pressure events in LC4 and LC6 pressure data, respectively. The results of the automatic methods for LC4 and LC6 are compared for a two-month period in 1998 as shown in figure 4.2, along with the results of the manual technique applied to LC6 (section 4.3.1). The method performs less well in winter due to a higher signal-to-noise ratio (Appendix C, Fig. C.1). The variance threshold is also better suited to LC6 than LC4 as it is less exposed and has a stronger response to changes at the glacier bed, leading to a greater number of detections.

A comparison of the total number of pressure events extracted manually and automatically shows relatively good agreement for the eight-year period studied. There is a 53% success rate if all events identified in the manual method are included, and the success rate increases to 74% and 92% for events defined as types 1-4 and with a pressure intensity

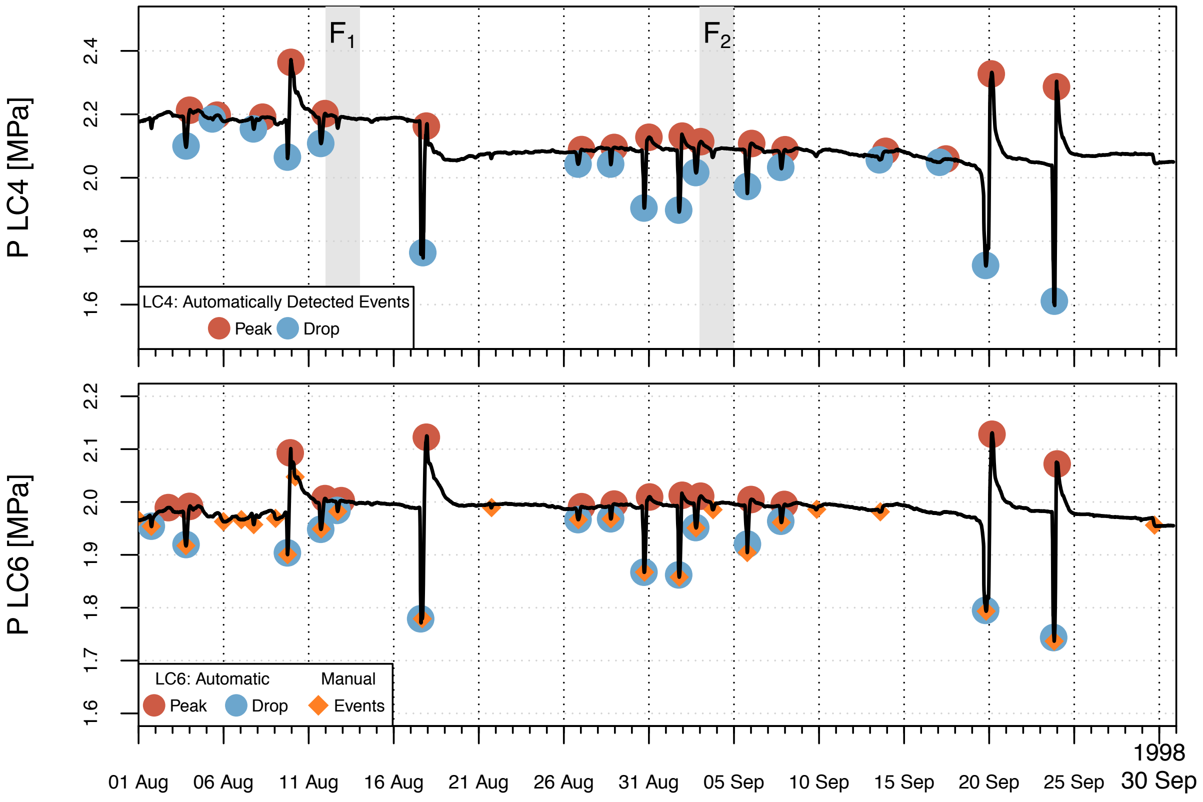

Figure 4.2: Pressure events identified using the automatic detection method for LC4 (top) and LC6 (bottom) for a two-month period in 1998. The manual method was applied to LC6 only (diamond). The automatic method discards the smallest events and events with uncertain peak (F_1 and F_2).

higher than 0.01 and 0.1 MPa (total number of events is 330 and 112 events, respectively). This difference is because the manual identification of events includes pressure perturbations of types 5-8 and obtains a greater number of events of low-intensity (Fig. 4.2 and C.1). The perturbations are filtered in the automatic method because these events have a variance lower than the threshold value of 4×10^{-6} MPa. The automatic method fails to detect some characteristic pressure events such as that on 13 August and 3 September at LC4, shown in figure 4.2 (F_1 and F_2), due to the lack of a clear maximum in the pressure records. High frequency noise also affects the identification of events. For example, the technique does not detect an event on 8 December 1998 in LC4 data (Fig. C.1, F_3).

The specifications of the automatic method lead to an underestimate of the number of pressure events in summer and an overestimate in winter due to an increase in signal-to-noise ratio. The identified pressure events are statistically analysed and summarised in figures 4.3, 4.4, and 4.5.

4.3.3 Seasonal Distribution of Intensity and Duration of Pressure Events

The melt season and associated production of meltwater leads to significant changes in the glacier hydrological system, which perturbs the pressure at the glacier base and especially the parts that are hydrologically isolated from the connected drainage system (Lappegard et al., 2006). The occurrence, intensity and duration of pressure events, identified in section 4.3.2, are investigated on a seasonal scale in order to derive the temporal distribution of the pressure event characteristics and understand what governs the variability in pressure events (Fig. 4.3).

The number of pressure events increases in summer as the glacier bed responds to surface melt and the development of the subglacial hydrological drainage. Figure 4.3a shows the seasonal variation in the number of pressure events, normalised for each month by the total number of months with pressure data. This graph thus shows the number of events that will be triggered during a typical year for LC4 and LC6. As pressure events usually have a duration of one day (Lappegard et al., 2006), the monthly distribution graph shows that the glacier bed is disturbed 1-3 days per month between November and March and 8-12 days per month between May and September (Fig. 4.3a). The isolated drainage system responds less than the connected hydrological system as measured in boreholes. Indeed, water pressure in boreholes shows diurnal variations in summer (Gordon et al., 1998; Harper et al., 2005; Meierbachtol et al., 2013; Andrews et al., 2014).

The monthly distribution in intensity of pressure events, meaning the difference in pressure between minimum and maximum values (Fig. 4.3b), further indicates that the smallest and most common events (<0.1 MPa, Fig. 4.3c) occur mainly in summer (average of 162 events per month) and rarely in winter. In Spring (April-May) and Autumn (September-November), the number of high intensity pressure event increases, although there are fewer events than in summer. This difference may reflect a stronger response of the glacier bed as large volumes of meltwater are rapidly funnelled into a drainage system of low capacity. This situation is commonly observed at the beginning of the melt season and during autumn rainfall events. In contrast, in summer a more developed drainage system can accommodate the daily production of meltwater so the subglacial system is less disturbed.

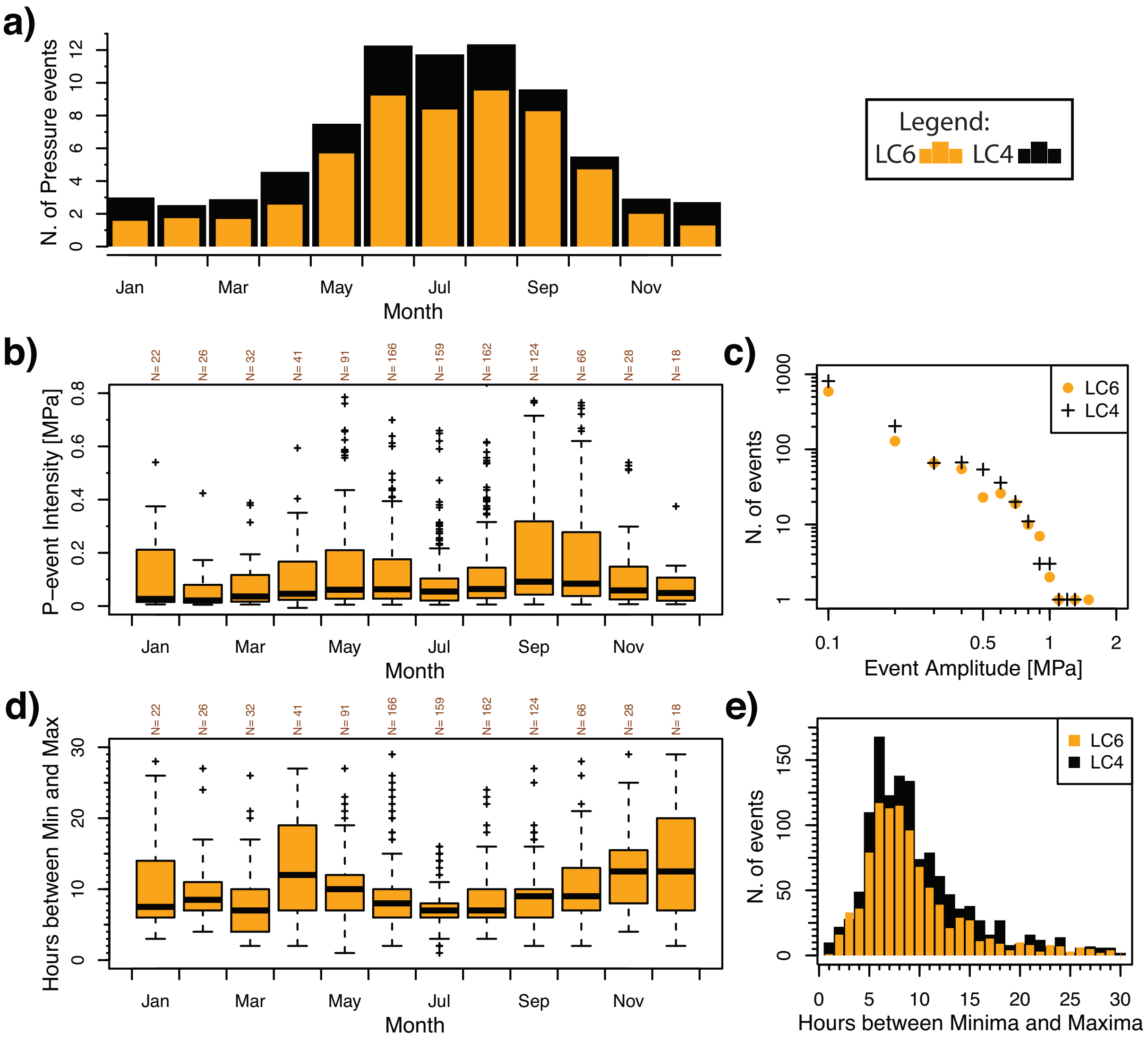

Figure 4.3: a) Average monthly occurrence of pressure events for LC6 (orange) and LC4 (black). b) Monthly distribution of the intensity of pressure events at LC6 with N the number of points per month given at the top of the graph. c) Logarithmic distribution of the intensity of pressure events obtained from the difference between minimum and maximum. d) Monthly distribution (for LC6 only) and e) distribution of the time interval between minimum and maximum of pressure events. All results are based on automatically-detected events for the measurement period 1993-2014.

The large distribution in pressure intensity in April is associated with an increase in the duration of pressure events, defined as the time difference between minimum and maximum in pressure (Fig. 4.3d). Longer pressure events are assumed to reflect a stronger subglacial forcing, which also cause an increase in time needed for the system to recover. The seasonal variability in the duration of an event is higher in winter, ranging from 3 hours to more than 25 hours, and lower in summer, ranging from 3 to 15 hours (Fig. 4.3d and 4.3e). The difference is again explained by an increase in the efficiency of the subglacial hydrological drainage system in summer. A developed drainage system accommodates an increase in meltwater faster, limiting the level of pressurisation in channels and disturbance in the isolated drainage system. The glacier bed response is dampened and recovers faster in summer.

The seasonal distribution in intensity and duration of pressure events reflects the influence of the melt season. Pressure events characterise winter and summer regimes as emphasised by Lappegard et al. (2006). Here, the winter regime is defined by few and long events although the duration between the maxima and minima in pressure varies. The summer regime is instead characterised by many low intensity events with a short time interval between the two extrema of pressure events. Spring and autumn are similar to the winter regime, but the intensity and duration of pressure events are more variable. During these two seasons, the capacity of the drainage system cannot accommodate rapid surface melt causing strong changes at the glacier bed. In autumn, the large variability in intensity is due to heavy rainfall events, diminishing melt activity, and a slowly contracting drainage system that leads to a large variability in the capacity of the subglacial hydrological system. Nevertheless, there is still a short response time due to the greater efficiency of the drainage system compared with spring and winter. This efficiency intensifies recovery to the background level in pressure by rapidly evacuating the water, whereas in spring the recovery time is much longer as the drainage system is not yet developed. The capacity and efficiency may not directly cause pressure events; however they influence the intensity and timing of the response of the glacier bed.

4.3.4 Timing and Shape of Daily Pressure Events

The timing and the shape of pressure events are investigated on a daily scale in order to identify the processes that trigger these events. The timing of the minimum and maximum in pressure is examined and a principal component analysis identifies the typical shape of pressure events and associated discharge curve.

Pressure events defined as type 1-4 are recurrent features of the load cell record and preferentially occur at a certain time of the day (Fig. 4.4). The temporal variation of the start, minimum and maximum of the pressure events is first determined from the manually identified events in LC6 records for eight years (section 4.3.1). This record consists of 440 events selected if the intensity is greater than 0.01 MPa (total number: 523). The population is thus representative of the most significant pressure events. The automatically extracted pressure events in LC4 and LC6 records cover the entire measurement period and give a total of 935 and 1282 events, respectively.

The start of the pressure event is determined visually as an increase in pressure gradient (Lappegard et al., 2006) and the temporal distribution indicates a typical onset between 13:00 and 16:00 as shown in figure 4.4b. A minimum follows the decrease in pressure and preferentially occurs between 18:00 and 19:00 for the manually extracted events and 16:00 and 19:00 for the automatically detected events (Fig. 4.4b and 4.4d). The timing of the maxima is statistically more spread and is observed from 21:00 and as late as 5:00-7:00, the following day (Fig. 4.4c and 4.4e). The overall pattern reflects the influence of meltwater production that usually increases during the day, peaks in late afternoon and decreases in the evening. Nevertheless, other processes linked to surface melt can modify the normal stress at the glacier bed on a diurnal basis such as: pressurisation of the drainage system, fluctuation in sliding, opening/closure of cavities or stress redistribution when the glacier bed is not entirely in contact with bedrock.

The shape of pressure events is extracted using a Principal Component Analysis (PCA) and is investigated to understand the cause of pressure events. This method reveals the general shape of pressure events by extracting the largest variances in a covariance matrix of daily pressure events, and decomposes the signal in principal components using eigenvectors. These eigenvectors create new orthogonal coordinates for the temporal variation in pressure during the day that are rotated to fit the largest possible variance, assuming that the variance is uncorrelated. The principal component analysis reduces the complexity of the shape of daily pressure events by ignoring random noise and outliers and keeping only the characteristic daily variations in pressure. This method is applied to a stack of 1282 and 935 events measured at LC4 and LC6, respectively. The time of the minimum is defined as a reference in order to normalise the start of the stack of pressure events. The analysis uses the pressure data with a 15 minute interval. The PCA is computed for a period that covers 6 hours before and 18 hours after the minimum. This length is reduced to a day in order to avoid overlap between succeeding events. Figure 4.5 and figure C.3 in Appendix C show the envelope in variance of pressure over a day and the percentage

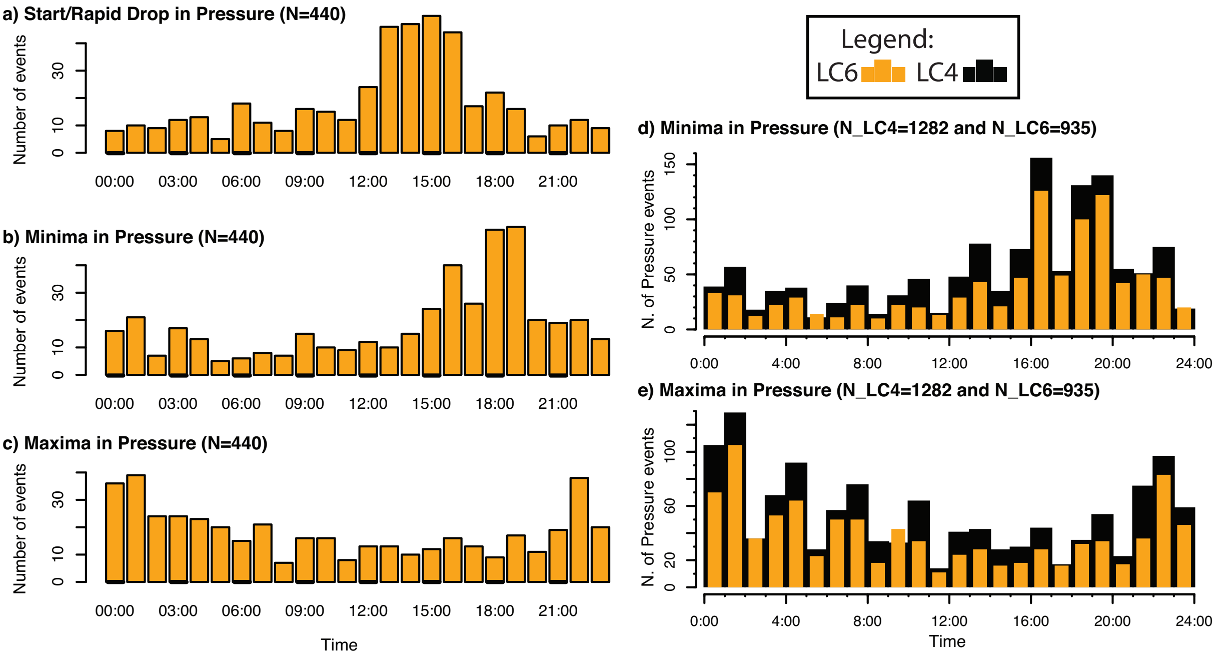

Figure 4.4: a) Timing of the start (a), minima (b,d) and maxima (c,e) of identified pressure events on a daily time scale. The hourly distribution of their occurrence is calculated from pressure events detected manually for LC6 (a,b,c) and automatically for LC6 and LC4 (d,e).

of cumulative variance explained by the first three principal components, which is equal to 66/61, 80/77 and 90/87% for LC6/LC4, respectively.

The resulting shape of pressure events is identical for both load cells. It demonstrates that pressure decreases from a background level at a faster rate after 16:00, reaches a minimum then rises smoothly, reaches a peak in pressure and finally returns to approximately the original pressure. The distinct minimum is a consequence of selecting the trough as the time of reference. The disappearance of the peak in pressure is probably due to the variability in timing, which is not captured in figure 4.5. The peak as shown in section 4.3.1 may thus be a less systematic feature. The most represented variance is a combination of types 2-4 as defined in figure 4.1 and shows a pressure range of nearly 100 kPa for LC6 and 120 kPa for LC4 (Fig. 4.5 and C.3). The low-intensity events dominate the output as they comprise 64 % of the total events (Fig. 4.3c). The lack of peaks in many pressure events suggests that diurnal production of meltwater is not directly linked to the increase and maxima in pressure as measured by LC6 and LC4. One possibility is that the peak is caused by stress redistribution at the interface between ice and bedrock. Stress bridging, a type of stress redistribution, transfers the load of unsupported ice within subglacial cavities or channels to their edge, which causes normal stress to increase at the contact of the ice with the bed (Chapter 6). The exponential decay in pressure after the peak also indicates a stress relaxation due to the viscous flow of the ice (Fig. 4.2) as it resumes contact with the bedrock. This process also explains the vanishing of the peak for low intensity pressure events because the more modest the event, the smaller the decoupling between ice and bedrock and stress bridging effect.

4.3.5 Daily Pressure Events and Discharge

The relationship between pressure events and hydrology has been identified earlier: 1) the triggering is often associated with the maximum value in discharge gradient supporting the occurrence of pressurisation at the glacier bed (Lappegard et al., 2006) and 2) the minima is reached when the capacity of the drainage system can accommodate and overcome the input volume of surface melt.

A principal component analysis is used to compare the typical pressure events, described above, with the daily variation in subglacial discharge (station 3 in Fig. 3.1). Discharge responds to both production of meltwater and changes in capacity of the hydrological drainage system. Variations in discharge are assumed to be representative of the changes in water pressure and subglacial conditions near the load cell network because of the proximity of the load cells to the subglacial intakes (110-420 m from the load cells). The same principal component analysis that was performed for the load cell data is also applied to discharge data for days that coincide with pressure events. 311 days with discharge that overlap with time of pressure events are extracted. They represent 38% of the total number of days with pressure events occurring between 1998 and 2013 (total: 807). The low number of extracted days is due to missing values in the discharge data and problems with the rating curve for high discharge (section 3.2.3). This number, although low, is still representative of the occurrence of pressure events as the monthly distribution of the studied pressure events shows the same Gaussian distribution as in figure 4.3a.

The results of the first three principal components for the daily variations in discharge explain 53, 72 and 84% of the cumulative variance, respectively (Fig. 4.6). The main feature is that discharge increases during a typical pressure event as a result of an increase in surface melt. This observation is consistent with the triggering process of pressure events associated with a pressurisation of the subglacial drainage system. Diurnal variations in discharge caused by surface melt are also superimposed onto this increase. This fluctuation was expected to be a more significant feature as it could explain the diurnal behaviour of pressure events (Fig. 4.5). Thus, pressure events are primarily caused by

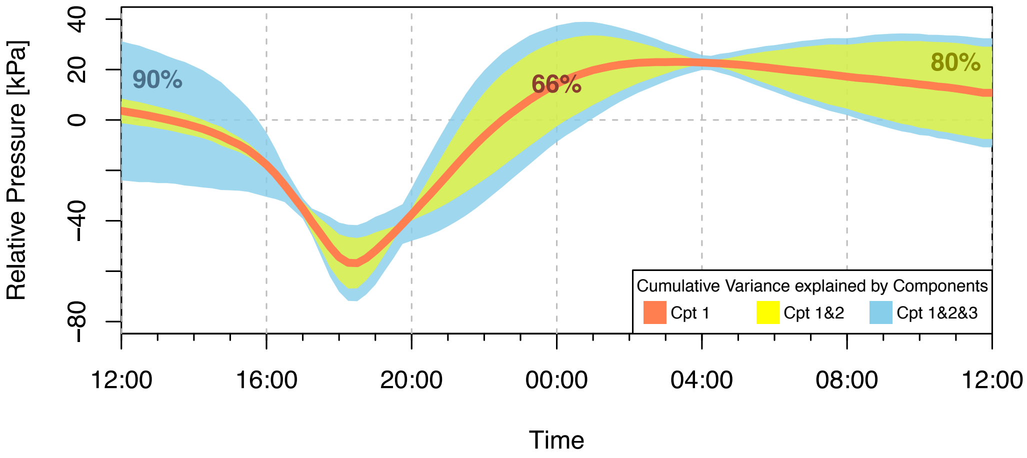

Figure 4.5: Envelope of variance and cumulative percentage explained by the first three components of the principal component analysis based on 795 daily pressure events identified automatically in LC6 records between 1993 and 2014. The studied time window for the pressure events is defined by the time of the minimum that starts 6 hours earlier, ends 12 hours later and is set in the graph to 17:30 to fit the timing as found in figure4.4d.

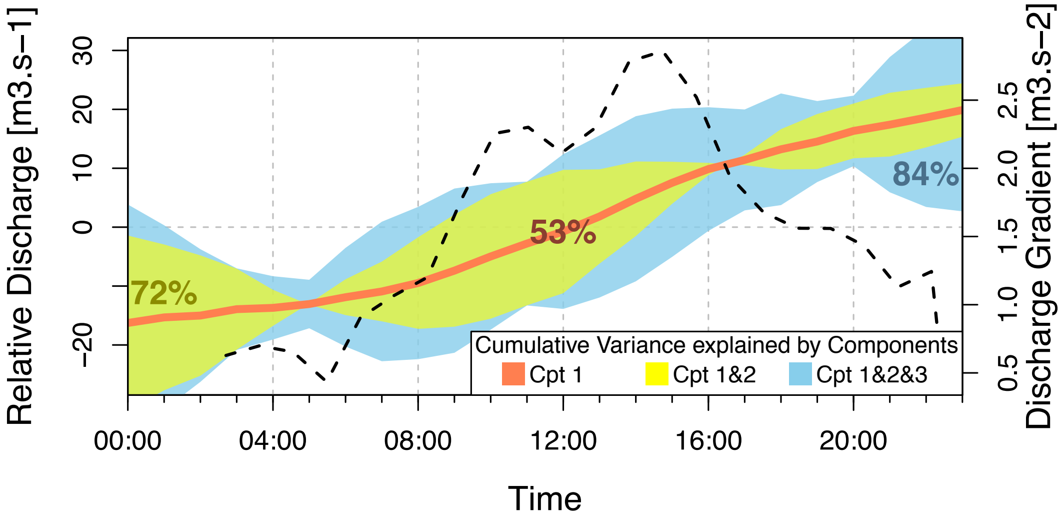

Figure 4.6: Variance in discharge computed from a principal component analysis for 278 days concurrent with pressure events between 1993 and 2014. The gradient in discharge of the first component (dashed line) is also plotted and reaches a maximum between 13:00 and 16:00.

an increase in meltwater input that causes pressurisation at the glacier bed. A secondary cause is then related to the diurnal variation in production of meltwater and discharge as highlighted by the gradient in discharge of the first component (Fig. 4.6). The gradient exhibits a diurnal response with a low before 7:00 that gradually rises and reaches a maximum between 14:00 and 16:00. The maximum in gradient occurs around the same time as the start of pressure events (13:00-16:00 in Fig. 4.4) and the start of the drop in pressure obtained from the principal component analysis of pressure events (15:00-16:00 in Fig. 4.5). The time of the maximum gradient is assumed to represent the time at which the subglacial hydrological system undergoes over-pressurisation (Lappegard et al., 2006). The pressurisation leads to a flooding of the glacier base and enhances hydrological connections at the glacier bed. Increase in water pressure in the efficient drainage system also causes channels to support some of the ice load, thus reducing pressure on the bedrock (Lefeuvre et al., 2015, Paper II).

The trigger of pressure events is thus identified. Pressurisation of the efficient hydrological drainage system leads to a contrasting decrease in pressure in the isolated subglacial drainage system. The minimum in pressure is assumed to be reached when the capacity of the drainage system becomes so large that it accommodates surface meltwater and decreases water pressure in channels. Falling water pressure leads to a rise in pressure in isolated parts of the bed due to the stress bridging effect (Chapter 6). Pressure at the ice-bedrock contact then rises above the overburden pressure and the larger the channels (or capacity of the drainage system) the more pronounced the peak in pressure at the glacier bed. This effect may vary with or depend on the intensity of earlier pressurisation, flooding of the glacier bed and opening of cavities. For the largest events, pressure measured by the load cells decays exponentially from the peak in pressure, which is caused by a relaxation of stresses through viscous ice flow during the reconnection between the glacier bed and bedrock. Therefore, the nature and behaviour of pressure events offers some insight into the timing of pressurisation in the efficient hydrological system at the glacier bed as well as the extent of the area of the glacier bed that is not resting on bedrock after the development of the drainage system.

4.3.6 Conclusions

The characteristics of daily pressure events, such as seasonal variation, intensity, timing and shape, highlight the role of meltwater in the pressure response of the unconnected drainage system.

The seasonal subglacial activity, as measured by the number of pressure events, increases during the melt season. Nevertheless, the intensity of pressure events decreases in summer, showing a dampening of the glacier bed response. The largest pressure perturbations occur in spring and autumn, when the drainage system is not yet developed or is contracting (i.e. low capacity) and melt and rainfall events lead to a high input rate of meltwater. The duration between the minima and maxima of pressure events also demonstrates that pressure events last longer in spring, whereas the pressure events are short in summer and autumn. This difference is explained by a better efficiency of the subglacial drainage system at evacuating meltwater. In spring, the efficiency is low as channels are not yet formed, whereas in summer and autumn, channels are developed and accommodate surface melt faster.

The response of the unconnected drainage system in summer shows that daily pressure events are associated with diurnal melt at the glacier surface. The timing and principal components of pressure events indicate that pressurisation of the efficient hydrological system, identified from the steepest gradient in discharge, triggers pressure events. The observed drop in pressure is due either to load transfer where channels take up the load from the surrounding bed or to an increase in basal sliding that decreases the shear stress applied on the load cell plate. A typical pressure event starts with a drop in pressure around 13:00-16:00, reaches a minimum around 18:00-19:00 and a maximum after midnight. The intensity of the response is usually <0.12 MPa although 1 MPa pressure events are also observed. The peak in pressure is not a consistent feature. The peak depends on the intensity of the preceding drop and may reflect stress bridging effects at the glacier bed during contraction of the drainage system. After the peak, the exponential decay in pressure is caused by ice flow as the ice regains contact with the bed, thus decreasing stress concentration on a small part of the bedrock surface.

We conclude that hydrological pressurisation in the efficient drainage system triggers pressure events. The following drop in pressure is produced by either load transfer near channels or increased basal sliding. The peak and then decay in pressure are controlled by stress concentration and mechanical flow of the ice at the glacier bed. Stronger pressurisation in the drainage system in spring and autumn also increases the length and intensity of pressure events.

4.4 Spring Melt Events

Spring melt events are examined in order to understand the response of the unconnected drainage system during the development of an efficient subglacial hydrological system. During these melt events, the glacier is known to experience bed separation and opening of cavities as meltwater is routed to the glacier base (Harper et al., 2007). The pressure response in the unconnected drainage system is investigated in relation to these subglacial processes.

Pressure in the unconnected system shows pressure events of high intensity as surface melt increases in spring (section 4.3.3). From the two decades of load cell data, two end-members of the pressure response during spring melt events are identified (Table D.1). The glacier bed response exhibits either a simple pressure event of type 1 (Fig. 4.1) or a complex response with a succession of events of types 9 and types 5-7 (section 4.3.1). The spring melt events show some variability between these two end-members that reflects the complexity of the reorganisation of the subglacial system. As the drainage system adjusts to persistent surface melt, the typical summer regime develops and diurnal pressure events dominate the pressure signal (section 4.3.3).

4.4.1 Simple Glacier Bed Response: Spring 2010

The glacier bed response in spring 2010 consists of a rapid, short and intense pressure event that occurs during one of the sharpest and strongest melt events observed in the discharge records (Fig. 4.7).

The start of the spring melt event on 14 May 2010 is striking. In April and May before the event, surface melt is limited to the lowermost part of the glacier (<800 m a.s.l.). Air temperature, recorded on a nunatak at Skjæret (1364 m a.s.l.), remains negative and stable with a mean of -6 °C. From 12 May, air temperature rises by 16 °C in four days. It becomes positive at Skjæret on 14 May, causing extensive melt on the glacier surface. On the same day, subglacial discharge measured under Engabreen (around 600 m a.s.l.) shows a slight increase of 0.2 m^3 s^{-1} as meltwater reaches the glacier bed. However, the most significant rise in discharge occurs one day later and reaches a maximum discharge of 6 m^3 s^{-1} on 17 May. The initial arrival of meltwater affects the pressure at the glacier base and all load cells measure a slight drop in pressure early in the morning of 14 May (Fig. 4.7). Larger variations in pressure at load cells LC97_1 and LC97_2 start in the afternoon, concurrently with the maximum air temperature ($\sim$6°C). This infiltration of meltwater probably does not trigger an acceleration of the glacier by basal sliding because the response of the load cells is small and this melt event does not produce enough meltwater to substantially increase the subglacial water pressure. These first irregular variations in pressure are a consequence of hydrological changes through reorganisation and pressurisation of the distributed hydrological system. The routing of meltwater at the glacier base locally increases water pressure that supports some of the glacier load and thus reduces the pressure applied to the surrounding bedrock and the load cell plate. As water drains from parts of the distributed system, water pressure decreases and stress bridging near low pressure cavities causes an increase in normal stress at the glacier bed (Paper II). This process and the resulting pressure signal occurs over a few hours only, when there is little melt production and low capacity of the drainage system. Similar pressure oscillations were observed at South Glacier, in Yukon Territory, Canada (Schoof et al., 2014). They are produced by instabilities in a subglacial linked cavity system where low meltwater production and water storage favours oscillating routing and drainage of water at the glacier base. This hydrological interpretation explains low and short pressure changes during the early injection of meltwater, when there is assumed to be little basal sliding.

On 15 May, air temperature remains high, discharge rate increases and the load cells' response is synchronous and of high intensity (Fig. 4.7). The pressure records at LC97_1 and LC97_2 show a decrease on 15 May (00:00), that accelerates around 04:00 in the morning and is followed, 3 hours later, by a drop in pressure at all load cells. The magnitude of the drop is of 0.3, 0.4, 0.5 and 0.6 MPa at load cells LC4, LC6, LC97_1 and LC97_2, respectively. The cause of this decrease must be rapid pressurisation of the drainage system or decoupling at the glacier base in order to explain the synchroneity of the response. The timing of the following minimum in pressure is unclear because of noise in the data that increases during strong subglacial changes. Although noisy, the time of the minimum appears to vary across the load cell network (Fig. 4.7). This difference in response time is also observed later during the rise in pressure and stops after the peak in pressure. The peak occurs before midnight at LC4 and LC6 and is followed by an exponential decay in pressure. The decrease is more gentle at LC97_1 and LC97_2 and is delayed by 3 hours relative to the other load cells. This lag may be due to the location of the load cells. LC97_1 and LC97_2 are located in an area more exposed to the hydrological drainage system (Lappegard et al., 2006; Lefeuvre et al., 2015) that takes longer to close.

Pressure slowly returns to the background level at the end of the main spring pressure event. Nevertheless, the pressure records show some slight variations before stabilising on

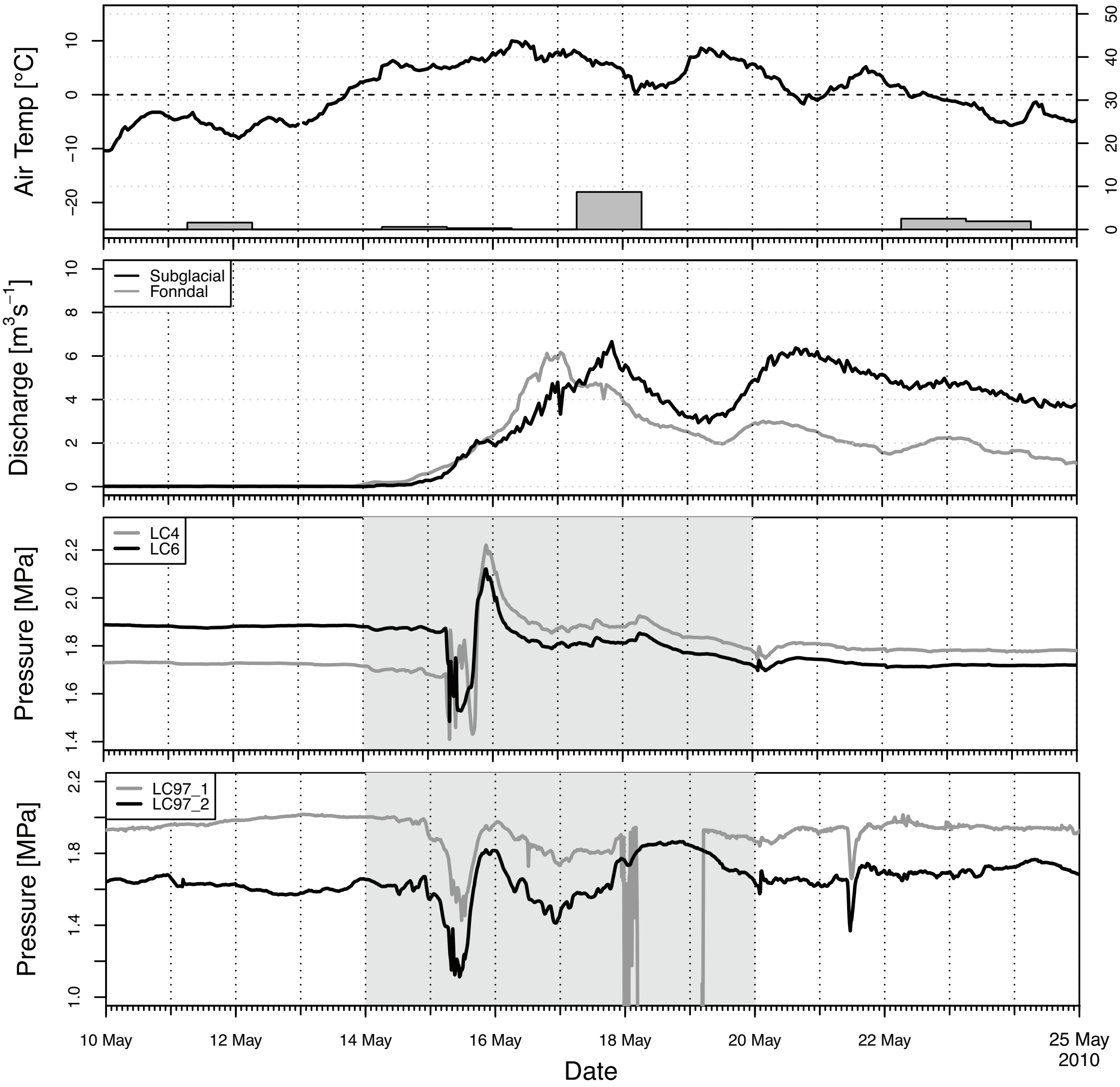

Figure 4.7: Spring Melt event in 2010 with air temperature from Skjæret station, precipitation from Reipå station, discharge data and load cell data.

20 May, especially in the unconnected system (LC4 and LC6). These irregular variations are similar to the ones observed at the beginning of the spring melt events and are typically events of type 5-7 (section 4.3.1). The hydrological system experiences similar conditions where the contraction of the drainage system causes a reorganisation of the distributed and unconnected drainage system.

Load cells LC97_1 and LC97_2 also record these small events, although they are superimposed onto a larger and longer variation in pressure between 16 and 20 May. This longer signal is characterised by a low pressure period on 16-17 May, high pressures on 18 May and a decrease to the background level in pressure. This variation in pressure reflects changes in pressurisation of the hydrological system and load transfer as indicated by its out-of-phase relationship with subglacial discharge (Paper II). Pressurisation occurs when the gradient in discharge is greatest and not when the discharge itself is greatest (Lappegard et al., 2006). This explains the lag between the extrema in pressure and discharge. Pressure measured at the load cells responds to these hydrological changes until 20 May. Then, the sustained melt and high discharge lead to the development of an efficient drainage system. Channelisation and high capacity of the drainage system reduce the possibility of pressurisation at the glacier bed and lead to a dampening of the response at the load cells.

The spring melt event in 2010 has a sharp onset in melt that causes a strong, short and homogeneous response in pressure at the glacier bed. The load cells show irregular variations in pressure that are signs of reorganisation of the hydrological system preceding the major event on 15 May. The continuous production of meltwater from 14 May reaches the glacier bed a day later and pressurises the subglacial system, causing decoupling at the glacier bed and the drop in pressure. Stress bridging and/or load transfer lead to the peak in pressure in the unconnected drainage system. As the drainage system closes, viscous relaxation (i.e. ice creep) causes the exponential decay in pressure. In the connected system, the load cells show an anti-correlated pressure response to subglacial discharge caused by pressurisation at the glacier bed until 20 May. The hydrological drainage system is then efficient enough to accommodate surface input and to reduce pressurisation and its effect on pressure at the glacier bed.

4.4.2 Complex Glacier Bed Response: Spring 2013

The start of the 2013 melt season is more gradual and associated with a complex response in pressure at the glacier bed (4.8). Spring 2010 and 2013 both have a pre-event stage with irregular fluctuations in pressure and a short, high-intensity pressure event terminating the spring melt event. However, the bed response differs in length and amplitude showing the importance of hydrological reorganisation of the drainage system during prolonged surface melting.

Prior to the main spring melt event in 2013 (11-19 May), there are two episodes when surface meltwater reaches the glacier bed. A combination of precipitation and surface melt triggers a rise in subglacial discharge on 15 April and on 6-7 May (App. D.6). The effect of meltwater routed to the glacier base does not trigger any major pressure events. However, it appears to precondition the bed by initiating the melting of subglacial channels and increasing subglacial water storage as little water is evacuated (discharge <0.1 m^3.s^{-1}). The subglacial drainage system is thus already developing before the spring melt event. From 9 May surface melt becomes almost continuous. Air temperature at Skjæret varies between -2 and 3 °C. The input of meltwater causes a rise in discharge on 11 May that is concurrent with the first notable variation in pressure at the glacier bed. The response in pressure is characterised by a double drop in pressure of $\sim$ 0.20 MPa, recorded at all load cells. There is also a delay between surface melt and bed response due to a slow meltwater transfer at the glacier surface (i.e. snowpack infiltration) or in the distributed drainage system. Thus, the subglacial system still shows characteristics of the winter regime (Lappegard et al., 2006).

A second perturbation at the glacier bed occurs as temperature at Skjæret (1364 m a.s.l.) remains positive between 12 and 14 May and melt continues (Fig. 4.9). On 12 May, pressure at LC4 and LC6 shows a double drop over less than 4 hours that is out-of-phase with high-intensity changes at LC97_1 and LC97_2, followed by a continuous increase in pressure at all load cells overnight. The double drop in pressure may be caused by water transfer in a linked cavity system as observed at South Glacier in Canada (Schoof et al., 2014). The subsequent increase in pressure indicates a stress bridging effect during a slow contraction of the efficient hydrological drainage system. The sustained melt leads to greater capacity of the subglacial drainage system and thus a faster drainage of meltwater stored at the glacier base. This reduction in storage is also consistent with the continuous increase in discharge during the entire spring melt event, that occurs even when air temperature falls below 1°C at Skjæret on 14-15 May. The lag between the drops in pressure and maximum air temperature indicates that the hydrological drainage system is still dominated by an inefficient distributed system.

Nevertheless, the inefficient distributed drainage system is active. Pressure measured at load cells LC97_1 and LC97_2 (45 cm apart) shows the effect of drainage of subglacial water on 13-14 May and 16-17 May. On these occasions, the load cells that previously had

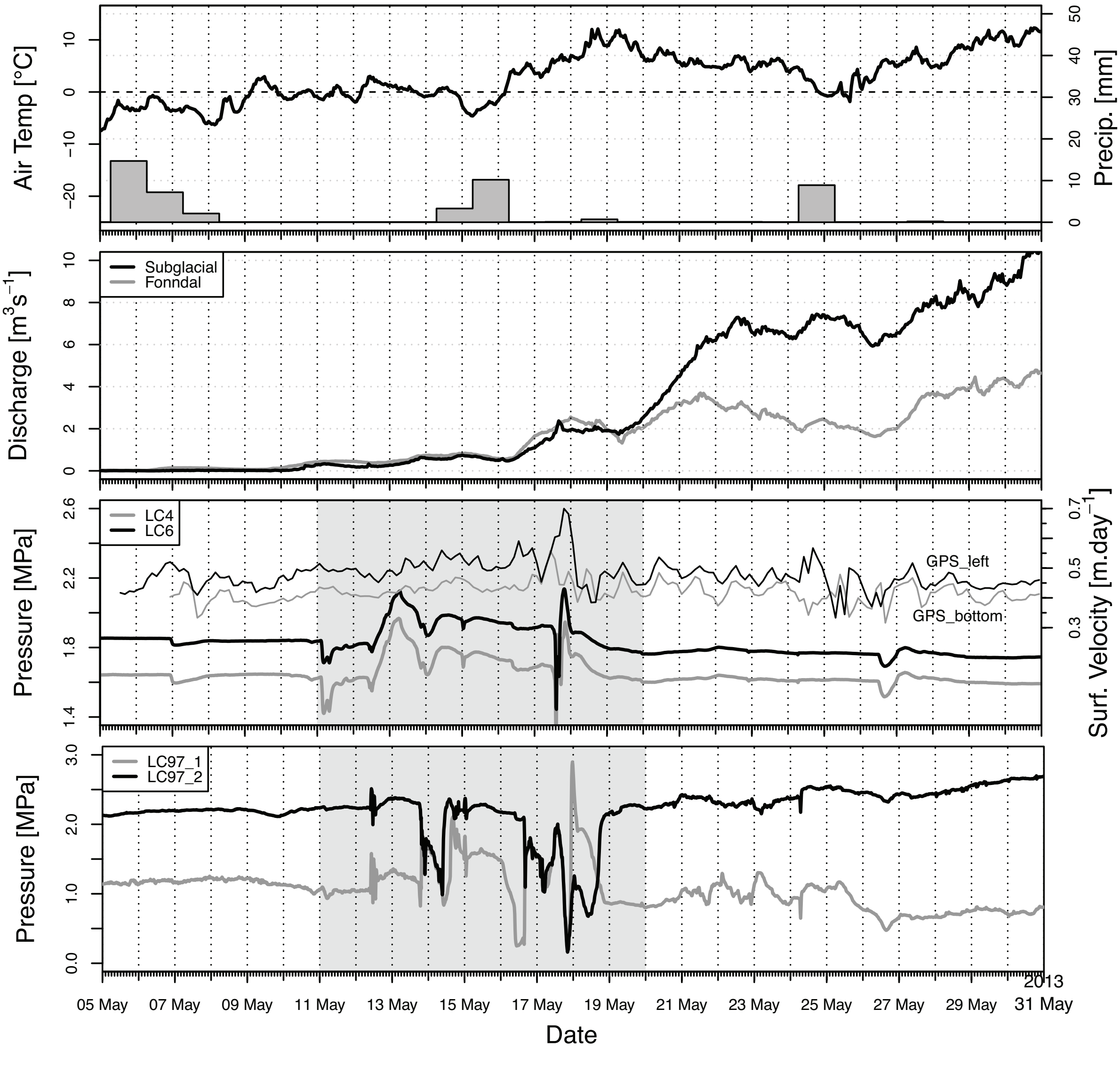

Figure 4.8: Spring melt event in 2013 with air temperature at Skjæret station (elevation 1364 m a.s.l.), precipitation at Reipå station, discharge data, surface velocity from two GPS receivers placed on the glacier tongue and pressure recorded at the load cells.

an offset of 1 MPa have the same pressure. They are thus connected through a common channel or cavity, and show local, hydrostatic water pressure. On 13-14 May this connection synchronously affects the pressure at LC4 and LC6. The pressure signal again shows a double drop, and an anti-correlated signal with the load cell pair LC97_1-LC97_2. Water pressure in the channel/cavity (i.e. LC97_1-LC97_2) decreases throughout the night and reflects the slight decrease in air temperature and discharge. The contraction of the drainage system is observed: 1) as ice regains contact first with the downstream load cell (LC97_2) and the upstream load cell a few hours later, and 2) as pressure at LC4 and LC6 also returns to the background level on 14 May.

The connection on 16-17 May is different, possibly because the drainage system is now more efficient, and it is associated with the initiation of the main spring pressure event (17-18 May). Pressure at LC97_2 decreases first on 16 May and is then followed by a drop in pressure measured by all load cells around 10:00 that is synchronous with a rapid rise in air temperature. Subsequently, load cells LC97_1 and LC97_2 become hydrologically connected and record a water pressure below the overburden pressure ($\sim$ 1.8 MPa). Water pressure decreases throughout the night until the hydrological system contracts and closes over LC97_2 between 05:00 and 11:00 on 17 May. Surface melt during the day then leads to an increase in water pressure and the pair LC97_1-LC97_2 reconnect. Water pressure measured at LC97_1 and LC97_2 reaches a maximum around 14:00 on 17 May, which is anti-correlated and synchronous with the main spring pressure event recorded at LC4 and LC6. The anti-correlation is also observed as water pressure falls at the pair LC97_1-LC97_2 in the evening when pressure at LC4 and LC6 peaks. These hydrological connections demonstrate that the load cells respond primarily to changes in the hydrological system. Nevertheless, the effect of basal sliding on pressure can be important. This relationship is examined using data from two GPS receivers installed on the glacier tongue and at an elevation 600 m lower than the glacier surface above the load cells (Fig. 4.9), (GPS data from Messerli, 2015). These data are part of Messerli (2015)'s thesis, which describes the dynamics of Engabreen. Despite the noise, the increase in surface velocity corresponds roughly with the timing of the main spring pressure event. The initiation of basal sliding above the SSL should occur later than at the snout if sliding propagates up glacier (Harper et al., 2007). However, the effect of basal sliding on pressure cannot be identified clearly due to the uncertainty in the velocity measurements (Messerli, 2015).

The contraction of the hydrological system during the spring melt event is identified from the peak in pressure and the associated decay in pressure. The peak occurs first at

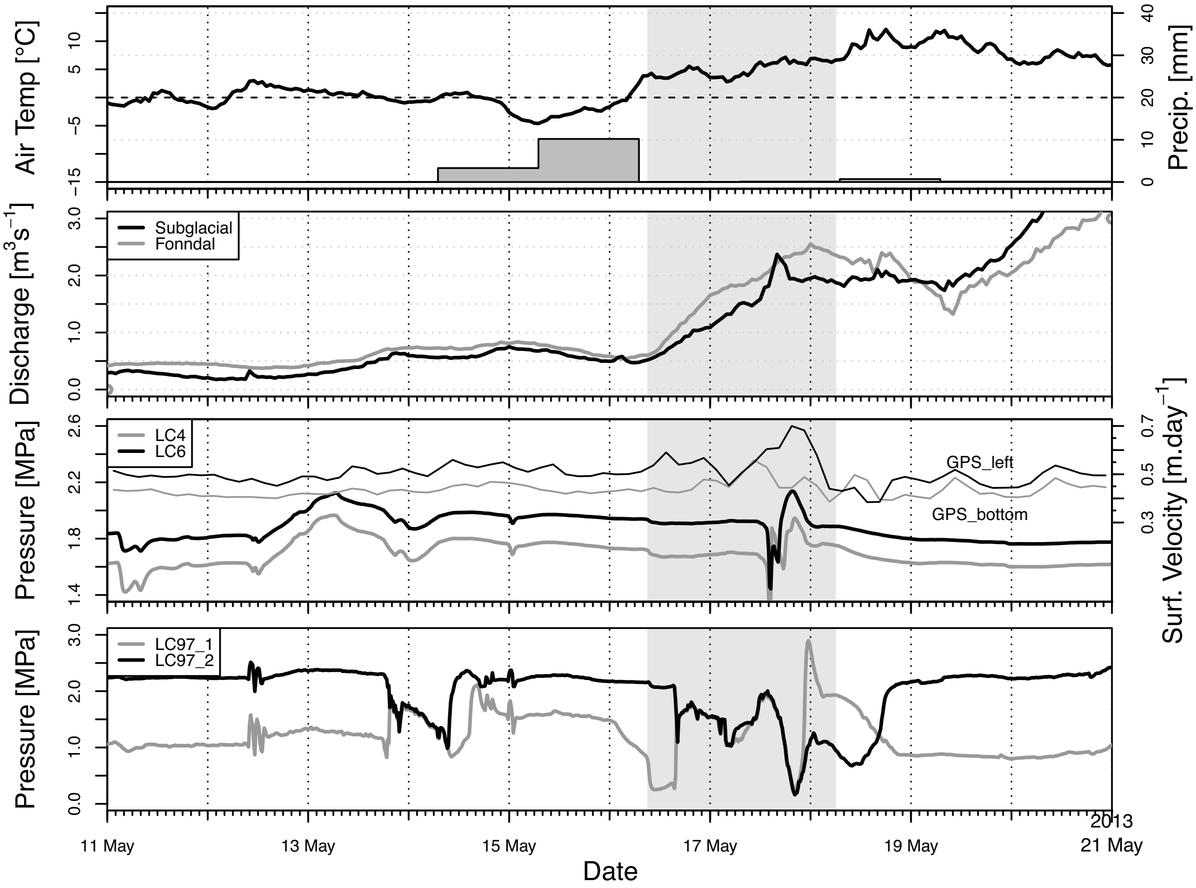

Figure 4.9: Close-up of the spring melt event in 2013 with air temperature at Skjæret station (elevation 1364 m a.s.l.), precipitation at Reipå station, discharge data, surface velocity from two GPS receivers placed on the glacier tongue and pressure recorded at the load cells.

the pair LC4-LC6 on 17 May and few hours later at the pair LC97_1-LC97_2. However, the closure is arrested at LC97_1 and LC97_2 due to a new influx of surface melt due to a rise in air temperature on 18 May. This forcing causes a reconnection with the hydrological system at the downstream load cell LC97_2 and a drop in pressure. After the main pressure event and peak in pressure, the subglacial system measured by the load cells becomes less responsive to surface melt as the pressure of the load cells returns to the level prior to the spring melt event and shows little fluctuation. The hydrological drainage system accommodates meltwater and reduces the possibility of pressurisation in subglacial channels that causes pressure events at the glacier bed.

In summary, the response at the glacier bed from the spring melt event in 2013 is slow and complex. In the early stage there is a delay between surface forcing and basal response, and although some meltwater reaches the bed, the subglacial drainage system is poorly developed. From the 13 May, a subglacial channel or cavity covers the load cells LC97_1 and LC97_2 and both measure water pressure. This hydrological connection indicates a reorganisation of the hydrological system with slow drainage capacity. A drop in temperature reduces surface melt input on 14-15 May, which leads to a contraction of the drainage system. The increase in melt on 16 May reopens the basal hydrological connection between LC97_1 and LC97_2. The peak in meltwater production and associated water pressure at the glacier bed leads to the triggering of a pressure event at LC4 and LC6. This pressurisation causes decoupling of the glacier bed that facilitates the drainage of channels or cavities that approximately coincides with the speed-up event as measured by the GPS receivers. As the water in the system is drained, the ice regains contact unevenly with the glacier bed, which concentrates stresses locally until the drainage system closes and pressure regains its background level.

4.4.3 Conclusions

This study demonstrates that pressure at the load cells can be used to identify different types of spring melt events. Increasing meltwater production in spring perturbs a subglacial drainage system dominated by an inefficient hydrological system. However, the pressure response shows that the development of the drainage system can vary in length and undergo complex changes in hydrological connectivity prior to the main spring pressure event. A short response is observed during a rapid and intense melt event in 2010. An increase in meltwater input causes pressurisation at the glacier bed and triggers a pressure event. The 2013 spring melt event is complex as meltwater routed to the glacier base flows irregularly and drains during the reorganisation of the inefficient drainage system. The pressure response becomes more homogeneous over the load cell network after the main pressure event. This pressure event is approximately concurrent with an increase in surface velocity and presumably basal sliding. A pressure event indicates 1) a pressurisation of the subglacial drainage system and 2) the establishment of an efficient drainage system during sustained melt events that reduces the sensitivity of the glacier bed to surface melt.

Chapter 5
Mapping the glacier bed

Melting

Paul Serail

5 Mapping the glacier bed

5.1 Introduction

The geometry of the glacier bed is fundamental in understanding the causes of pressure variations measured by the load cells. The bedrock shape controls water flow at the scale of the sensor network and stress redistribution from mechanical transfer and sliding. However, the knowledge of the bed topography near the Research Shaft is known only at a coarse spatial resolution of about one metre, and along subglacial tunnels melted at the glacier base (Fig. 3.3). The aim of this work is to find a suitable method for mapping the bedrock. It should improve the spatial coverage and resolution of the mapping originally conducted during the construction of the Svartisen Subglacial Laboratory in 1992-1993. A high precision mapping of the bedrock geometry is performed in order to 1) better characterise the load cell environment, 2) constrain the effect of bedrock in models of stress transfer and water flow at the glacier base and 3) provide a baseline for measuring erosion rates at the glacier base.

The conditions in man-made subglacial cavities and the remote location of the Svartisen Subglacial Laboratory impose restrictions on the methods available for mapping the glacier bed. The instruments used have to be easily transportable, water- and dirt-resistant, able to tolerate temperature contrasts, and have a fast rate of data collection. These requirements rule out the use of classic laser scanner or LIDAR. Thus, the mapping is performed based on two novel approaches: a short-range low-cost LiDAR (Light Detection And Ranging), the Kinect™, and 'Structure-from-Motion' (SfM), a photogrammetric technique. The two methods can be used individually but in our case have been used together in order to improve the final product. This chapter provides results of the bedrock mapping and a method framework for mapping subglacial environments.

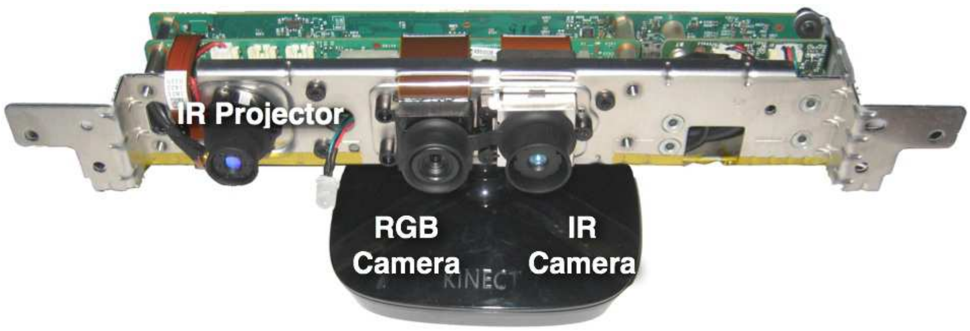

Figure 5.1: Interior of a Kinect with infrared projector at the left, colour camera in the centre and infrared camera to the right (reproduced from Mankoff et al. (2011)).

5.2 Techniques

5.2.1 Short-Range LiDAR: The Kinect™

The Kinect™ is a controller of the video game console Microsoft® Xbox®, and a ∼150€ casual laser scanner that can be used to map surfaces and 3D objects (Fig. 5.1). Its application in various research fields, most notably in the domain of computer vision and robotics (Han et al., 2013), has grown significantly since the public launch of the Kinect™ in 2010. It has also attracted interest in geosciences (Mankoff and Russo, 2012). The processing of real time data from the Kinect™ has led to a large variety of softwares and applications such as mapping large interior areas either manually (Henry et al., 2010; Izadi et al., 2011; Henry et al., 2012) or from remotely controlled vehicles (Bonnal, 2011; Bachrach et al., 2012), detecting objects (Lai et al., 2011) and controlling devices using human gestures (Doliotis et al., 2011; Wachs et al., 2011).

The development of processing techniques in computer vision facilitated the use of the Kinect™ in geoscience as described in Mankoff and Russo (2012). This pilot study demonstrated that the Kinect™ can measure temporal changes in surface elevation on a daily scale (e.g. debris-covered glacier surface), map bathymetry in shallow rivers and obtain geomorphological characteristics of sand ripples. The real-time collection of surface elevation is an advantage to investigate complex geometries and metre-scale processes. A study about the formation of penitentes showed that the Kinect™ resolved their 3D shape better than a commercial LiDAR and the structure from motion technique (Nicholson et al., 2014). The manoeuvrability of a hand-held Kinect enables to avoid obstacles that would block the field of view of fixed LiDAR. This aspect was shown to be particularly useful in speleological investigations of surface roughness of subglacial channels (Mankoff and

Gulley, 2012) and karst/stalagmite morphometry (Hammerle et al., 2014). The Kinect™ can also be mounted in laboratory experiments in order to monitor elevation changes. For example, Caviedes-Voullième et al. (2014) analyse fast grain flow over obstacles and compared snapshots of surface elevation measured at differences of hundreths of millisecond. These results help to validate grain flow models and understand the effect of geohazard protections in mountain areas on stopping avalanches. All these applications of the Kinect™ demonstrate the potential of this instrument in providing reliable data in order to understand processes in a wide range of environments.

The Kinect™ is composed of three built-in sensors: an RGB camera, an infrared projector and an infrared camera that continuously records colour image and depth at a rate of 30 frames per second (Fig. 5.1). The depth is overlaid with the RGB image after correcting for the difference in angle of view in order to produce a composite 3D model with colour value. The concept of the depth measurement is based on the deformation of a known infrared structured light pattern and is similar to interferometry. A pattern of randomly distributed points is emitted by the infrared projector at a wavelength of 830 nm. On the studied surface, the deformed projection is recorded by the infrared camera. The deformation is then internally computed into an intensity level, called Digital Number (DN) and converted into a depth image, the final product (Mankoff and Russo, 2012).

The advantages of the Kinect™ such as being inexpensive and replaceable outdoor field instrument (Mankoff and Gulley, 2012) make it a promising tool for the mapping of the bedrock at the Svartisen Subglacial Laboratory.

5.2.2 Structure from Motion

Structure from Motion (SfM) is a technique to determine the orientation and position of cameras from a set of overlapping images and is used to map 3D surfaces. In contrast with classic photogrammetry, SfM does not require the position of the cameras. This offers the advantage to use any pair of images even though their location and parameters are unknown. The positions and parameters of the cameras are instead computed from the images itself, and then the modelled cameras are used to reconstruct the 3D surface of an object based on classic photogrammetry methods. This flexibility and the fast rate of data collection were critical advantages in mapping bedrock inside the continuously contracting subglacial cavity.

The SfM technique was originally developed by Snavely et al. (2008). Their project aimed to reconstruct the 3D facade of popular historical monuments by using non-geolocalised images that are freely available on sharing platforms. However, the location, orientation and focal length of each cameras and so photos are unknown and have to be modelled. The first part of the SfM method consists in obtaining these parameters by extracting tie points on the images and modelling together all cameras to fit distances between tie points. A feature detection technique based on Scale-Invariant Feature Transform (SIFT, Lowe, 2004) produces tie points for each individual photos. The points are then matched between image pairs. The system of matching point serves to compute iteratively the position and the focal length of each camera until the sum of the distances between matches is minimised. That is, the iteration stops when the location of the tie points on the images and the projected points from the modelled cameras converges. This process is called the Bundle Adjustement (Snavely et al., 2008). The final step is to apply a dense feature matching from the new system of camera poses onto the original set of images. It is based on the Clustering Views for Multi-view Stereo (CMVS) and Patch-based Multi-view Stereo (PMVS2) written by Furukawa and Ponce (2010). It is important to note that these developments were only possible due to recent increase in computing power and the use of multi-threading and Graphic Processing Units (GPU) since SfM algorithms are computationally demanding. The final result is a point cloud in a relative coordinate system. The cloud can be scaled and geo-referenced based on three options: using ground control points, another geo-localised point cloud or the GPS position of the cameras.

The workflow (SIFT-SfM-CMVS-PMVS2) has now been integrated into many different user-friendly programs that require only a set of images as input. The images need to have good overlap, contrast and follow a structured track (e.g. flight path) to facilitate the image matching process (Westoby et al., 2012). In geology and glaciology, SfM opened a new scale of low cost mapping between terrestrial and airborne using pictures taken from Unmanned Aerial Vehicles (UAVs) (Niethammer et al., 2012; Ryan et al., 2015). Comparison of DEMs between SfM technique and traditional laser scanning shows that their spatial and horizontal resolution depend mostly on the density of points and laser penetration into vegetation (Niethammer et al., 2012; Westoby et al., 2012). The density varies with the orientation of the surface relative to the camera (e.g. shadowing) and surface properties (e.g. reflectance and transparency). The result of the SfM is also improved for larger camera sensors and lenses that have less distortion (Kääb et al., 2014).

The novelty and flexibility of the SfM technique was attractive and we thus tested its capacity to map the subglacial environment at the SSL.

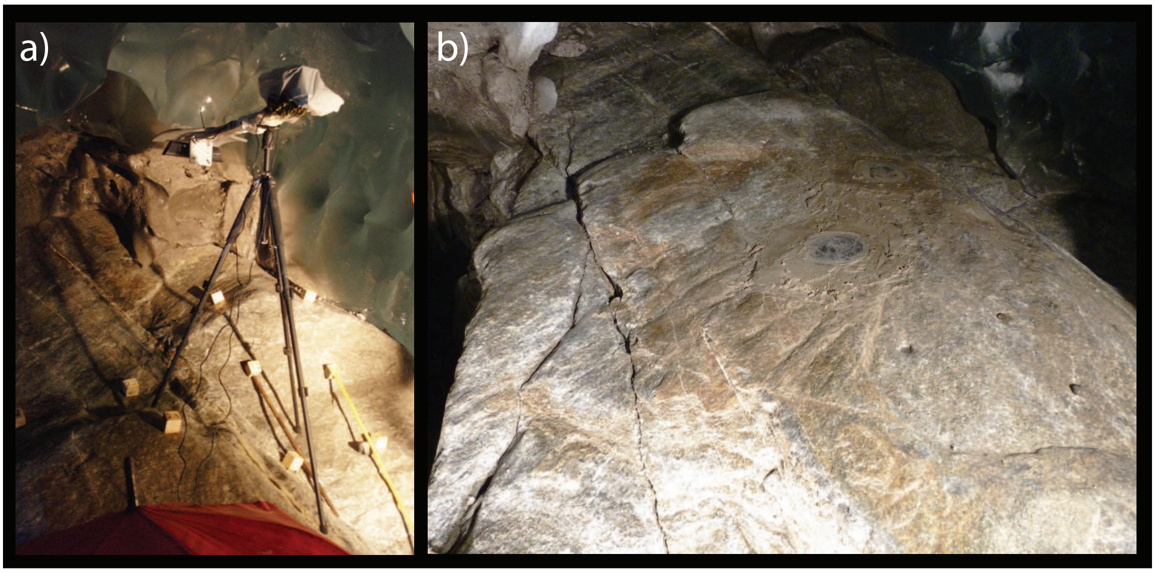

Figure 5.2: Photos of the Kinect and bedrock mapped in 2012. a) The Kinect is installed on a tripod and overlooks the bedrock and cubes that are used to reference the mapped surfaces. b) The photo shows the load cells LC97_1 and LC97_2 and the general structure of the bedrock downstream of the mapped area of photo a) and figure 5.7.

5.3 Methods

Three field campaigns were conducted to map the bedrock under the glacier near the location of load cells LC97_1 and LC1e (Fig. 5.4 and E.2). The Kinect was deployed in March 2012 and April 2012. The photos of the bedrock for the SfM technique were collected in April 2012 and April 2013. All surveys followed the same sequence described in figure 5.3.

The access to the glacier bed is melted out using a hot water drilling system from the horizontal research shaft (Fig. 3.4). The bedrock surface is cleared of ice and debris. The difficulty of melting obliges us to concentrate the melting effort to zones near the load cells the closest to the entrance: the load cells LC97_1 and LC1e. The concept is to map a small part of the bed at a time. Each time, the map is extended by merging the old and new mapped zones.

5.3.1 Kinect™

The Kinect™ is installed on a tripod and placed looking downward over different parts of the exposed bedrock inside the subglacial cavity (Fig. 5.2a). This technique (i.e. fixed position) is preferred for its higher precision and accuracy (e.g. averaged depth image)

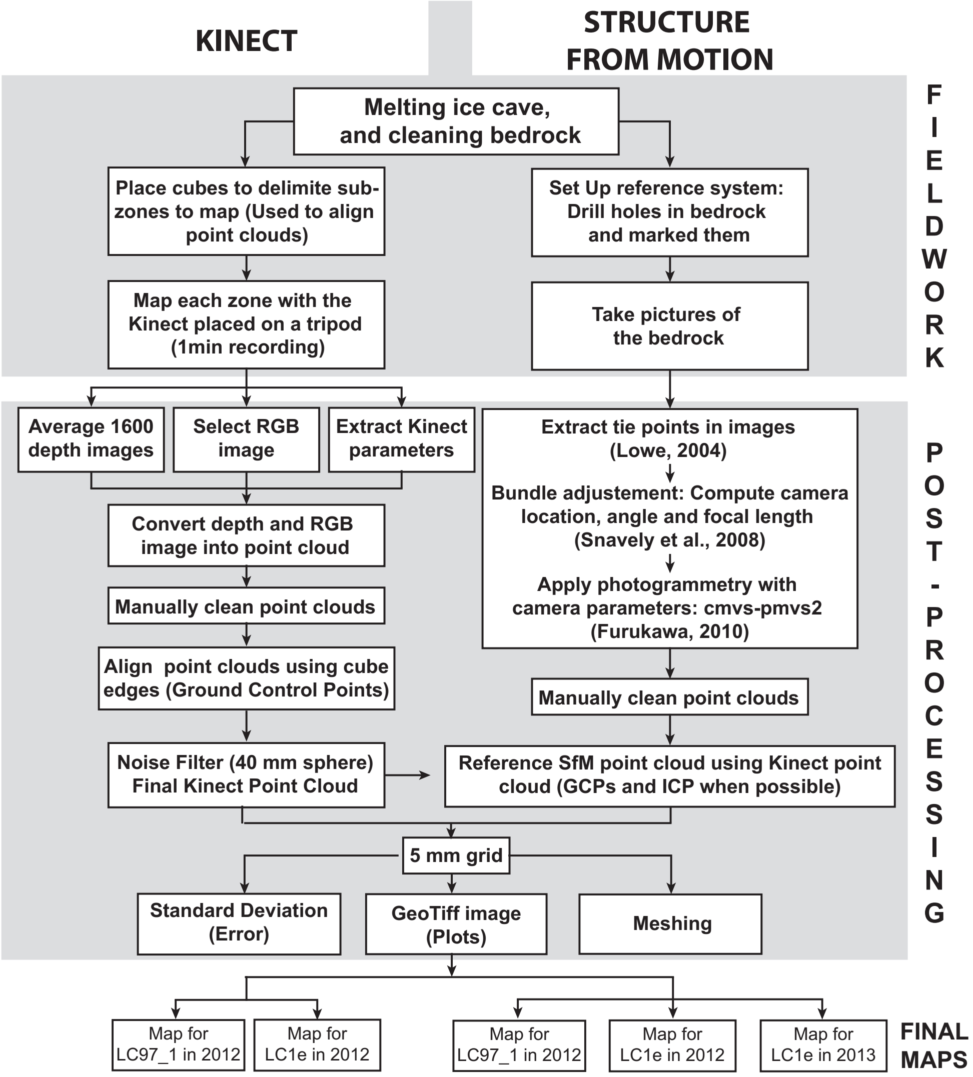
KINECT
STRUCTURE FROM MOTION
FIELDWORK
Melting ice cave, and cleaning bedrock
Place cubes to delimite sub-zones to map (Used to align point clouds)
Set Up reference system: Drill holes in bedrock and marked them
Map each zone with the Kinect placed on a tripod (1min recording)
Take pictures of the bedrock
POST-PROCESSING
Average 1600 depth images
Select RGB image
Extract Kinect parameters
Extract tie points in images (Lowe, 2004)
Bundle adjustement: Compute camera location, angle and focal length (Snavely et al., 2008)
Apply photogrammetry with camera parameters: cmvs-pmvs2 (Furukawa, 2010)
Convert depth and RGB image into point cloud
Manually clean point clouds
Align point clouds using cube edges (Ground Control Points)
Manually clean point clouds
Noise Filter (40 mm sphere) Final Kinect Point Cloud
Reference SfM point cloud using Kinect point cloud (GCPs and ICP when possible)
5 mm grid
Standard Deviation (Error)
GeoTiff image (Plots)
Meshing
Map for LC97_1 in 2012
Map for LC1e in 2012
Map for LC97_1 in 2012
Map for LC1e in 2012
Map for LC1e in 2013
FINAL MAPS

Figure 5.3: Processing workflow for the Kinect and Structure from Motion.

compared to a time of flight or scanning mode. In the time of flight method, the Kinect™ is moved over the surveying surface and programs such as KinectFusion (Izadi et al., 2011; Henry et al., 2012) process and merge data in real time. In this study, the Kinect™ is fastened at one extremity of a metallic support that is locked onto a tripod. This setup is pioneered by Mankoff and Russo (2012). A 12 V battery powers the Kinect™ and is fixed on the other end of the support, acting as counterweight as shown in figure 5.2a. The Kinect™ is positioned over a number of ∼1 m^2 areas that divides the area of the surveyed bedrock (Fig. 5.2a). Each zone is demarcated by four 5-cm wooden cubes placed on the bedrock. The cubes are later used to align each individual depth map.

A first survey was conducted on 25 March 2012 and covered an area of 2.5 m by 2.5 m upstream of LC97_1. The zone was divided into 13 sub-zones as shown on figure 5.4. A second zone of the same size was mapped near LC1e in April 2012. It was split into 17 areas of 1 m^2 (Fig. E.2).

The data extraction from the the Kinect™ follows the procedure described in Mankoff and Russo (2012). The method uses the open source library 'libfreenect' that is distributed by the OpenKinect community. It provides a 'record' command that exports the DN image live to a computer connected via a USB port until the process is 'killed'. The typical recording time per take is approximately one minute, during which $\sim$1 Gb of data is acquired including $\sim$1800 depth images in a 16-bit Portable Gray Map (PGM) format and the same number of RGB images in a 24-bit Portable Pixel Map (PPM) format.

The DN data $\{640, 480, t\}$ are then averaged over time in post-processing. This increases coverage and precision of the measurements. Figure 5.5 compares the results between the first image recorded by the Kinect™ (Fig. 5.5a for depth and and 5.5d for colour) and the average depth image that is computed from 100 and 1600 images (Fig. 5.5b 5.5e) along with their respective standard deviation (Fig. 5.5c and 5.5f). In the first image, the signal is lost in a zone with strong light reflection due to the presence of a thin water film on the bedrock. By compiling 1600 images, an intermittent signal can be detected in this zone and this increases the coverage of the measurements. Moreover, averaging 1600 images instead of 100 images shows the improvement of the signal to noise ratio and resulting precision by nearly 2 DNs. This corresponds to less than 3 mm when the Kinect is placed a 1 m above the bedrock (Fig. 5.6). The depth image $\{pixel, pixel, DN\}$ and RGB image are then calibrated into spatial coordinates with associated colour $\{x, y, z, r, g, b\}$ using the manufacturer parameters internally saved in the Kinect™. The program 'kinect_register' maintained by Mankoff and Russo (2012) extract these internal parameters and converts the averaged image into a point cloud containing about 300 000 points in a Polygon File Format (i.e. .ply).

The alignment of each mapped area is done manually using point clouds and ground control points defined by cubes placed on the bedrock. The order of the alignment follows the collection order of the different zones. The original reference is point cloud n. 1 (5.4 and E.2). The point clouds are aligned, merged and then become the new reference system. Each subsequent point cloud is then aligned to and merged with this new system. The referencing is normally based on four corners of two cubes. However, when a point cloud has two concomitant edges with the referenced and merged point cloud then three cubes serve as ground control points. The final map is generated when all point clouds

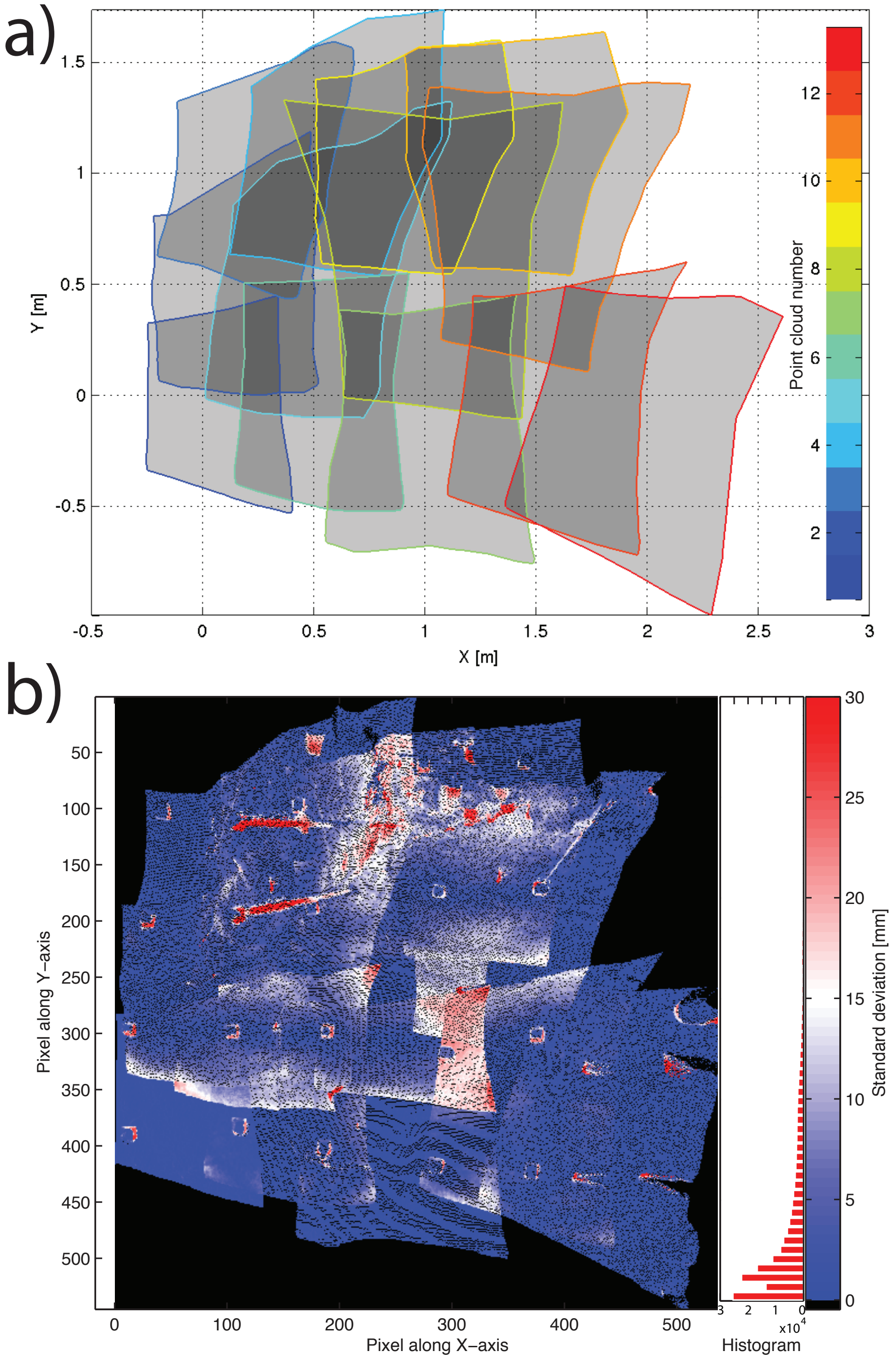

Figure 5.4: Effect of aligning Kinect tiles on elevation errors (non-propagated) for the area close to LC1e. a) Outline of each mapped zone. The covered areas are shaded and transparent. Darkening of the map indicates an increase in point density. b) Standard deviation computing from a 5 mm radius moving sphere.

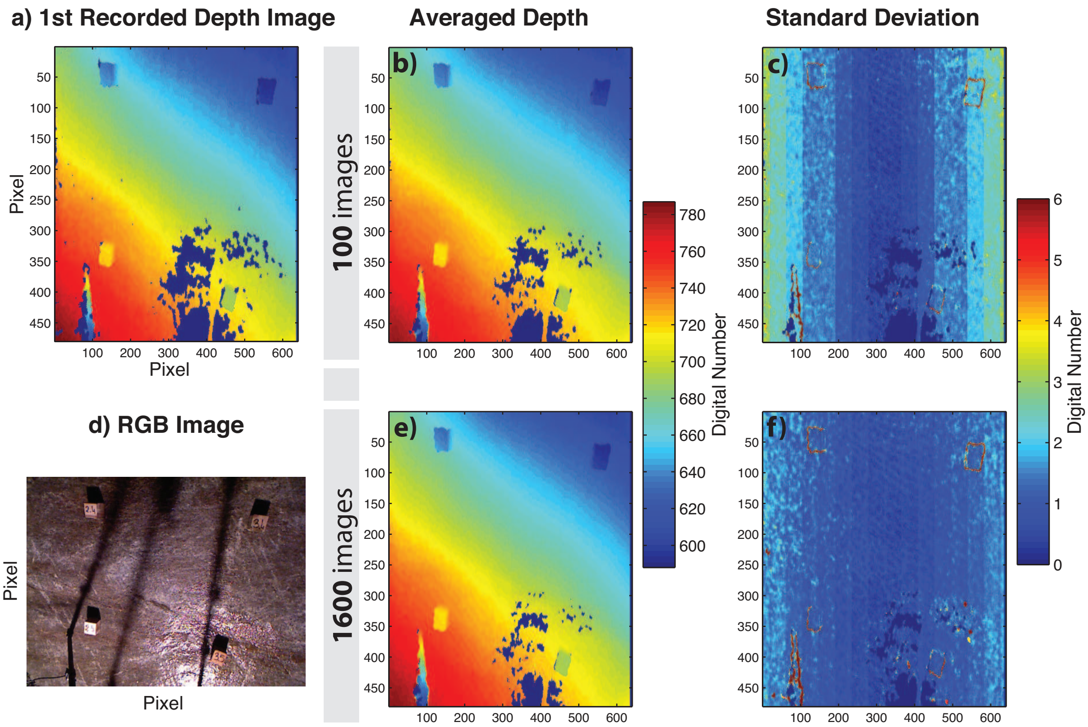

Figure 5.5: Improvement of the Kinect measurements by averaging large number of images. a) First recorded depth image (axis are not equal). b) Averaged depth and c) standard deviation for 100 images. d) First recorded RGB image. b) Averaged depth and c) standard deviation for 1600 images.

are joined together. This point cloud still contains artefacts from the operation of the Kinect such as steel bars that maintained cubes in steep areas or the legs of the tripod. They are manually identified and the affected parts are deleted.

5.3.2 Structure from Motion

The survey of the bedrock for the SfM method was conducted separately to the Kinect campaigns. A first set of 82 images was taken of the bedrock surrounding LC97_1 in March 2012. The zone near LC1e was covered twice in April 2012 and April 2013 and consisted of 69 and 240 photos, respectively. The details of the cameras used are given in table 5.1. The 2012 surveys used a compact camera with a highly distorted focal length of about 4. The photos do not follow a particular track, but include a large variety of angles from few points. In contrary, a more structured and along track pattern increased the coverage of the bedrock during the 2013 campaign. The SLR camera used is also of better quality with a larger sensor and a less distorted lense (Tab. 5.1).

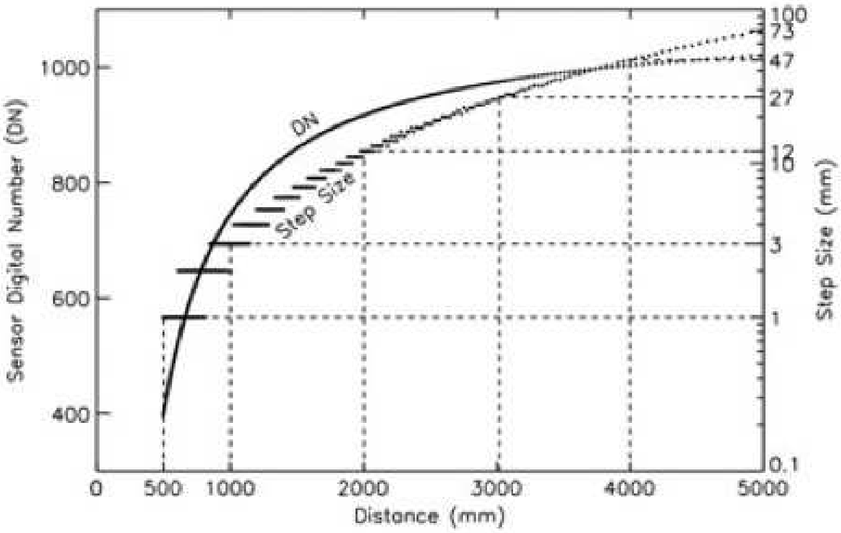

Figure 5.6: Accuracy and precision of the Kinect from Mankoff and Russo (2012)

Cameras	Collection	Dimension	Focal length	N. of images
Panasonic compact DMC-TZ18	26 March 2012	4320x3240	4.3	82
Panasonic compact DMC-TZ8	April 2012	4000x3000	4.1	69
Canon EOS 550D	18 April 2013	5184x3456	33	240

Table 5.1: Details of cameras and images used in the SfM technique.

The point clouds are generated directly from the collected set of photos. They are computed using the Open Source SfM software, VisualSfM (Wu, 2011) that implemented the workflow described in section 5.3.2 (Fig. 5.3). The large coverage of the images often contains points on the edge of the bedrock from debris in the ice. The selection and removal of these points are done manually.

The cleaned point cloud is then scaled and co-registered to the Kinect point cloud. An independent local referencing was set during fieldwork but the localisation of the ground control points could not be computed from the field measurements. First, pairs of points are identified in the two clouds. They are determined based on features in the rgb colour and shapes of the clouds. A rotation/transformation is applied to the SfM point cloud and minimises the error between pair of points. Few pairs are removed if it increases the final root mean square. A minimum of 6 pairs of points are used. The referencing is then improved using the iterative closest point method (ICP). This iteratively computes point to point differences and transforms the point clouds until a mean squared error between the reference and the model reaches a threshold. This fine alignment works best when the surface is rough and shows marked 3D features. The zone covered by the Kinect (i.e. the reference) near LC1e is, for instance, too uniform to use it. The resulting clouds are finally scaled to the Kinect point cloud. Although it lacks geo-referencing, the final cloud has the advantage of being spatially coherent and keeping the overall structure of the bedrock. Points are linked between each other from the set of images whereas the Kinect point clouds are aligned with each other (Fig. 5.4).

5.4 Results

The Kinect and the SfM technique were combined during three field campaigns and the bedrock adjacent to the load cells LC1e and LC97_1 was mapped.

5.4.1 Mapping near LC97

Figure 5.7 shows the result of the Kinect mapping near LC97_1. It combines 13 zones of 300 000 points for a total of ∼ 3.9 million points. A noise filter with a sphere of 40 mm reduced the number of points to about 2.7 million points. The bedrock slopes from left to right and has a 1-2 m step in the top left corner. The step gives rise to a gentle bump, where load cells LC97_1 and LC97_2 are installed. They are located on the lee side relative to the sliding direction of the glacier (Fig. 3.3). A fracture at the surface of the

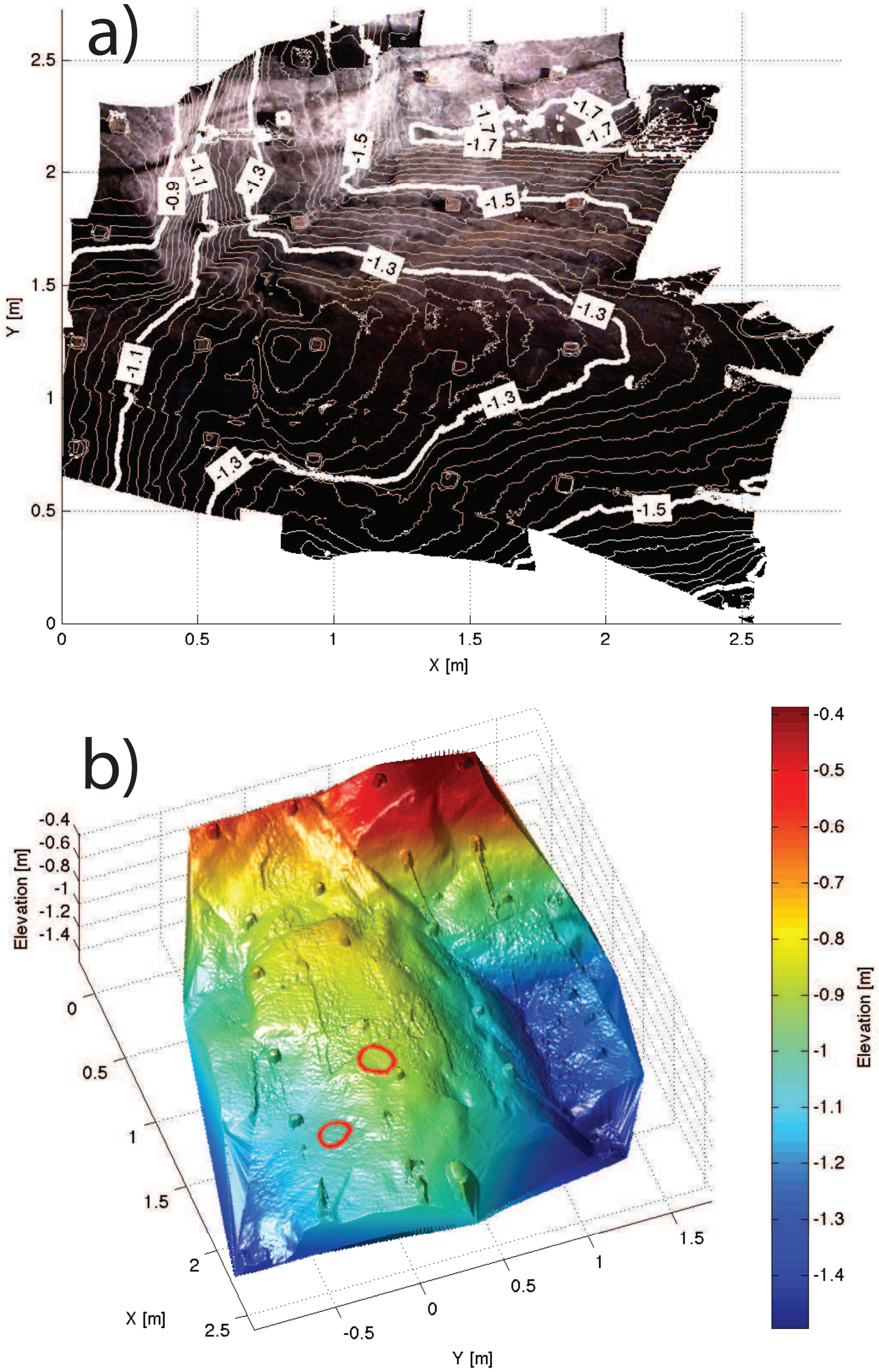
a)
-0.9
-1.1
-1.3
-1.5
-1.7
-1.7
-1.7
-1.7
-1.5
-1.3
-1.3
-1.1
-1.3
-1.3
-1.5
Y [m]
0
0.5
1
1.5
2
2.5
X [m]
0
0.5
1
1.5
2
2.5
b)
Elevation [m]
-0.4
-0.6
-0.8
-1
-1.2
-1.4
X [m]
0
0.5
1
1.5
2
2.5
Y [m]
-0.5
0
0.5
1
1.5
Elevation [m]
-0.4
-0.5
-0.6
-0.7
-0.8
-0.9
-1
-1.1
-1.2
-1.3
-1.4

Figure 5.7: Mapping of the zone adjacent to the load cells LC97_1 and LC97_2 generated from the Kinect method. a) Composite image and contour lines. b) 3D view of the final DEM with load cell positions highlighted with red circles.

bedrock is observed upstream of the load cell and perpendicular to the longest axis of the bump. Some artefacts are observed in figure 5.7b. For example, some parts of the steel bars holding the cubes on the step are still visible. They could not be entirely deleted without removing points from the bedrock, so they remained in the Kinect point cloud. The bedrock surface also shows artefacts at the limits of point clouds. They correspond to a co-registration mismatch of the Kinect point clouds.

The Structure from Motion technique in the zone near LC97_1 has a better coverage than the Kinect (Fig. 5.8). However, the texture of the map in the figure 5.8b indicates a coarser resolution. This is marked by a lower density of points, ~ 2.6 million points for a covered area roughly 20% wider than the Kinect area. The density of points also decreases in the steepest parts of the bed (e.g. near the step and fractures).

5.4.2 Mapping near LC1e

The second zone mapped with the Kinect is characterised by a gently sloping bed (Fig. 5.9). Load cell LC1e is installed in the bottom left corner and surrounded by vertical walls that inhibited the mapping with the Kinect. This part of the bed is wider than the previous map and is divided into 17 zones (Fig. E.2). The total number of points is about 3.5 million after applying the same noise filter as above. Artefacts from the tripod legs, feet of the operators or caused by mismatch between Kinect point clouds are also less evident.

The map coverage is improved with the SfM especially on the vertical walls behind the load cell LC1e (Fig. E). This point cloud can be considered as a 3D object instead of a 2D surface as shown in figure E.4 where camera positions are plotted. Two point clouds of the same area were produced with SfM one for April 2012 and another one for April 2013. They are registered to each other using an Iterative Closest Point method after a rough manual alignment. The merging of the two point clouds complements missing parts of the bed and extends the area composed of ~ 2.7 million points. The vertical wall to the 'west' of LC1e is parallel to the sliding direction, whereas the one to the 'south' is perpendicular. Perhaps, this geometry causes the ice to stagnate or at least to slow down in this corner. They show evident fractures on their surfaces.

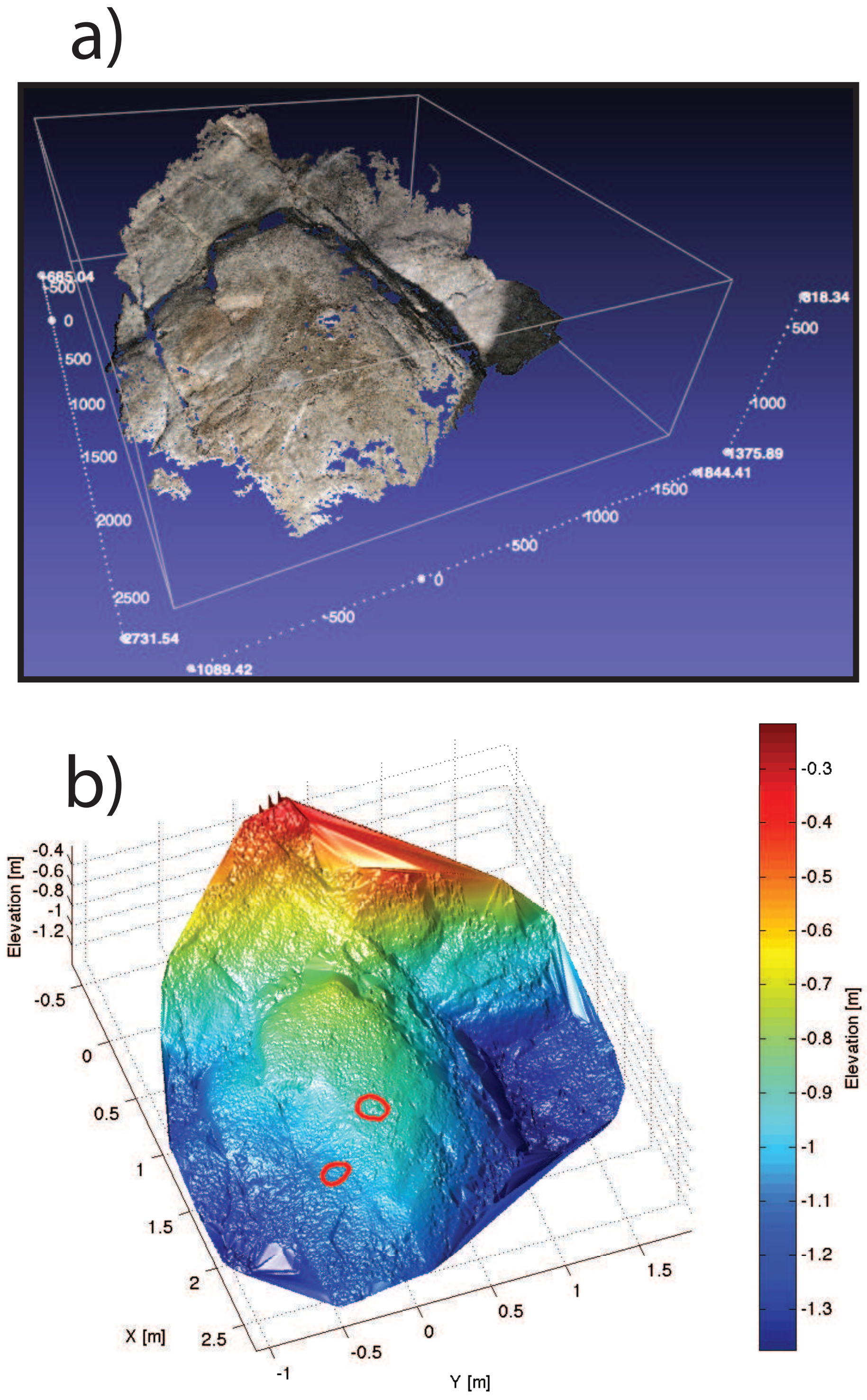
a)
685.04
500
0
500
1000
1500
2000
2500
2731.54
1089.42
-500
0
500
1000
1500
1844.41
1375.89
1000
500
818.34
b)
Elevation [m]
-0.4
-0.6
-0.8
-1
-1.2
-0.5
0
0.5
1
1.5
2
2.5
X [m]
-1
-0.5
0
0.5
1
1.5
Y [m]
-0.3
-0.4
-0.5
-0.6
-0.7
-0.8
-0.9
-1
-1.1
-1.2
-1.3
Elevation [m]

Figure 5.8: Referenced and scaled point cloud produced with the Structure from Motion method in the surrounding of load cells LC97_1 and LC97_2 (circles). 3D view of a) the point cloud with overlaid RGB colour and b) the elevation map.

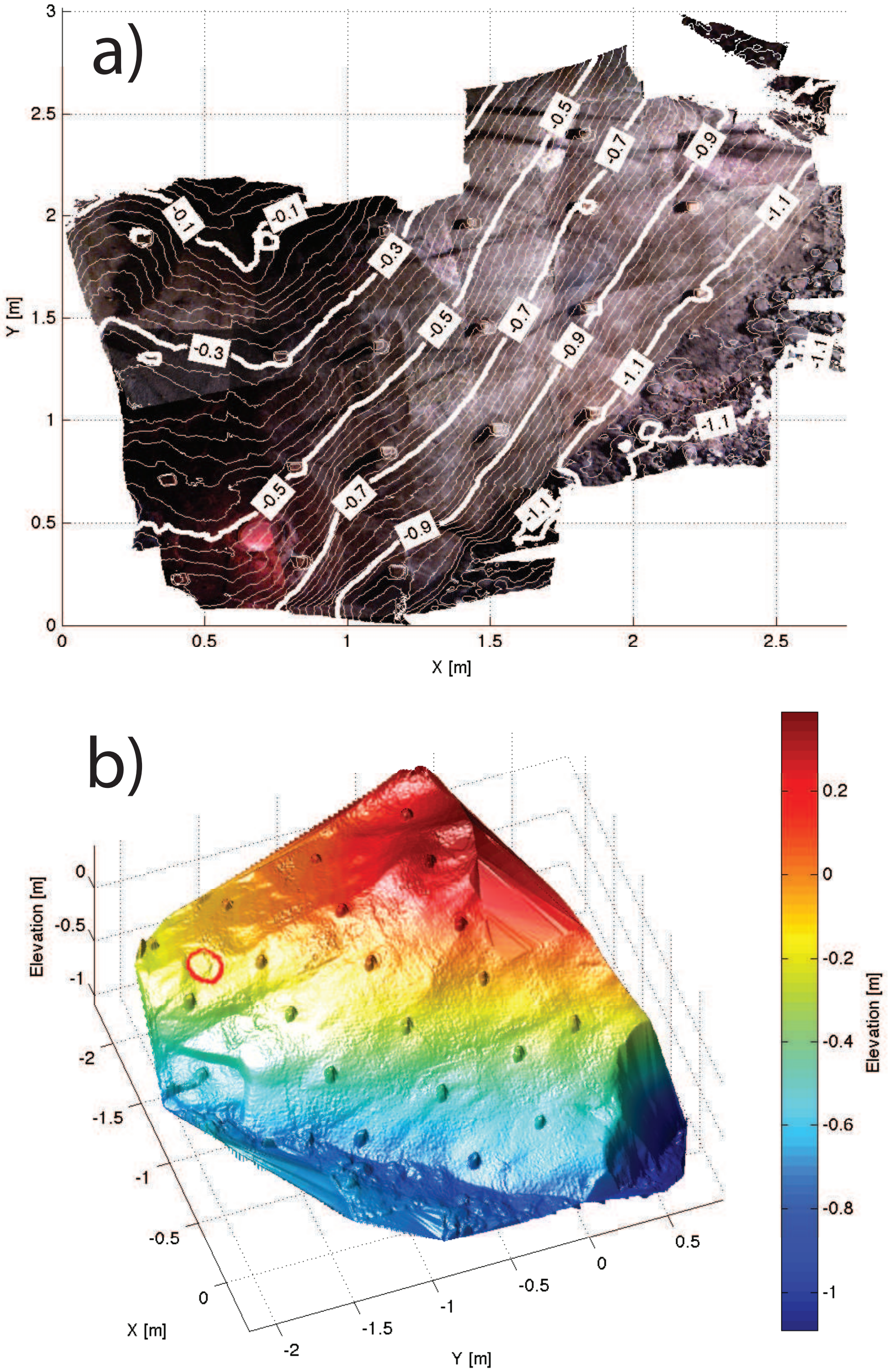
a)
3
2.5
2
1.5
1
0.5
0
Y [m]
0
0.5
1
1.5
2
2.5
X [m]
-0.1
-0.1
-0.3
-0.3
-0.5
-0.7
-0.9
-1.1
-0.5
-0.7
-0.9
-1.1
-0.5
-0.7
-0.9
-1.1
-1.1
-1.1
b)
0
-0.5
-1
Elevation [m]
-2
-1.5
-1
-0.5
0
X [m]
-2
-1.5
-1
-0.5
0
0.5
Y [m]
0.2
0
-0.2
-0.4
-0.6
-0.8
-1
Elevation [m]

Figure 5.9: Bedrock map in the vicinity of the load cell LC1e as measured by the Kinect. a) Composite image of the bedrock and contour lines. A red light illuminates LC1e. b) DEM of the bedrock with shaded relief. The location of the load cell is circled in red.

5.5 Discussion

The Kinect and Structure from Motion are two suitable techniques for mapping subglacial bedrock. We discuss below the issues encountered during fieldwork and post-processing for both techniques. Scaling and referencing of the point clouds are the main obstacles for studying bedrock geometry and subglacial processes.

5.5.1 Kinect errors

The most important questions with the Kinect method are how to reduce the errors and how to minimise error propagation. It is especially important to understand these errors because they affect the referencing of the Structure from Motion point cloud (section 5.5.2).

First, the calibration from DN to distance corrects for instrumental biases including focal length, principal point offsets, lens distortion coefficients, base length and distance of the reference pattern (Khoshelham and Elberink, 2012). The calibration used here includes these intrinsic parameters of the Kinect (Mankoff and Russo, 2012) and has an accuracy of ± 3 DN and 3 mm spatial resolution at about 1 m (Fig. 5.6).

The main internal error that affects the precision originates from changes in wavelength of the infrared laser due to temperature variations. A temperature stabiliser corrects these fluctuations, but responds with a delay (i.e. switching on and off) that leads to this error (Mankoff and Russo, 2012).

Precision errors are also related to the field of view as shown in figure 5.5c. The standard deviation of DN increases to the sides. The signal to noise ratio is reduced by averaging depth images (Fig. 5.5e, Mankoff et al., 2011). This improvement, which is of the order of few DNs, is more and more important as the distance range increases (Fig. 5.6). During fieldwork, the Kinect was placed about 1 m above the bedrock and so the precision is about 3 mm.

Averaging of depth images is also useful in detecting errors from the surface property. Reflection of light on wet surfaces and steepness of the bedrock cause the depth signal to be less precise. These errors can be masked out with a threshold on the standard deviation. During fieldwork, the sensor saturation due to light reflections can also be reduced by removing light sources after a few seconds. Nevertheless, a few seconds of illumination is necessary to obtain useful rgb images for the point cloud and surface details. Features on the bedrock are important for identifying additional ground control points.

The largest errors in the final point cloud originate from the alignment of the Kinect point clouds in order to construct the final composite map. The map orientation depends on the first point cloud that defines the coordinate system of reference. However, the Kinect was not precisely levelled during fieldwork and the reference cloud may not be on the exact horizontal plane thus inducing a tilt into the final map. Ground control points with absolute coordinates can correct this problem, but were not available.

The tilt error is probably negligible compared with the propagation of errors during the point cloud co-registration. The position of the control points used for the manual alignment of each point cloud are not randomly distributed. The edges of the cubes are nearly coplanar as they often delimit only one side of the mapped zones (e.g. two cubes, one in the top-left and the other in the bottom-left corner). This decreases the accuracy of the alignment and causes an exaggerated rotation on the other side of the point cloud. This problem is seen in the deformation of the point could outlines in figures 5.4a and E.2a. The first and last co-registered point clouds are particularly subject to this error because the co-registration is based only on two cubes. This problem is reduced when the merged point cloud has three cubes in common with the point cloud to be aligned.

5.5.2 Structure from Motion errors

The SfM point clouds have better spatial coherence, but lower spatial resolution than the Kinect maps. The main problem with the Structure from Motion method is its dependence on the Kinect point clouds for scaling and referencing. The alignment of the point clouds propagates the errors from the Kinect processing. Thus, the uncertainty in the Kinect map and the lack of absolute coordinate system affects the quality and use of the co-registered SfM point clouds. For instance, the location of bedrock features do not exactly match between the two maps (e.g. grooved marks).

To avoid this issue, an independent reference system was installed during the 2013 SfM field campaign by drilling markers in the bedrock. However, the exact position of the drilled holes cannot be retrieved because the distances between three reference points used for triangulation are lacking. The drilled holes are still in place and so the system of markers can be re-surveyed. This reference system offers consistent ground control points for future mapping campaigns and can be linked to the absolute coordinate system of the tunnel network.

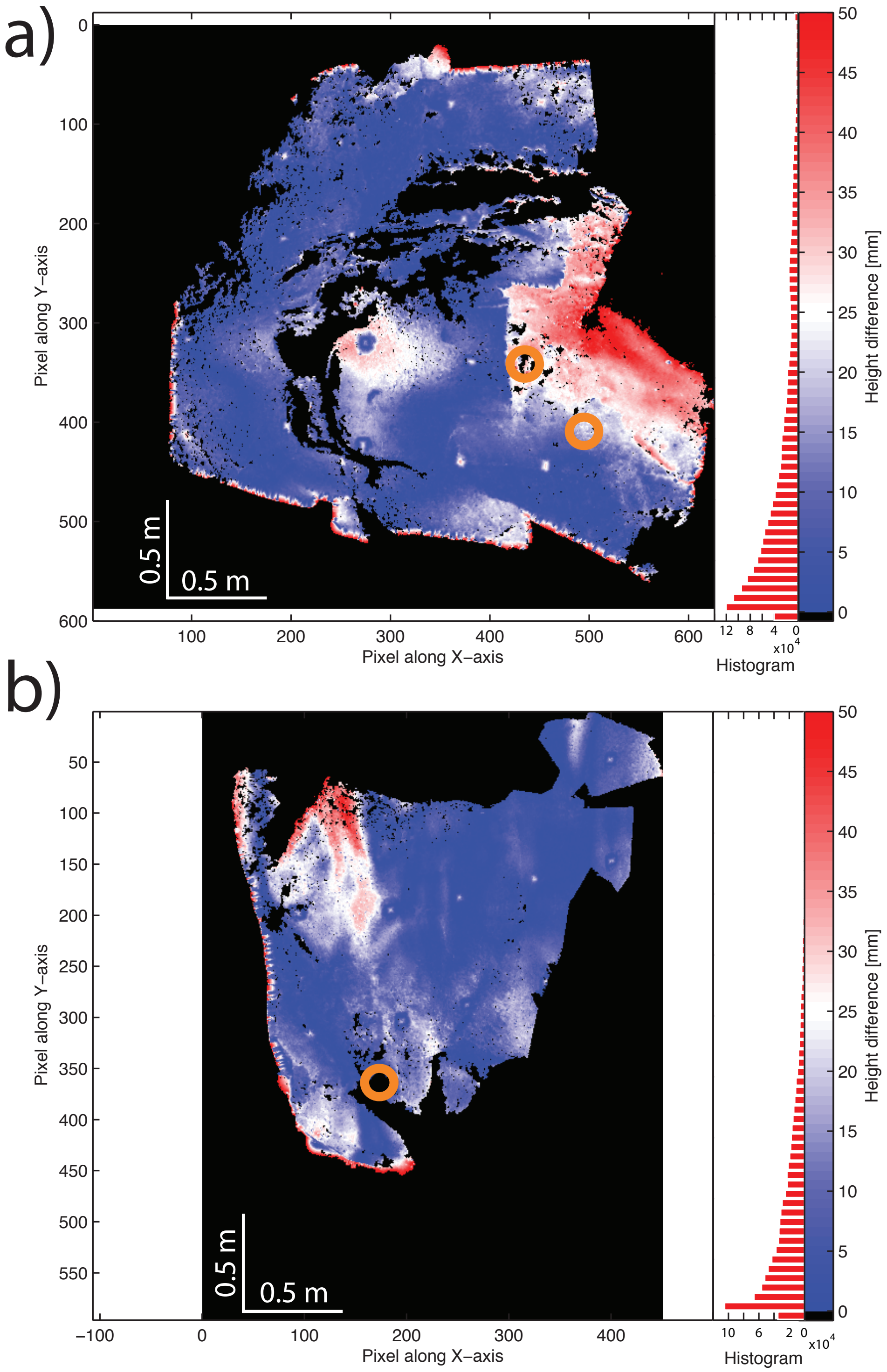

Figure 5.10: Absolute height difference between the Kinect and co-registered SfM point clouds for the zones a) near LC97_1/LC97_2 and b) near LC1e (data collected in 2012). The location of the load cells is highlighted with orange circles. 100 pixel is equivalent to 0.5 m.

5.5.3 Map comparison

The map of the bedrock surrounding load cell LC97_1 exhibits evident alignment errors (Fig. 5.4a and 5.4b). The difference between the Kinect and Structure from Motion maps in figure 5.10a is concentrated in the centre right part, and follows the limits of the three last aligned point clouds (e.g. point clouds 11-13 in figure 5.4a). One reason for this misalignment is a bad co-registration of point cloud n. 12 that is done using one cube because the second one is out of the field of view. The other reason is a propagation of a low score in co-registration of point clouds n. 8 and 9. The obtained root mean square for these point clouds is 2 to 4 times greater than the median for the rest of the point clouds (i.e. 4.3 ± 0.6 mm). This error is introduced because several point clouds overlap in the steep area, which creates noise and uncertainty in the ground control points although three cubes were used (Fig. 5.4b). It is also possible that the high root mean square is inflated because a small alignment error in the steep part causes a greater elevation difference. The pattern of the co-registration errors is highlighted at the border of two point clouds and is seen in both the standard deviation of the point cloud (Fig. 5.4b) and when compared to the SfM point cloud (Fig. 5.10a). A zone of error in the centre of the map is different and may be associated to the Iterative Closest Point (ICP) method that over-fitted the SfM point cloud to the reference Kinect map. Because it has a more robust spatial coherence and cover a larger area then the Kinect, the ICP may have compressed the SfM map to fit the Kinect map, leading to this bulge pattern. The SfM and Kinect results are otherwise in good agreement, as expected from the ICP.

The map of the zone adjacent to LC1e is in better agreement with the SfM map of the area as seen in the histogram of the difference in figure 5.10b. This area is less subject to alignment errors (Fig. 5.9b). This improvement is a result of a better visibility of features on the bedrock in the rgb images. The identification of features that are consistent between two point clouds served as additional ground control points. Lights projected on the bedrock during fieldwork increased the image contrast. The drawback is a deterioration of the depth signal from light reflections on the bed and sensor saturation. The errors are furthermore reduced because the terrain near LC1e is more regular and monotone. Large deviations are thus less likely to occur and for instance observed only near the vertical faces of the cube (Fig. E.2b). The differences with the SfM point cloud show slight rectilinear patterns that follow the alignment of the Kinect point clouds (Fig. 5.10b). The largest errors are observed on the edges of the map and in the top-left corner. The error in the corner is related to an insufficient number of ground control points for aligning the point cloud of the Kinect (Fig. E.2a). The quantitative assessment of the combined errors from the point cloud and alignment (Fig. E.2b and 5.10b) suggests that the accuracy and precision of the bedrock elevation are on the order of centimetres and in some parts can reach a resolution of a few millimetres.

5.6 Conclusion

The Kinect and Structure from Motion methods were used together to map the bedrock under the glacier. The Kinect results are altered by errors that propagate during the alignment of mapped zones. Nevertheless, the spatial resolution is of high quality (>3 mm) and in some parts reaches the millimetre vertical accuracy needed to investigate erosion rates. For this purpose, the coordinate system of the map has to be converted from relative into an absolute coordinate system. The SfM method extends the Kinect maps of the bedrock, but depends on the Kinect maps for scaling and referencing. However, the SfM method was lighter to carry and simple to set up, thus making it easier to use for fieldwork. This is why the SfM method is preferred to the Kinect, although effort is needed to obtain a reference network of points with absolute coordinates to co-register the SfM point clouds.

These maps gives us useful information on the general bedrock geometry and can be incorporated into models. The point cloud resolution is so fine (millimetre precision in some parts) that it has to be reduced for modelling purposes. However, the accuracy and precision of the Kinect point clouds and registration issue of the SfM point clouds limit their use to study erosion rates from repeated mapping.

Chapter 6
Effect of cavity contraction on basal pressure

A melted cavity,
Under 200 metres of ice

Mathieu Tachon

6 Effect of cavity contraction on basal pressure

This chapter investigates the effect of stress bridging on the temporal variation in normal stress by comparing a field experiment conducted at the Svartisen Subglacial Laboratory with a model study. The experiment consists of melting out an artificial cavity over load cells LC97_1 and LC97_2 and monitoring pressure as the cavity contracts and the ice migrates over the load cells. A peak in pressure at the glacier bed is observed during the experiment. Modelling of the contraction of a cavity reproduces the time evolution of normal stress at the glacier bed. This shows the effect of cavity geometry and ice rheology on the characteristics of the observed peak.

6.1 Background

Observations from load cells installed at the glacier bed of Engabreen show that basal pressure can reach values exceeding the local overburden pressure on a daily basis (chapter 4 and Fig. 6.1). This increase takes the form of a peak in pressure and is assumed to be caused by stress bridging effect near subglacial cavities and wherever parts of the glacier bed are decoupled from bedrock (Weertman, 1972; Van Der Veen and Whillans, 1989; Lappegard, 2006b). Stress bridging describes the transfer of the load of the ice overlying the roof of a subglacial cavity to the sidewalls of the cavity. Shear stress transfers the load of the ice to zones in contact with bedrock. The result is a local increase in normal stress at the bed.

A typical example of the peak in pressure is shown in figure 6.1 (Lappegard, 2006b). These observations show that the upstream load cell LC97_1 initially measures ice pressure and the downstream load cell LC97_2 water pressure in a subglacial channel. During day 190, a subglacial channel grows and connects both load cells until water pressure decreases. The channel then contracts and the upstream load cell LC97_1 records a peak in pressure nearly twice the overburden pressure (∼1.8 MPa). The nearly instantaneous

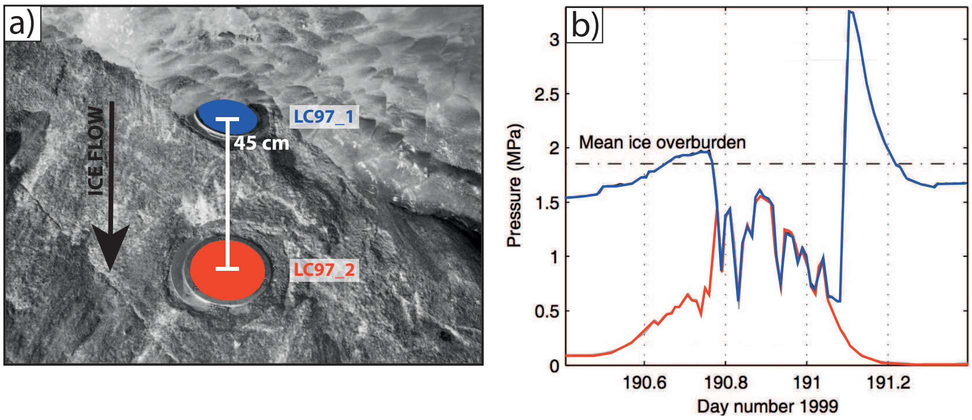

Figure 6.1: Observations of channel migration from the load cell record. a) Location of load cells LC97_1 (blue) and LC97_2 (red), and ice flow direction. b) Pressure changes showing the load cell pressure response to channel migration for the period 9-10 July 1999 (day of the year 190 and 191). The channel migrating over the upstream load cell causes a peak in pressure much greater than the overburden pressure (adapted from Lappegard (2006b)).

increase in pressure is assumed to be related to the edge of the channel regaining contact with the bedrock, while pressure at the downstream load cell LC97_2 falls to atmospheric pressure. After the peak, pressure at LC97_1 decreases exponentially to its previous background level in less than 5 hours. The rapid decrease is assumed to be controlled by how fast the edge of the channel migrates over the load cell that depends on ice deformation and sliding.

A model of stress bridging near a subglacial channel demonstrated that it can reproduce a peak in pressure similar to that observed (Lappegard, 2006b). The normal stress distribution at the bed peaks at the edge of the channel and decays exponentially away from it. The magnitude of the maximum pressure varies according to channel size, geometry and ice rheology, but reaches the same order of magnitude as observed in the subglacial laboratory (Fig. 6.1). However, the model considers a channel at steady-state and ignores the temporal variation that is observed in the load cell record (Lappegard, 2006b).

6.2 The Contraction of an Artificial Cavity

Measurements were undertaken at Svartisen Subglacial Laboratory (SSL) between 12 and 17 November 2012 (Fig. 3.1). Two artificial cavities were melted out in order to uncover the load cells LC97_1 and LC97_2 that passively recorded pressure changes at a 2-min interval (Fig. 3.3 and 6.2). The aim of the experiment was to study the peak in pressure measured by the load cells. The creep closure of the cavity is measured using an original application of the Kinect that is not only used for mapping bedrock and the result is validated against measurements of markers screwed in the ice (Fig. 6.3 and 6.4). The pressure peaks recorded at load cells LC97_1 and LC97_2 are characterised and compared to the closure rate as well as observations of ice coverage over the load cell plate (Fig. 6.5).

Access to the glacier base is through the horizontal research shaft using a hot-water drilling system (section 3.1.2). Steel bars that prevent intrusion of ice in the tunnel are first removed and then melting of the ice goes on until the load cells are reached. The periods of melting are shown in figure 6.5. During the later stage of the melting time (especially in the second cavity), the walls of the cavity are smoothed and shaped by manually controlling a narrower water jet. A simpler shape enhances the quality of the creep closure measurements and the comparison with the model of the subglacial cavity. The first man-made cavity (13-14 Nov.) has a small overhang above the load cells and is higher than the second cavity (15-16 Nov.), which has a more elliptical shape (Fig. 6.2).

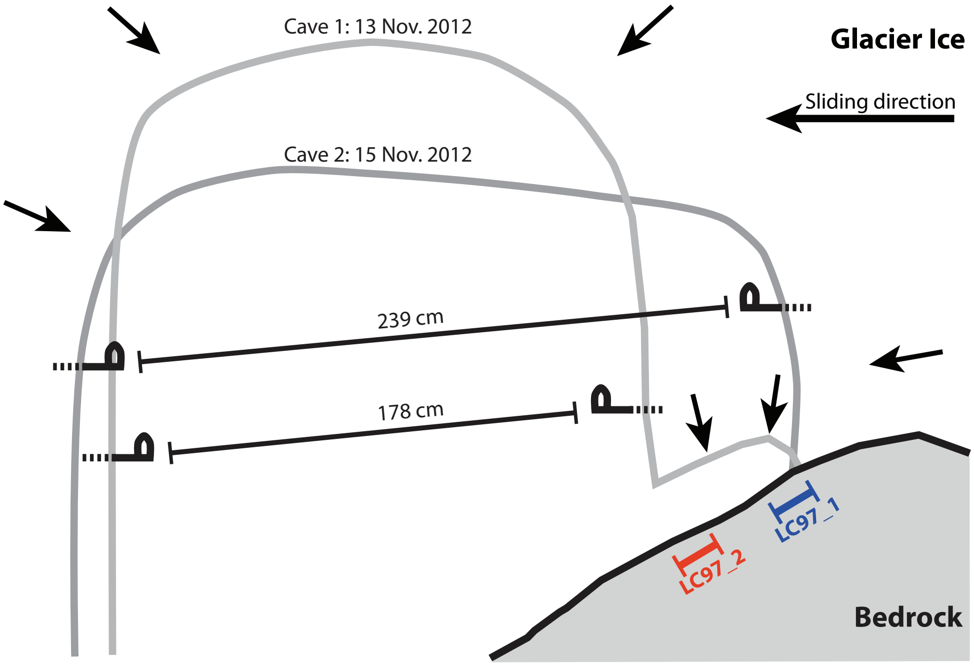

Figure 6.2: Approximate cross-sections of the two cavities melted on 13 and 15 November 2012. The cavities are drawn based on field observations and the width of the cavity measured between two markers drilled in the ice (black screws). The arrows indicate direction of creep closure.

6.2.1 Measurement of Closure Rate from Markers

Markers are drilled in the ice on each side of the cavity parallel to the prevailing sliding direction. In order to obtain the closure rate of the cavity, the distance between the markers is measured three times at irregular intervals during the contraction of the first cavity and every 1-3 hours, simultaneous with the Kinect measurements, for the second cavity (Tables F.2 and F.4). The computed closure rate takes into account the ice deformation from 1) the downstream and 2) upstream ice wall and 3) sliding of the glacier along the bed. The components are not separated in this study, sliding is assumed constant and ice rheology to be isotropic. Sliding contributes to 15±7 cm.day^{-1} according to previous measurements (Cohen et al., 2005; Lappegard, 2006a). The closure rate from the markers is thus divided by two to approximate the mean closure rate. This is compared with the contraction rate of the upstream ice wall as measured by the Kinect. The mean closure rate underestimates the contraction of the upstream side of the cavity relative to the Kinect because the closure rate is asymmetric and the upstream wall contracts faster due to sliding.

The shorter the time interval, the larger the error in closure rate. A total error of 5 mm in the marker measurement gives an error of 12 cm.day^{-1} in the mean closure rate for a period of an hour ($dx_{error}/dt \cdot 24$ includes conversion from cm.hr^{-1} to cm.day^{-1}). The error decreases to 1.3 cm.day^{-1} for the longest time interval between two measurements (i.e. 9 hours). The error in closure rate may be larger as the ice screws were observed to rotate due to ice flow and ice to deform at the base of the markers changing the distance between the measured surface and the marker. The closure rate computed from the distance between two markers is used as a reference in order to validate the Kinect measurements within the measurement error.

6.2.2 Short-Range LiDAR and Closure Rate

The setup of the Kinect for measuring the contraction of the cavity is similar to that for mapping bedrock (Chapter 5). The Kinect sits at the end of an arm that is attached to a tripod. The main difference is that the sensor is installed in a fixed position, vertical and facing the cavity wall (Fig. 6.3), instead of placed at different locations, horizontal and facing down. The Kinect was placed high enough, approximately 1.50 m above the bed, to have a field of view covering a part of the bedrock, the ice wall, the load cells and one of the markers. The bedrock is also mapped as it can be used to reference the point clouds and correct possible motion from the Kinect. Assuming that the Kinect is

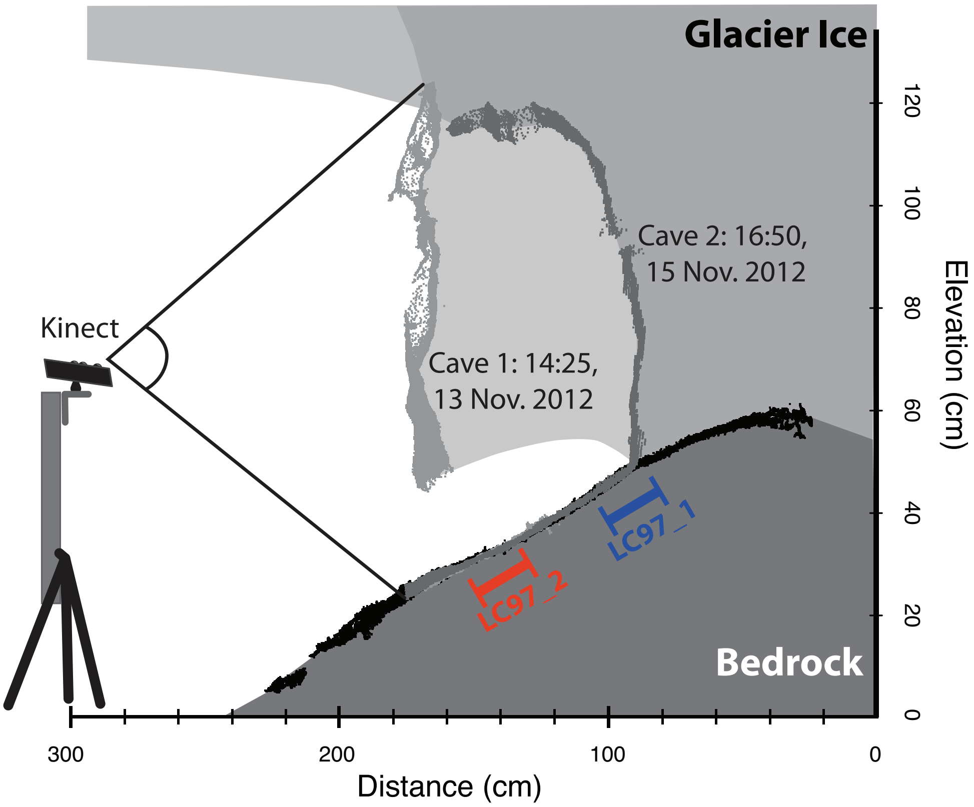

Figure 6.3: Cross-section of the two cavities surfaces extracted from the Kinect point clouds and obtained at 14:25 on 13 Nov. and 16:50 on 15 Nov.. They are referenced to the SfM point cloud of the bedrock derived in chapter 5. Location of load cells LC97_1 and LC97_2 is shown in blue and red. The point clouds are in a relative coordinate system (see chapter 5).

fixed over time, it is possible to record 3D point clouds of the ice wall at different times and compute displacement and then closure rate. This novel application required the development of a particular post-processing protocol and is described below.

Measurements of the wall 3D surface follow the same procedure as in chapter 5 (Fig. 6.4). The Kinect is manually activated every 1-3 hours to record depth and rgb images for one minute (see Tables F.1 and F.3 for more details). The depth is averaged from ∼1600 collected images at each pixel. The conversion of the averaged depth image and rgb image into a point cloud of ∼300 000 points is done using the Kinect-calibrated software 'kinect_register' (Mankoff and Russo, 2012).

The spatial resolution and distance accuracy of the point cloud depends on the distance between the Kinect and the cavity wall (Fig. 5.6). The lowest obtained spatial resolution is 5 mm and 10 mm when the wall of the first and second cavity was 1.2 m and 1.8 m away from the Kinect, respectively. The resolution improved to less than 1 mm, as the cavity contracts and the wall gets closer to the Kinect. The distance accuracy is about 3 mm at 2 m and increases to 1 mm at 0.5 m (Mankoff and Russo, 2012). The accuracy of the Kinect can deteriorate where there is high reflection on the cavity wall due to lights and where the surface of the cavity is tangential. However, this is restricted to defined areas that are easily identified by the noise in the point cloud and are removed manually. The transparency of the ice in the infrared wavelength (Kinect wavelength: 830 nm) can be problematic. Nevertheless, the melting out of debris on the surface of the cavity wall provides a suitable surface for infrared laser measurements. When the ice surface is clean, the signal is lost and no data are collected.

The collected point clouds are referenced into a universal coordinate system using the bedrock. This corrects possible displacement of the Kinect (Fig. 6.4). However, this correction is only applicable to the second cavity (15-16 Nov.), where bedrock is visible during the whole experiment. The Kinect was too close to the ice during the measurements of the first cavity (13-14 Nov.) and bedrock is quickly covered by the ice. The referencing consists of extracting the bedrock from each point cloud, defining a reference, applying a rigid transformation and rotation based on ground control points (e.g. manual alignment), and then automatically registering it using an iterative closest point algorithm (Fig. 6.4). Manual alignment is carried out only if a visible displacement was identified in the rgb image (Table F.3). Error in the alignment is estimated based on the root mean square of the registration, visual assessment of the point cloud, and spread of the error distribution between the reference point cloud and the corrected bedrock. The obtained transformation matrixes are then applied to the extracted point cloud of the ice wall.

The displacement between two point clouds collected at time t1 and t2 is obtained based on the nearest neighbour method (Fig. 6.4). First, the point cloud collected at time t1 is meshed using a Delaunay triangulation (i.e. best fitting plane) with a maximum distance threshold of 10 mm. This surface enhances the closest point differencing as nearest neighbour can be interpolated on the mesh to find the shortest distance with the points of the compared point cloud. Then, the closest point-to-mesh distance is computed between the mesh and the compared point cloud and comprises between 255 000 and 295 000 values. To go from 2D values to one closure rate estimate, the median, 25% and 75% quartiles are derived from the distribution of the absolute displacements and divided by the time interval t2-t1 (Tables F.1 and F.3). Fig. 6.5 shows the closure rate distribution as described by these three components.

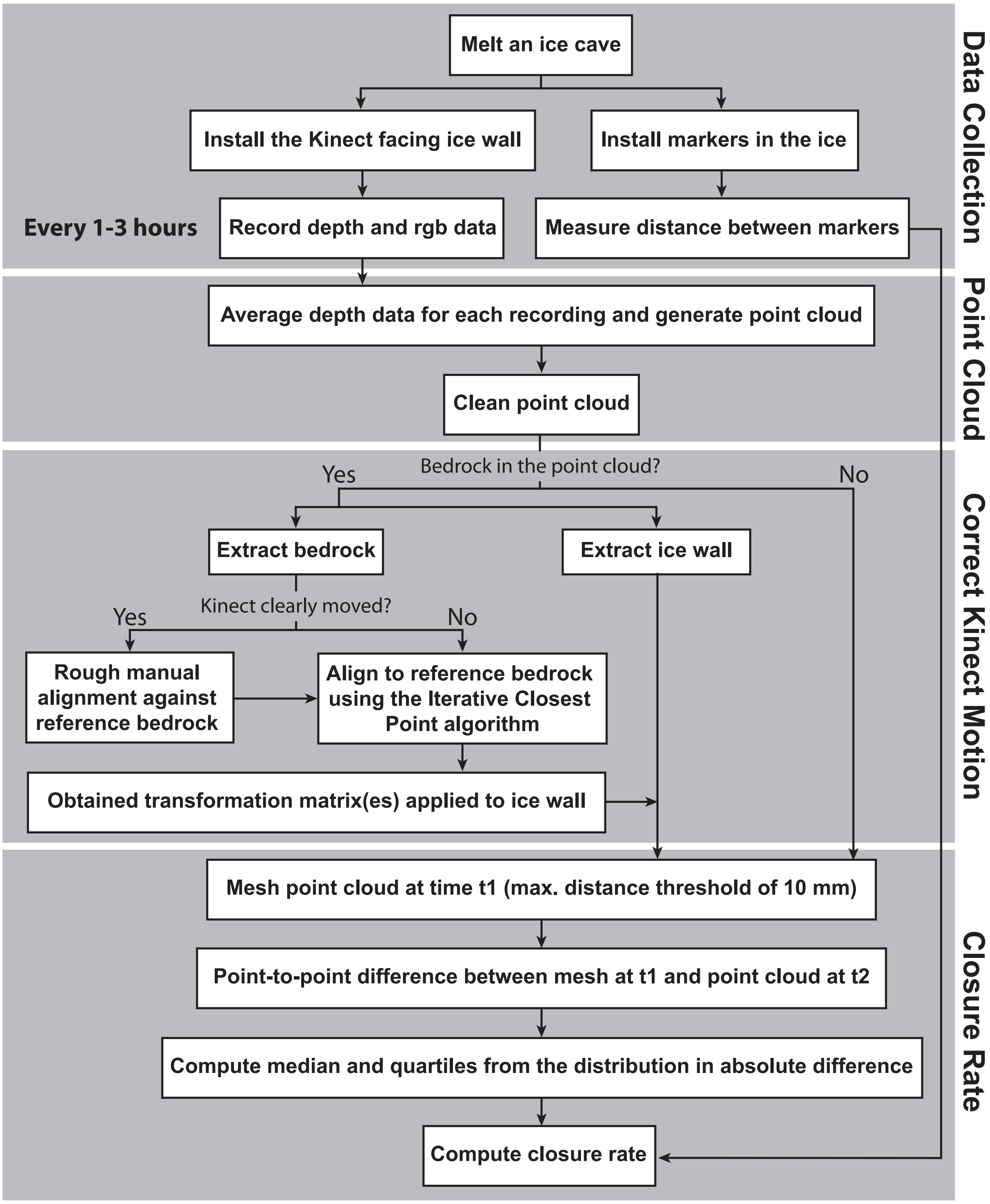
Melt an ice cave
Install the Kinect facing ice wall
Install markers in the ice
Every 1-3 hours
Record depth and rgb data
Measure distance between markers
Average depth data for each recording and generate point cloud
Clean point cloud
Bedrock in the point cloud?
Yes
No
Extract bedrock
Extract ice wall
Kinect clearly moved?
Yes
No
Rough manual alignment against reference bedrock
Align to reference bedrock using the Iterative Closest Point algorithm
Obtained transformation matrix(es) applied to ice wall
Mesh point cloud at time t1 (max. distance threshold of 10 mm)
Point-to-point difference between mesh at t1 and point cloud at t2
Compute median and quartiles from the distribution in absolute difference
Compute closure rate
Data Collection
Point Cloud
Correct Kinect Motion
Closure Rate

Figure 6.4: Workflow to calculate the closure rate of a subglacial cavity.

6.2.3 Results and Interpretation

The pressure on the load cell is measured during the contraction of two artificial cavities. The migration of the cavity wall produces a peak in pressure on the bedrock, but the peak intensity and timing differ across load cells and between the two cavities.

The pressure response is more marked during the contraction of the first cavity, especially at the upstream load cell LC97_1 (Fig. 6.5, 15-16 Nov.). This load cell measures a 2.05 MPa rise in pressure over 4 hours that corresponds to the ice migrating over the load cells (e.g. percentage of ice covering the load cell). The peak is followed by a 17 hour long decrease in pressure from 2.05 to 0.65 MPa. The exponential decay is similar in shape to the peak observed during natural cavity migration (Fig. 6.1), although the return to a stable level in pressure during the experiment takes three times longer. This slower decay is maybe due to a lower sliding rate in November compared to July (Fig. 6.1) that slows down cavity migration. A more modest peak is observed 25 hours later at the downstream load cell LC97_2. Pressure peaks to a maximum value of 1.73 MPa at 17:49, then decreases for 8 hours to reach a background pressure of 1.48 MPa. During the contraction of the cavity, the closure rate is nearly constant showing a slight increase from 19 to 21 cm.day^{-1} for the Kinect measurements and from 25 to 27 cm.day^{-1} for the manual measurements. Thus, the difference in shape of pressure peaks is not explained by temporal variations in ice flow.

The difference in peak intensity as measured by the two load cells may reflect the effect of the overhang/decoupling between ice and bedrock (Fig. 6.2). At the beginning of the creep closure measurements, the glacier already covers LC97_1. The cavity wall is 40 cm downstream and 20 cm above LC97_2, due to the realised melting of the cavity (Fig. 6.6). This overhang concentrates the load of a larger area of unsupported ice onto the load cell LC97_1, which leads to a distinct peak in pressure. In contrast, the peak at LC97_2 is dampened and occurs while the overhang closes onto the load cell, as indicated by the decrease in closure rate (i.e. 09:10-11:58 in Table F.1) and twofold reduction in vertical flow (i.e. 14:57-18:10 in Fig. 6.7). This increased contact surface between ice and bedrock enhances the distribution of the load on the glacier bed and reduces the normal stress onto the load cell as well as the intensity of the peak. The closure of the overhang also explains why the migration of the cavity wall, as defined by the timing of the peak between the two load cells (i.e. 45 cm in 25 hours), is twice as fast as the measured closure rate (i.e. ~20 cm.day^{-1}). This doubling in closure rate is caused by the migration of the wall parallel to the bed and the added downward flow of the overhanging ice.

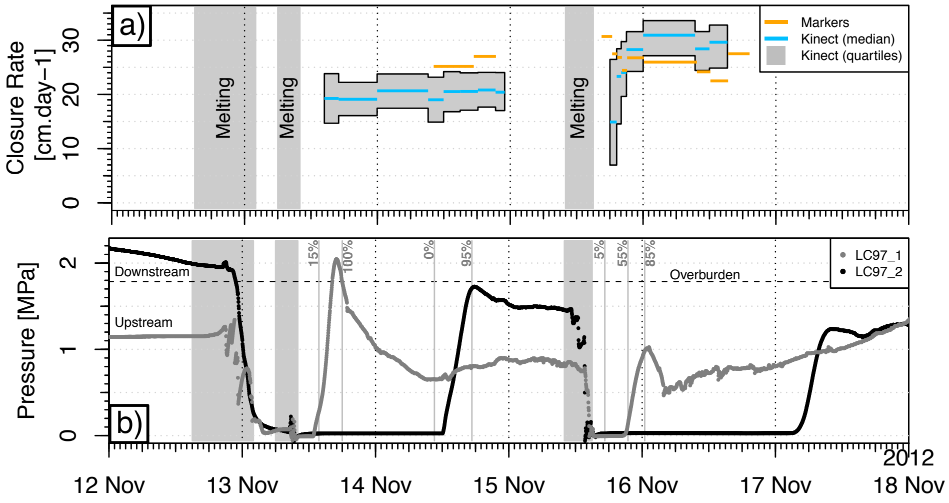

Figure 6.5: Pressure response during the contraction of two cavities between 12 and 18 November 2012. a) Closure rate of the cavity from half-distance between markers screwed in the ice (see section 6.2.1 for the uncertainty in closure rate) and from the difference between two Kinect point clouds (median, first and third quartile). b) Pressure measured by the load cells LC97_1 (upstream) and LC97_2 (downstream). Vertical lines indicate percentage of ice covering the load cells based on casual observations.The periods of melting are shaded in grey.

The peaks in pressure in the second cavity are short-lived and less intense. In this second cavity, the ice edge migrates more rapidly and closely to the bed topography (Fig. 6.5 and F.1, 15-16 Nov.). The upstream load cell LC97_1 records a peak 1.2 times higher than the local background pressure measured on 15 November (i.e. 0.83 MPa). The subsequent decrease occurs in less than 3 hours and pressure drops to a minimum of 0.47 MPa. For unknown reasons, the increase in pressure does not match the increase in percentage of ice coverage from visual observations and Kinect measurements. Unless the load cell is covered 100%, the load cell seems to measure only a fraction of the load. The peak at the downstream load cell LC97_2 is smaller than the one measured at load cell LC97_1, but comparable in shape. It reaches a maximum of 1.24 MPa and then decreases gently to a minimum of 1.14 MPa. The closure rate as measured by the Kinect and markers are in relatively good agreement except for the increase between 19:00 and 00:00 on 15 November. However, the rate computed from these early measurements is very uncertain because of the short time interval between the measurements (Tables F.3 and F.4). The uncertainty in the contraction rate for periods of one hour is about 12 cm.day^{-1} for both the Kinect and the marker data. Thus, theses changes in closure rate does not represent realistic changes. The rest of the closure rate estimates indicates instead a more steady contraction that varies between 25 and 30 cm.day^{-1}, which is ∼20 % faster contraction than during the first cavity.

The cavity geometry and increase in deformation are assumed to cause the different response in pressure and timing. The timing between the pressure peaks at LC97_1 and LC97_2 for each cavity indicates that the ice migrates from one load cell to the other in 25 hours for the first cavity and 32 hours for the second. The first cavity contracts faster over the load cells due to the overhang, although the measured closure rate is lower than the second cavity. The difference in closure rate may also express an increase in stress release from internal deformation of the ice and this leads to reduced stress on the bed and slower migration of the wall. Vertical flow of the roof in the second cavity (i.e. elliptical shape) dominates the creep closure compared to the first cavity. The faster contraction from the roof forced an early removal of the Kinect in the second cavity, which did not occur during the first one (i.e. high roof, semi-circular shape). The enhanced deformation is thus assumed to be mostly expressed through the vertical flow from the cavity roof. This stress release through deformation causes a decrease of the normal stress on the bedrock and may explain the low peak and the lack of exponential decay observed in the second cavity.

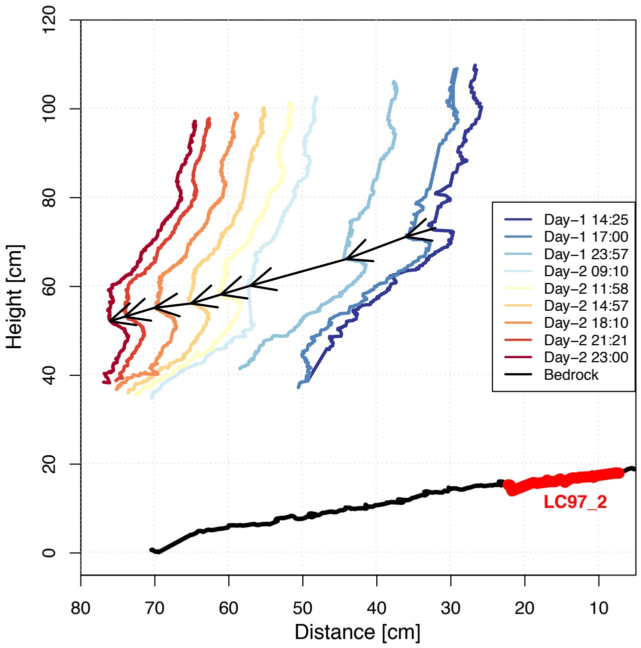

Figure 6.6: Displacement of the wall of the first cavity for the period 13-14 Nov. (Day 1 and 2). The cross-section is parallel to the sliding direction and passes over both load cells.

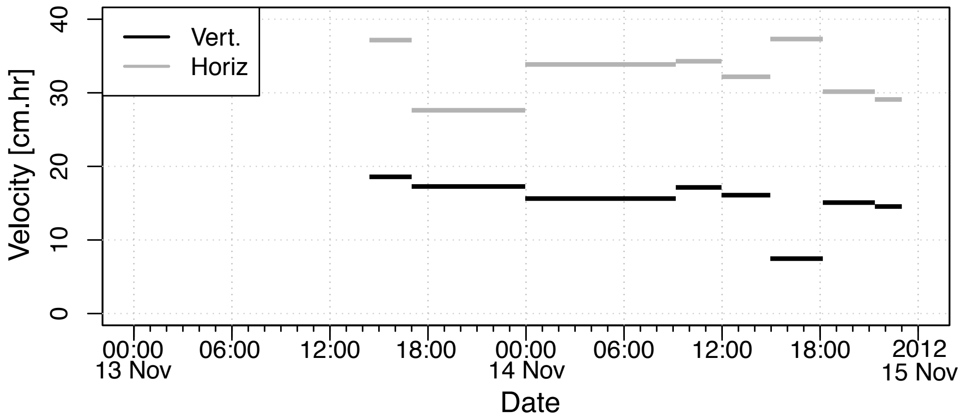

Figure 6.7: Vertical and horizontal closure rate from the point highlighted with a black arrow in figure 6.6 during the contraction of the first cavity (13-14 November 2012).

6.2.4 Experiment Conclusions

The pressure response during the contraction of the two cavities demonstrates that the stress bridging effect increases the normal stress at the load cells. The observed peaks show some variability in their shape. It is assumed to be due to the geometry of the cavity that affects ice deformation (i.e. stress relaxation) and thus the increase in normal stress on the bedrock. The contraction of the first cavity, that is approximately semi-circular, causes a high intensity pressure peak followed by an exponential pressure decay. This may be due to the presence of a small overhang located just above the load cells that increases the transfer of load to the edge of the cavity. The second cavity had a low roof and thus was more elliptical in shape than the first cavity. This geometry increases closure rate that dampens the intensity of the response and gives a broader peak in pressure.

The experiment demonstrates that the shape of the peak in pressure can be summarised as follows:

- A rise in pressure occurs between 4 and 6 hours after the ice regains contact with the load cells
- The subsequent peak in pressure varies in intensity but is twice or less the local background pressure when the edge of the cavity is in full contact with the load cell.
- During the migration of the cavity wall, the pressure decreases almost linearly for the small peaks in pressure measured at the downstream load cell and in the second

cavity (e.g elliptical shape). The decay in pressure becomes more exponential as the event intensity increases such as during the contraction of the first cavity (i.e. semi-circular shape).

In the next section, these observations are compared with a model of the contraction of a subglacial cavity.

6.3 Modelling Cavity Contraction

A full Stokes model is used to investigate the effect of stress bridging on the pressure response at the bed. The two dimensional model simulates the contraction of a subglacial cavity. Normal stress is averaged over an area representing the load cell plate as the cavity wall migrates over it and the result is compared with load cell observations. The aim is to reproduce the peak in pressure and characterise the effect of cavity geometry and sliding on the shape and intensity of the peak in pressure.

6.3.1 Model Equations

The model setup is a simplification of the experiment described in section 6.2. The contracting subglacial cavity is assumed to have its longest axis perpendicular to the sliding direction. Closure of the subglacial cavity is modelled, and the contact between ice and bedrock is investigated.

The governing laws of glacier flow are defined based on mass conservation and conservation of momentum. The mass conservation imposes a vanishing divergence of the velocity field $\boldsymbol{v}$ consisting of a vertical component u and a horizontal component v, is zero due to incompressibility of ice.

$$\nabla \cdot \boldsymbol{v} = 0, \quad \text{with } \boldsymbol{v}{=}(u, v)^{\mathrm{T}} \tag{6.1}$$

Ice flow is obtained from the Stokes equation assuming that acceleration in the fluid is negligible. The gravitational acceleration $\boldsymbol{g}$ and the density of ice ρ_{ice} (i.e. 900 kg m^{-3}) are related to the divergence of the deviatoric stress tensor $\boldsymbol{\tau}$ and the gradient in pressure p within the ice, by the following equation:

$$\nabla \cdot \boldsymbol{\tau} - \nabla p = \rho_{\text{ice}} \boldsymbol{g} \tag{6.2}$$

The rheology of the ice follows Glen's flow law assuming the ice is a viscous shear thinning material. The deviatoric stress tensor, $\boldsymbol{\tau}$ is obtained from the strain rate tensor, $\mathbf{D}$, and the second invariant of the strain rate tensor $\dot{\boldsymbol{\epsilon}}_{\boldsymbol{e}}$, such as:

$$\begin{aligned} \boldsymbol{\tau} &= 2\,\eta\mathbf{D} && (6.3)\\ \eta &= \frac{1}{2}A^{-1/n}\dot{\epsilon}_e^{(1-n)/n} \quad \text{with } \dot{\boldsymbol{\epsilon}}_{\boldsymbol{e}} = \sqrt{\mathrm{tr}(\mathbf{D}^2)/2} && (6.4) \end{aligned}$$

A defines a constant rate factor that depends on the properties of the ice. Assuming that the ice is temperate and isotropic, $A(T=0)$ is equal to 2.4×10^{-25} s^{-1} Pa^{-3} according to Cuffey and Paterson (2010).

The last equation to be solved is the free surface at the bed s, where is located the subglacial cavity. The free surface ignores the effect of refreezing and melting of the cavity walls and a height condition prevents downward flow of the ice when it has reached the bed. The cavity geometry is determined by the kinematic evolution defined for the free surface variable, s.

$$\frac{\partial s}{\partial t} + u\,\frac{\partial s}{\partial x} - v = 0 \qquad (6.5)$$

6.3.2 Boundary conditions

The model domain is a vertical ice slab with periodic lateral boundary conditions, and has a subglacial cavity at the glacier bed. The bottom boundary condition prevents penetration of the ice when the ice is in contact with the bed, such as $\boldsymbol{v}\cdot\boldsymbol{n}|_{\mathrm{bed}} = 0$, where $\boldsymbol{n}$ is the vector normal to the bed surface. The pressure in the empty cavity is equal to atmospheric pressure ($P_{atm} = 0$), which leads to the contraction of the cavity.

Only the part of the glacier close to the bed is modelled in order to reduce computation time and the overlying glacier thickness is accounted for by applying an external force at the top of the domain. The upper limit is set at a sufficient distance from the bedrock to avoid any effect of the upper boundary on the response at the bed. The value of the force p_{top} is computed so that the sum of this external force and the pressure of the modelled ice thickness equals the overburden pressure measured at the bed of Engabreen ($\sim$ 1.9 MPa). The external force as well as the body force of the ice can be rotated by an angle θ in order to simulate an inclined bed with angle θ.

6.3.3 Finite Element Discretisation

The model is solved numerically using the finite element method implemented in the software Elmer/Ice (Gagliardini et al., 2013).

The contraction of the channel is computed from the solution of Eqn (6.5), and the mesh geometry is updated at each time step (i.e. 10 min). The redistribution of the mesh-nodes is derived by solving a virtual linear elasticity problem.

No-penetration at the glacier bed $\boldsymbol{u} \cdot \boldsymbol{n}|_{\text{bed}} = 0$ is assumed when the ice is in contact with the bed such that $h_{ice} = h_{bed}$. This condition becomes $h_{ice} = 0$ as the height is computed relative to a flat bed.

6.3.4 Effect of Cavity Geometry

The first model investigates the effect of cavity geometry on the distribution and temporal variation in normal stress at the glacier bed. A semi-circular cavity and a semi-elliptical cavity, 2-metres wide, are modelled. The load cell is represented by a 15 cm line at the bed that is located at the edge of the subglacial cavity. The model domain is 8 m high and 2.5 m wide with a high mesh density of 4 cm spacing at the bottom boundary and 40 cm at the top of the domain (total of elements: 3272). The contraction of the cavity is simulated during 3 days at a time step of 10 minutes. The simulation is conducted with a reference model setup that has a flat bedrock, no slip condition at the glacier bed and the ice is assumed to flow as a non-Newtonian fluid (Glen's flow law exponent of 3).

A peak in normal stress about twice the overburden pressure is reproduced near the subglacial cavity for steady state conditions, where the model solves only for the Navier-Stokes equation (Fig. 6.8). The stress bridging effect is concentrated at the edge of the cavity and leads to a singularity. The effect rapidly vanishes in the first half-metre away from the channel and levels off to the lateral boundary of the domain. The difference between the two cavities is characterised by a faster decay in normal stress, a higher normal stress level at the lateral side of the domain and a >150% increase in closure rate for the semi-circular cavity. The vertical component of the closure rate dominates the contraction of the semi-elliptical cavity whereas it is more balanced for the semi-circular cavity. The horizontal closure rate in the latter still exceeds the vertical component at the ice wall.

The time variation in normal stress computed at the load cell shows the increase in normal stress and return to overburden pressure (Fig. 6.9), similar to the one observed in the experiment. The peak reaches nearly twice the overburden pressure: 3.8 MPa for the

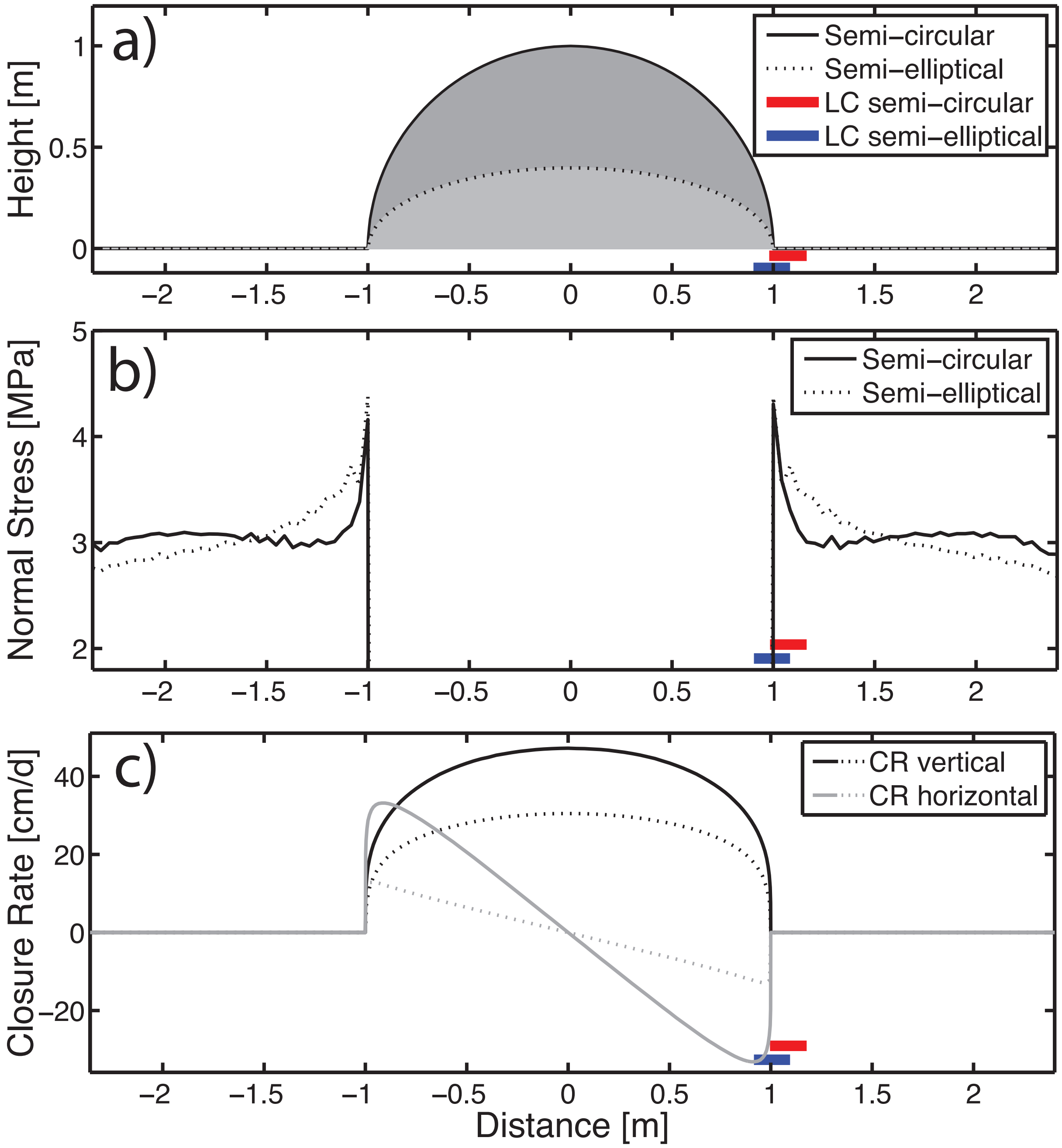

Figure 6.8: Stress bridging effect at the glacier bed for steady state conditions (where the model only solves for the Navier-Stokes equation) with a flat bed and a Glen's flow law exponent n of 3. a) Geometry of the semi-elliptical and semi-circular cavities with the location of the load cell as defined in the model. b) Distribution of normal stress at the glacier bed. c) Vertical and horizontal component of closure rate. Ice flow is positive to the right.

semi-elliptical cavity and 4.2 MPa for the semi-circular cavity. The shape of the decay is however less steep, it takes days to return to overburden pressure. The semi-elliptical cavity closes in ∼2.5 days and it takes longer than 3 days for the semi-circular cavity. This may be a response to the different area of the cavity despite faster closure rate for the semi-circular one. The decrease in normal stress for the semi-elliptical cavity appears also linear instead of the expected exponential decrease as seen in the observations and the semi-circular case.

The cavity geometry is proved to have an important effect on the normal stress response at the load cell. A more circular geometry of the cavity enhances faster closure rate and migration over the load cell. However, the timing of the response is too slow and does not fit the timing extracted from the observations.

6.3.5 Effect of Bed Slope and Sliding

This second experiment examines the role of bed slope and sliding on the temporal variation in normal stress. A bed slope of 7° is prescribed and the averaged normal stress representing the load cell is computed at the upstream side of the cavity like during the experiment (Lappegard, 2006b). The bed slope causes the peak in pressure to increase slightly in intensity and to occur earlier for both modelled geometry (Fig. 6.9). The closure rate distribution becomes asymmetric compared to figure 6.8 and enhances the contraction of the ice wall above the load cell.

A slip condition based on Weertman's sliding law is applied at the glacier bed through a slip coefficient (Weertman, 1957). The bed stays horizontally aligned in this test in order to separate the effect of sliding from the effect of slope. Sliding favours a more dynamic response in normal stress at the load cell (Fig. 6.9). The normal stress peaks earlier and decays more rapidly. The maximum attained pressure is also lower (i.e. 3.5 MPa). An inspection of the closure rate reveals a doubling of the horizontal component for the semi-circular cavity. The increase is more modest for the semi-elliptical one. The free slip condition enhances velocity tangent to the glacier bed, which relaxes more efficiently stresses in the ice and also explain the decrease in intensity of the peak in pressure.

The bed slope and sliding cause the peak and decay in normal stress to occur earlier and faster, although the evolution in normal stress is still much slower than the observations in the experiment (section 6.2).

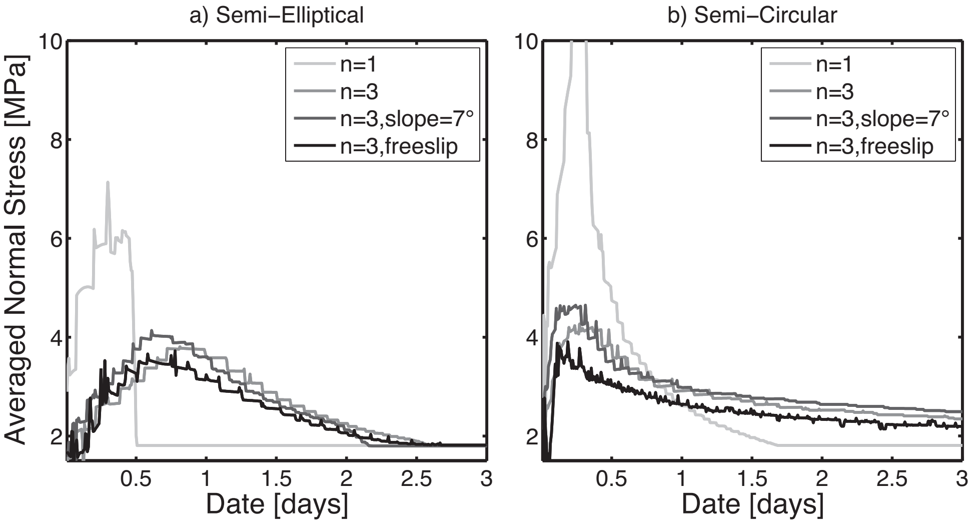

Figure 6.9: Temporal variation in normal stress averaged over the 15 cm line representing the load cell plate (Fig. 6.8). a) Response in normal stress during the contraction of a 2-metre wide semi-elliptical cavity for different conditions (ref. legend). b) Same as a), but for a semi-circular cavity.

6.3.6 Effect of Linear Rheology

The last experiment explores the possibility that ice rheology and a variation in Glen's flow law exponent n may explain the rapidity of the response in normal stress. The ice is generally considered as a non-Newtonian shear thinning fluid, $n = 3$, however observations at the Svartisen Subglacial Laboratory indicate that the ice may behave like a Newtonian material with $n = 1$ (Cohen, 2000; Lappegard, 2006b).

The 'diagnostic' result from this model shows that the exponent homogenises the response in normal stress between the two tested geometries of cavities (Fig. 6.10). The peaks in normal stress are 4-6 times greater than the overburden pressure. The semi-circular cavity has a lower maximum normal stress accompanied by enhanced horizontal closure rate. The vertical flow becomes more uniform with an exponent of 1 as the deformation increases in low shear stress area (< 100 kPa), and especially above the cavity where shear stresses range from 0 to 400 kPa.

The effect of a linear rheology also causes a high peak in normal stress and nearly immediate decay as the cavity contracts over the simulated load cell (Fig. 6.9). The vertical component of the closure rate controls the normal stress response. It leads to a roof collapse in the semi-elliptical cavity, which explains the sudden drop in normal stress. A test with different width of cavities from 25 cm to 2 m show that their closure

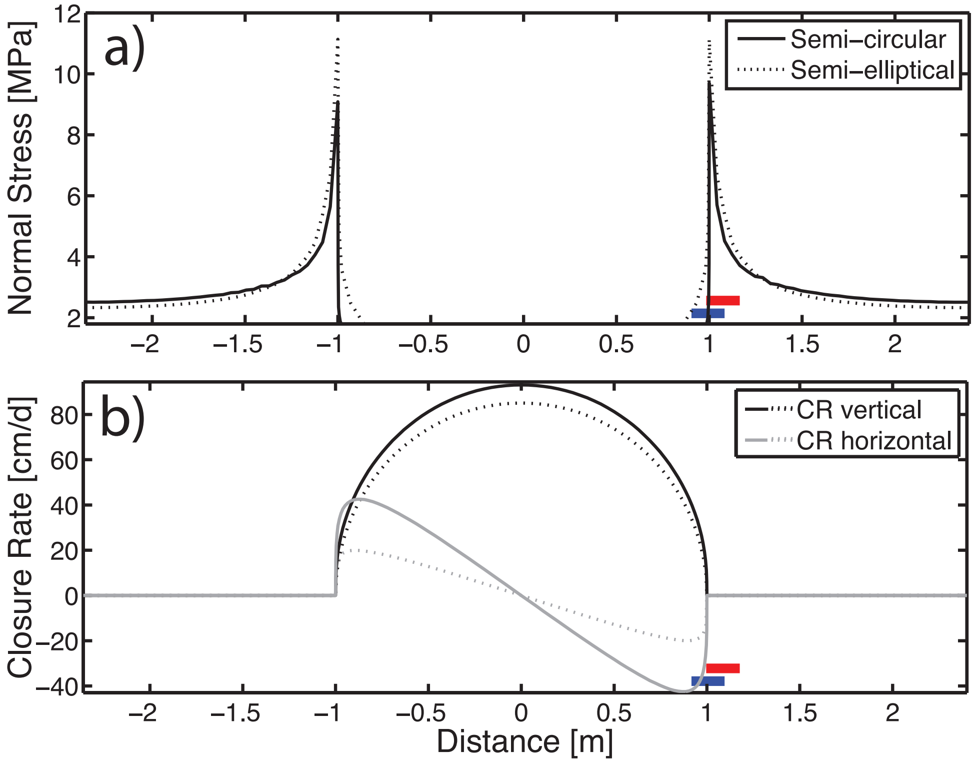

Figure 6.10: a) Distribution of normal stress at the bed for same condition as in figure 6.8, but with $n = 1$. b) Vertical and horizontal component of closure rate.

is all synchronous, indicating the dominance of the vertical flow for a cavity with a given height-width ratio. The contraction of the semi-circular cavity also shows that the time evolution of the vertical closure rate becomes linear compared to the earlier runs.

It is perhaps possible that the lower part of the glacier may deform at lower shear stresses and accelerate stress relaxation near the bed.

6.4 Discussion

The analysis of normal stress at the load cell in the model shows that the velocity of the ice wall migration and stress relaxation through ice creep controls the shape of the peak in pressure. This probably explains the different responses observed during the experiment.

Three factors can cause a more rapid migration of the cavity as expressed by an increase in the horizontal component of the closure rate. 1) The horizontal ice flow at the glacier bed increases as the cavity ceiling becomes higher relative to its width (Fig. 6.8). The migration of the ice wall is more rapid in the semi-circular than in the semi-elliptical cavity perhaps due to a more efficient transfer of the shear stress to the margin of the cavity. 2) A steeper bed and sliding enhances the horizontal closure rate on the upstream side of the cavity. The stress bridging effect is thus rapidly progressing downstream, which leads to a narrower peak in normal stress over time. 3) A change in ice rheology assuming a lower Glen's flow law exponent ($n = 1$) leads to a speed up of the closure of the cavity as deformation is enhanced at lower shear stress and above the cavity. This accelerates the return to the overburden pressure as the complete closure of the cavity occurs. However, the increased downward flow provokes a not-observed climb in normal stress that reaches 4 to 6 times the overburden.

The stress relaxation affects another part of the signal that is the intensity in the peak in pressure. As mentioned above, the change from a Non-Newtonian to a Newtonian rheology of the ice leads to a dramatic increase in normal stress. The building up in normal stress may be a result of the acceleration in vertical ice flow that presses down on the bed (Fig. 6.10. In this situation, stress bridging concentrates normal stress on a narrower area near the ice wall and boost the normal stress response at the simulated load cell. A more modest increase in normal stress is modelled at the upstream load cell in the simulation with an inclined bed. The bed slope modulates the compression in ice flow at the edge of the cavity. In contrast, sliding favours on the same scale as the result of the slope effect a stress relaxation at the glacier bed. Velocity tangent to the bed distributes the shear stress away form the cavity and decrease the magnitude of the peak in pressure.

The output of the model is directly relevant to the experiment and shows that sliding and the bed slope controls a part of the steepness and return in the peak in normal stress. The shape of the cavity explains the slower migration in the second cave that have a more elliptical shape and thus experience a slower migration of the ice wall. This lessened contraction broadened the peak in pressure as seen in this second cave. Furthermore, the semi-elliptical shape linearises the decay in pressure as shown in figure 6.9. This result is coherent with the normal stress signal from the second cavity (i.e. second part of the experiment) that shows a more linear decay after the peak in normal stress. The peak in intensity is however too variable to be able through the model results. Observations of normal stress at the Svartisen Subglacial Laboratory and Bondhusbreen show that the stress level is also influenced by the surrounding environment and effect of rock/boulders on pressure.

6.5 Summary

This chapter identified peaks in pressure from observations of normal stress at the Svartisen Subglacial Laboratory. The experiment of contraction of a subglacial cavity over the load cells show that this peak is reproducible. Measurements of closure rate from markers and a short range LiDAR helped explaining the variability of the peaks in pressure. Because the closure rate was stable, it is possible to attributes the variation in peak to the geometry of the cavity. The full Stokes model simulates a contracting cavity and the normal stress is averaged on the side of the cavity to reproduce the response in normal stress from the load cells. The temporal variation in normal stress is controlled by cavity geometry, slope, sliding and ice rheology. The strongest effect is seen from a change in shape of the subglacial cavity and ice rheology (Weertman, 1972). This analysis is coherent with the experiment output. As in the second cavity of the experiment, a semi-elliptical cavity dampens normal stress at the bed and shows a linear decay in normal stress. A semi-circular cavity instead leads to an increase in shear stress transfer and a stronger closure rate in the horizontal direction. The conclusion is that stress bridging explains the observations from the load cells. This effect causes concentration of stress near low-pressure cavities and can isolate the cavity from its surroundings.

Chapter 7
Conclusions

Monitoring cavity closure

Mathieu Tachon

7 Conclusions

This thesis investigates the relationship between stress at the glacier bed and changes in subglacial hydrology. It demonstrates the importance of mechanical processes such as stress bridging and load transfer, especially for the unconnected drainage system. Understanding the unconnected system is crucial as a reduction of its extent and sensitivity is believed to cause seasonal slow-down in the Greenland Ice-sheet (Andrews et al., 2014). It is a challenge to place direct observations of basal pressure in the context of glacier hydrology literature due to the unique location of the load cells. Nonetheless, this thesis is the first complete description of the processes that control variations in pressure in the unconnected drainage system.

Cause of Pressure Events

Daily pressure events are used to characterise the response of the unconnected drainage system. Characteristics of the pressure events identify how changes in the hydrological system cause pressure events at the glacier bed, as summarised in Chapter 4. As described by Lappegard et al. (2006), the pressurisation of the drainage system triggers the pressure events that leads to a pressure drop and then further decrease to a minimum. This minimum in pressure occurs when the capacity of the drainage system is able to accommodate meltwater input from the glacier surface. These basal observations indicate that the amplitude of the drop in pressure can be used to quantify the capacity of the drainage system, a variable that is usually only estimated qualitatively (Harper et al., 2007; Bartholomaus et al., 2008) or modelled (Schoof, 2010; Werder et al., 2013).

Although it is assumed that pressure events are caused by hydrological changes, the effect of basal sliding on normal stress is still uncertain. Glacier sliding could cause a similar decrease in normal stress on the lee-side of bumps (Iken and Bindschadler, 1986). A better mapping of the bedrock near the load cells, as done in Chapter 5, in combination with a higher order ice flow model could characterise the effect of sliding on normal stress at each load cell (Gagliardini et al., 2007). This would aid in the identification of the trigger of pressure events.

Pressure Events and Closure of the Drainage System

Daily pressure events are triggered by the hydrological system, but also respond to the closure of the drainage system as shown by a peak and decay in pressure. The magnitude of the peak in pressure appears to be directly linked to the amplitude of the previous drop in pressure. The intensity of the peak is thus related to the capacity of the drainage system too, although it is caused by the contraction and not the opening of the drainage system (Lappegard, 2006b, Paper III). The stress bridging effect near low pressure cavities causes the peak in pressure that reaches values much greater than the overburden pressure, as predicted by Weertman (1972). The experiment and modelling of stress bridging in Chapter 6 show that the geometry of subglacial cavities and sliding affects the intensity and shape of the peak in pressure. The shape of the peak can therefore be used to assess the extent and volume of the contracting drainage system. A statistical analysis of the load cell data also suggests that the greater the intensity of the peak in pressure, the larger the capacity of the drainage system. This explains why the largest peaks in pressure occur in spring and autumn, when variations in melt input are large. In summer, a more developed drainage system leads to a dampening of the amplitude of the peak. Although these interpretations are in good agreement with generally accepted theory of the development of the subglacial drainage system (Fountain and Walder, 1998), the direct observations present a completely new aspect of glacier hydrology, where the effect of the contraction of the drainage system on pressure is directly measured.

A secondary effect of stress bridging is that the increase in normal stress enhances ice deformation at the glacier bed and may cause a sealing of low-pressure channels (Lappegard et al., 2006). This sealing effect isolates channels and increases storage of water at the glacier bed. This concept contradicts accepted theory that low-pressure channels drain water from the distributed drainage system as inferred from measurements of water pressure in boreholes (Hubbard et al., 1995). Current models of subglacial hydrology do not account for this effect (Schoof, 2010; Werder et al., 2013), which reduces storage of subglacial water in the distributed drainage system. This directly affects the glacier dynamics by changing the effective pressure at the glacier bed. The direct observations reveal the effect of higher order stresses at the glacier bed, that are not addressed in hydrological models. The models could account for this sealing effect by simply reducing the porosity of the distributed drainage system near low-pressure channels and making this reduction proportional to the channel size.

Pressure Response during Spring Melt Events

The glacier bed experiences rapid changes during spring melt events as meltwater is routed to the subglacial system, sliding increases, and decoupling occurs at the ice-bedrock interface (Harper et al., 2007). Chapter 4 examines pressure recorded by load cells for nearly 20 spring melt events and identifies two types of subglacial dynamics based on the length of the event and levels of connectivity. The load cell observations reveal processes that previously have received little attention. The first type of event is characterised as ”simple bed response”, where the glacier bed adapts very rapidly to melt and load cells record a single pressure event. This pressure response is a consequence of rapid surface melt that leads to flooding or decoupling at the glacier bed. It is defined by an increase in spatial connectivity at the glacier bed (Lefeuvre et al., 2015). In contrast, the second type of spring melt event is ”complex”. Pressure at the glacier bed shows multiple irregular fluctuations and hydraulic connections at several load cells, identified by them having equal pressure. Both types of events, although different in response, terminate with a strong peak in pressure that indicates the closure of the drainage system.

The load cell observations differ to measurements of water pressure in boreholes. During spring melt events, water in boreholes generally becomes connected to an efficient drainage system and then exhibits daily pressure fluctuations during the rest of the melt season. Instead of presenting an increase in connection and activity, the load cells show a damped response after the subglacial drainage system has accommodated the first input of meltwater. The observations from load cells and boreholes are not contradictory; instead they complement each other and help characterise the mechanical and hydrological dynamics occurring at the glacier bed.

Load Transfer

Load transfer is defined as a mechanical transfer of the load of the ice from a pressurised drainage system to an unconnected drainage system (Paper II). This transfer is identified in load cell records of pressure as an anti-correlated signal between a load cell located in a channel and one in the unconnected drainage system. A thorough description of the timing and intensity between the forcing (i.e. pressurised channel) and response (i.e. unconnected system) is used to validate a model that reproduces this effect. Despite the simplicity of the model, the compression occurring during pressurisation creates an anti-correlated pressure signal between the channel and the rest of the glacier bed. This confirms that the load cells primarily measure pressure in the unconnected drainage system.

Importance of Direct Observations at the Glacier Bed

Direct observations from the Svartisen Subglacial Laboratory have led to a better understanding of the role of subglacial hydrology and mechanical processes in controlling variations in pressure at the glacier bed. Subglacial processes such as load transfer and stress bridging are shown to transmit the pressure response of the drainage system to hydrologically isolated or unconnected parts of the glacier bed. This transfer is important for propagating the effect of pressurisation of the drainage system to the rest of the glacier. It may also cause a dampening effect if the transfer in pressure is restrained. The observations from load cells, which have a fixed location at the glacier bed, were crucial in identifying the temporal and spatial variability in pressure and led to unique measurements of these mechanical processes. Future work needs to continue the description of the pressure response in order to quantify variations in the capacity of the drainage system. This is critical in order to assess the effect of subglacial processes on glacier dynamics.

References

Anandakrishnan S and Alley R (1997) Tidal forcing of basal seismicity of ice stream C, West Antarctica, observed far inland. *Journal of Geophysical Research-Solid Earth*, **102**(B7), 15183–15196

Anderson RS, Hallet B, Walder JS and Aubry BF (1982) Observations in a cavity beneath Grinnell Glacier. *Earth Surface Processes and Landforms*, **7**(1), 63–70

Andreassen LM, Winsvold SH, Paul F and Hausberg JE (2012) Inventory of Norwegian glaciers. Technical Report 38, Norwegian Water Resources and Energy Directorate (NVE), Oslo, Norway

Andreassen LM, Huss M, Melvold K, Elvehøy H and Winsvold SH (2015) Ice thickness measurements and volume estimates for glaciers in Norway

Andrews LC, Catania GA, Hoffman MJ, Gulley JD, Lüthi MP, Ryser C, Hawley RL and Neumann TA (2014) Direct observations of evolving subglacial drainage beneath the Greenland Ice Sheet. *Nature*, **514**(7520), 80–83

Bachrach A, Prentice S, He R, Henry P, Huang AS, Krainin M, Maturana D, Fox D and Roy N (2012) Estimation, planning, and mapping for autonomous flight using an RGB-D camera in GPS-denied environments. *The International Journal of Robotics Research*, **31**(11), 1320–1343

Bartholomaus TC, Anderson RS and Anderson SP (2008) Response of glacier basal motion to transient water storage. *Nature Geoscience*, **1**(1), 33–37

Bartholomew ID, Nienow PW, Mair DWF, Hubbard AL, King MA and Sole AJ (2010) Seasonal evolution of subglacial drainage and acceleration in a Greenland outlet glacier. *Nature Geoscience*, **3**(6), 408–411

Bartholomew ID, Nienow PW, Sole AJ, Mair DWF, Cowton TR and King MA (2012) Short-term variability in Greenland Ice Sheet motion forced by time-varying meltwater drainage: Implications for the relationship between subglacial drainage system behavior and ice velocity. *Journal of Geophysical Research*, **117**(F3), F03002

Beaud F, Flowers GE and Pimentel S (2014) Seasonal-scale abrasion and quarrying patterns from a two-dimensional ice-flow model coupled to distributed and channelized subglacial drainage. *Geomorphology*, **219**, 176–191

Benn DI and Evans DJA (2010) *Glaciers and Glaciation.* Hodder Education, London, second edition

Bennett RG (1968) Frost Shatter and Glacial Erosion under the margins of Østerdalsisen, Svartisen. *Norsk Geografisk Tidsskrift-Norwegian Journal of Geography*, **22**(3), 209–213

Blythe DS, Duling DV and Gibson DE (2014) Developing a hot-water drill system for the WISSARD project: 2. In situ water production. *Annals of Glaciology*, **55**(68), 298–302

Bonnal EP (2011) *3D Mapping of indoor environments using RGB-D Kinect camera for robotic mobile application.* Master's thesis, Politecnico di Torino, Department of Control and Computer Engineering

Boulton GS and Hindmarsh RCA (1987) Sediment deformation beneath glaciers: rheology and geological consequences. *Journal of Geophysical Research*, **92**(B9), 9059–9082

Boulton GS and Jones AS (1979) Stability of temperate ice caps and ice sheets resting on beds of deformable sediment. *Journal of Glaciology*, **24**(90), 29–43

Boulton GS, Morris EM, Armstrong AA and Thomas A (1979) Direct measurement of stress at the base of a glacier. *Journal of Glaciology*, **22**(86), 3–24

Budd WF and Jacka TH (1989) A review of ice rheology for ice sheet modelling. *Cold Regions Science and Technology*, **16**(2), 107–144

Carol H (1947) The formation of roches moutonnées. *Journal of Glaciology*, **1**, 57–59

Caviedes-Voullième D, Juez C and Murillo J (2014) 2D dry granular free-surface flow over complex topography with obstacles. Part I: experimental study using a consumer-grade RGB-D sensor. *Computers & Geosciences*, **73**, 177–197

Chandler D, Wadham JL, Lis GP, Cowton TR, Sole AJ, Bartholomew ID, Telling J, Nienow PW, Bagshaw EB, Mair DWF, Vinen S and Hubbard AL (2013) Evolution of the subglacial drainage system beneath the Greenland Ice Sheet revealed by tracers. *Nature Geoscience*, **6**(3), 195–198

Chinn TJH, Winkler S, Salinger MJ and Haakensen N (2005) Recent glacier advances in Norway and New Zealand: a comparison of their glaciological and meteorological causes. *Geografiska Annaler. Series A, Physical Geography*, **87**(1), 141–157

Clarke GKC (2005) Subglacial processes. *Annual Review of Earth and Planetary Sciences*, **33**(1), 247–276

Cohen D (2000) Rheology of ice at the bed of Engabreen, Norway. *Journal of Glaciology*, **46**(155), 611–621

Cohen D, Hooke RL, Iverson NR and Kohler J (2000) Sliding of ice past an obstacle at Engabreen, Norway. *Journal of Glaciology*, **46**(155), 599–610

Cohen D, Iverson NR, Hooyer TS, Fischer UH, Jackson M and Moore PL (2005) Debris-bed friction of hard-bedded glaciers. *Journal of Geophysical Research*, **110**(F2), F02007

Cohen D, Hooyer TS, Iverson NR, Thomason JF and Jackson M (2006) Role of transient water pressure in quarrying: A subglacial experiment using acoustic emissions. *Journal of Geophysical Research*, **111**(F3), F03006

Cuffey KM and Paterson WSB (2010) *The Physics of Glaciers*. Elsevier, fourth edition

Cuffey KM, Raymond CF, Conway H, Hallet B and Gades AM (1999) Interfacial water in polar glaciers and glacier sliding at -17 °C. *Geophysical Research Letters*, **26**(6), 751–754

Cuffey KM, Conway H, Gades AM, Hallet B, Lorrain R, Severinghaus JP, Steig EJ, Vaughn BH and White J (2000) Entrainment at cold glacier beds. *Geology*, **28**(4), 351–354

DiBiagio E (2003) A case study of vibrating-wire sensors that have vibrated continuously for 27 years. In *6th International Symposium on Field Measurements in GeoMechanics*, 1–15, NGI, Taylor &amp; Francis, Oslo, Norway

Doliotis P, Stefan A, McMurrough C, Eckhard D and Athitsos V (2011) Comparing gesture recognition accuracy using color and depth information. In *the 4th International Conference*, 1–20, ACM, New York, New York, USA

Dunse T, Schellenberger T, Hagen JO, Kääb A, Schuler TV and Reijmer CH (2015) Glacier-surge mechanisms promoted by a hydro-thermodynamic feedback to summer melt. *The Cryosphere*, **9**(1), 197–215

Echelmeyer K and Zhongxiang W (1987) Direct observation of basal sliding and deformation of basal drift at sub-freezing temperatures. *Journal of Glaciology*, **33**(113), 83–98

Fitzsimons SJ, Lorrain RD and Vandergoes MJ (2000) Behaviour of subglacial sediment and basal ice in a cold glacier. *Geological Society, London, Special Publications*, **176**(1), 181–190

Fitzsimons SJ, McManus KJ, Sirota P and Lorrain RD (2001) Direct shear tests of materials from a cold glacier: implications for landform development. *Quaternary International*, **86**(1), 129–137

Flowers GE (2015) Modelling water flow under glaciers and ice sheets. *Proceedings of the Royal Society of London A: Mathematical, Physical and Engineering Sciences*, **471**(2176), 20140907

Fountain AG and Walder JS (1998) Water flow through temperate glaciers. *Reviews of Geophysics*, **36**(3), 299–328

Fudge TJ, Humphrey NF, Harper JT and Pfeffer WT (2008) Diurnal fluctuations in borehole water levels: configuration of the drainage system beneath Bench Glacier, Alaska, USA. *Journal of Glaciology*, **54**(185), 297–306

Furukawa Y and Ponce J (2010) Accurate, Dense, and Robust Multiview Stereopsis. *Pattern Analysis and Machine Intelligence, IEEE Transactions on*, **32**(8), 1362–1376

Gagliardini O, Cohen D, Råback P and Zwinger T (2007) Finite-element modeling of subglacial cavities and related friction law. *Journal of Geophysical Research*, **112**(F2), F02027

Gagliardini O, Zwinger T, Gillet-Chaulet F, Durand G, Favier L, De Fleurian B, Greve R, Malinen M, Martín C, Råback P, Ruokolainen J, Sacchettini M, Schäfer M, Seddik H and Thies J (2013) Capabilities and performance of Elmer/Ice, a new-generation ice sheet model. *Geoscientific Model Development*, **6**(4), 1299–1318

Gerrard JAF, Perutz MF and Roch A (1952) Measurement of the Velocity Distribution along a Vertical Line through a Glacier. *Proceedings of the Royal Society A: Mathematical, Physical and Engineering Sciences*, **213**(1115), 546–558

Glen JW (1952) Experiments on the deformation of ice. *Journal of Glaciology*, **2**(12), 111–114

Glen JW (1955) The Creep of Polycrystalline Ice. *Proceedings of the Royal Society A: Mathematical, Physical and Engineering Sciences*, **228**(1175), 519–538

Glen JW (1956) Measurement of the deformation of ice in a tunnel at the foot of an ice fall. *Journal of Glaciology*, **2**(20), 735–746

Goodman DJ, King G, Millar D and Robin GQ (1979) Pressure melting effects in basal ice of temperate glaciers: laboratory studies and field observations under glacier d'Argentière. *Journal of Glaciology*, **23**(89), 259–271

Gordon S, Sharp MJ, Hubbard BP, Smart C, Ketterling B and Willis IC (1998) Seasonal reorganization of subglacial drainage inferred from measurements in boreholes. *Hydrological Processes*, **12**(1), 105–133

Gordon S, Sharp MJ, Hubbard BP, Willis IC, Smart C, Copland L, Harbor JM and Ketterling B (2001) Borehole drainage and its implications for the investigation of glacier hydrology: experiences from Haut Glacier d'Arolla, Switzerland. *Hydrological Processes*, **15**(5), 797–813

Gulley JD, Walthard P, Martin J and Banwell AF (2012) Conduit roughness and dye-trace breakthrough curves: why slow velocity and high dispersivity may not reflect flow in distributed systems. *Journal of Glaciology*, **58**(211), 915–925

Gulley JD, Spellman PD, Covington MD, Martin JB, Benn DI and Catania GA (2014) Large values of hydraulic roughness in subglacial conduits during conduit enlargement: implications for modeling conduit evolution. *Earth Surface Processes and Landforms*, **39**(3), 296–310

Haefeli R (1951) Some observations on glacier flow. *Journal of Glaciology*, **1**(9), 496–500

Haefeli R (1952) Observations on the quasi-viscous behaviour of ice in a tunnel in the Z'mutt glacier. *Journal of Glaciology*, **2**(12), 94–99

Hagen JO, Wold B, Liestøl O, Østrem G and Sollid JL (1983) Subglacial processes at Bondhusbreen, Norway: preliminary results. *Annals of Glaciology*, **4**(3), 91–98

Hagen JO, Liestøl O, Sollid JL, Wold B and Østrem G (1993) Subglacial investigations at Bondhusbreen, Folgefonni, Norway. *Norsk Geografisk Tidsskrift-Norwegian Journal of Geography*, **47**(3), 117–162

Hallet B, Lorrain R and Souchez RA (1978) The composition of basal ice from a glacier sliding over limestones. *Geological Society of America Bulletin*, **89**(2), 314–320

Hammerle M, Hofle B, Fuchs J, Schroder-Ritzrau A, Vollweiler N and Frank N (2014) Comparison of Kinect and Terrestrial LiDAR Capturing Natural Karst Cave 3-D Objects. *Geoscience and Remote Sensing Letters, IEEE*, **11**(11), 1896–1900

Han J, Shao L, Xu D and Shotton J (2013) Enhanced Computer Vision With Microsoft Kinect Sensor: A Review. *Ieee Transactions on Cybernetics*, **43**(5), 1318–1334

Harper JT, Humphrey NF and Pfeffer WT (2005) Evolution of subglacial water pressure along a glacier's length. *Annals of Glaciology*, **40**(1), 31–36

Harper JT, Humphrey NF, Pfeffer WT and Lazar B (2007) Two modes of accelerated glacier sliding related to water. *Geophysical Research Letters*, **34**(12), L12503

Harper JT, Bradford JH, Humphrey NF and Meierbachtol TW (2010) Vertical extension of the subglacial drainage system into basal crevasses. *Nature*, **467**(7315), 579–582

Helmstetter A, Nicolas B, Comon P and Gay M (2015) Basal icequakes recorded beneath an Alpine glacier (Glacier d'Argentière, Mont Blanc, France): Evidence for stick-slip motion? *Journal Of Geophysical Research-Earth Surface*, **120**(3), 379–401

Henry P, Krainin M, Herbst E, Ren X and Fox D (2010) RGB-D Mapping: Using depth cameras for dense 3D modeling of indoor environments. In *Proceedings of International Symposium on Experimental Robotics ISER, Delhi, India, December*, 477–491, Springer Berlin Heidelberg

Henry P, Krainin M, Herbst E, Ren X and Fox D (2012) RGB-D mapping: Using Kinect-style depth cameras for dense 3D modeling of indoor environments. *The International Journal of Robotics Research*, **31**(5), 647–663

Hewitt IJ (2011) Modelling distributed and channelized subglacial drainage: the spacing of channels. *Journal of Glaciology*, **57**(202), 302–314

Hoffman MJ and Price S (2014) Feedbacks between coupled subglacial hydrology and glacier dynamics. *Journal Of Geophysical Research-Earth Surface*, **119**(3), 414–436

Holdsworth G (1974) Meserve glacier Wright Valley, Antarctica: Part II. Basal Processes. Technical report

Holdsworth G and Bull C (1970) The flow law of cold ice: investigations on Meserve Glacier, Antarctica. *International Association of Hydrological Sciences*

Hooke RL, Laumann T and Kohler J (1990) Subglacial water pressures and the shape of subglacial conduits. *Journal of Glaciology*, **36**(122), 67–71

Hubbard BP (2002) Direct measurement of basal motion at a hard-bedded, temperate glacier: Glacier de Tsanfleuron, Switzerland. *Journal of Glaciology*, **48**(160), 1–8

Hubbard BP, Sharp MJ, Willis IC, Nielsen MK and Smart CC (1995) Borehole water-level variations and the structure of the subglacial hydrological system of Haut Glacier d'Arolla, Valais, Switzerland. *Journal of Glaciology*, **41**(139), 572–583

Iken A and Bindschadler RA (1986) Combined measurements of subglacial water-pressure and surface velocity of Findelengletscher, Switzerland - Conclusions about drainage system and sliding mechanism. *Journal of Glaciology*, **32**(110), 101–119

Iken A and Truffer M (1997) The relationship between subglacial water pressure and velocity of Findelengletscher, Switzerland, during its advance and retreat. *Journal of Glaciology*, **43**(144), 328–338

IPCC (2013) *Climate change 2013: The Physical Science Basis. Contribution of Working Group I to the Fifth Assessment Report of the Intergovernmental Panel on Climate Change*. Cambridge University Press, Cambridge, United Kingdom and New York, NY, USA

Iverson NR (1991) Morphology of glacial striae: Implications for abrasion of glacier beds and fault surfaces. *Geological Society of America Bulletin*, **103**(10), 1308–1316

Iverson NR, Hooyer TS and Baker RW (1998) Ring-shear studies of till deformation: Coulomb-plastic behavior and distributed strain in glacier beds. *Journal of Glaciology*, **44**(148), 634–642

Iverson NR, Cohen D, Hooyer TS, Fischer UH, Jackson M, Moore PL, Lappegard G and Kohler J (2003) Effects of Basal Debris on Glacier Flow. *Science*, **301**(5629), 81–84

Iverson NR, Hooyer TS, Fischer UH, Cohen D, Moore PL, Jackson M, Lappegard G and Kohler J (2007) Soft-bed experiments beneath Engabreen, Norway: regelation infiltration, basal slip and bed deformation. *Journal of Glaciology*, **53**(182), 323–340

Izadi S, Kim D, Hilliges O and Molyneaux D (2011) KinectFusion: real-time 3D reconstruction and interaction using a moving depth camera. In *Proceedings of ACM Symposium on User Interface Software and Technology, Santa Barbara, CA, USA, 16–19 October 2011*, 559, ACM Press, New York, USA

Jackson M, Brown I and Elvehøy H (2005) Velocity measurements on Engabreen, Norway. *Annals of Glaciology*, **42**(1), 29–34

Jansson P, Kohler J and Pohjola VA (1996) Characteristics of basal ice at Engabreen, northern Norway. *Annals of Glaciology*, **22**, 114–120

Kääb A, Girod L and Berthling I (2014) Surface kinematics of periglacial sorted circles using structure-from-motion technology. *The Cryosphere*, **8**(3), 1041–1056

Kamb BW and LaChapelle E (1964) Direct observation of the mechanism of glacier sliding over bedrock. *Journal of Glaciology*, **5**(38), 159–172

Kennett M, Laumann T and Lund C (1993) Helicopter-borne radio-echo sounding of Svartisen, Norway. *Annals of Glaciology*, **17**, 23–26

Khoshelham K and Elberink SO (2012) Accuracy and Resolution of Kinect Depth Data for Indoor Mapping Applications. *Sensors*, **12**(2), 1437–1454

Kjøllmoen B, Andreassen LM, Elvehøy H, Jackson M and Giesen RH (2011) Glaciological investigations in Norway in 2010. Technical Report 3, Norwegian Water Resources and Energy Directorate (NVE), Oslo, Norway

Kohler J (1998) The effect of subglacial intakes on ice dynamics at Engabreen. Technical Report 12, Norwegian Water Resources and Energy Directorate (NVE)

Lai K, Bo L, Ren X and Fox D (2011) A large-scale hierarchical multi-view RGB-D object dataset. In *2011 IEEE International Conference on Robotics and Automation (ICRA)*, 1817–1824, IEEE

Lappegard G (2006a) *Basal hydraulics of hard-bedded glaciers: Observations and theory related to Engabreen, Norway*. Ph.D. thesis, University of Oslo, University of Oslo

Lappegard G (2006b) *Paper III: Subglacial stress bridging around low-pressure channels (unpublished)*. Ph.D. thesis, University of Oslo

Lappegard G and Kohler J (2005) Determination of basal hydraulic systems based on subglacial high-pressure pump experiments. *Annals of Glaciology*, **40**(1), 37–42

Lappegard G, Kohler J, Jackson M and Hagen JO (2006) Characteristics of subglacial drainage systems deduced from load-cell measurements. *Journal of Glaciology*, **52**(176), 137–148

Lefeuvre PM, Jackson M, Lappegard G and Hagen JO (2015) Interannual variability of glacier basal pressure from a 20 year record. *Annals of Glaciology*, **56**(70), 33–44

Lliboutry L (1968) General theory of subglacial cavitation and sliding of temperate glaciers. *Journal of Glaciology*, **7**(49), 21–58

Lliboutry L (1976) Physical processes in temperate glaciers. *Journal of Glaciology*, **16**(74), 151–158

Lowe DG (2004) Distinctive image features from scale-invariant keypoints. *International Journal of Computer Vision*, **60**(2), 91–110

Mankoff KD and Gulley JD (2012) Small scale high resolution LiDAR measurements of a subglacial conduit. *EGU General Assembly Conference Abstracts*, **14**, 245

Mankoff KD and Russo TA (2012) The Kinect: A low-cost, high-resolution, short-range, 3D camera. *Earth Surface Processes and Landforms*, **38**(9), 926–936

Mankoff KD, Russo TA and Norris BK (2011) Kinects as sensors in earth science: glaciological, geomorphological, and hydrological applications. *AGU Fall Meeting*

Mathews WH (1964) Water pressure under a glacier. *Journal of Glaciology*, **5**(38), 235–240

McCall JG (1952) The internal structure of a cirque glacier: Report on studies of the englacial movements and temperatures. *Journal of Glaciology*, **2**(12), 122–131

McCall JG (1954) Glacier tunnelling and related observations. *Polar Record*, **7**(48), 120–136

Meierbachtol TW, Harper JT and Humphrey NF (2013) Basal Drainage System Response to Increasing Surface Melt on the Greenland Ice Sheet. *Science*, **341**(6147), 777–779

Messerli A (2015) *Surface velocities and hydrology at Engabreen: Observations from feature tracking and hydro-meteorological measurements*. Ph.D. thesis, University of Copenhaguen

Moore PL (2014) Deformation of debris-ice mixtures. *Reviews of Geophysics*, **52**(3), 435–467

Moore PL, Winberry JP, Iverson NR, Christianson KA, Anandakrishnan S, Jackson M, Mathison ME and Cohen D (2013) Glacier slip and seismicity induced by surface melt. *Geology*, **41**(12), 1247–1250

Murray T and Clarke GKC (1995) Black-box modeling of the subglacial water-system. *Journal of Geophysical Research-Solid Earth*, **100**(B6), 10231–10245

Ng FSL and Hallet B (2002) Patterning mechanisms in subglacial carbonate dissolution and deposition. *Journal of Glaciology*, **48**(162), 386–400

Nicholson LI, Partan B and Petlicki M (2014) Obtaining 3d models of surface snow and ice features (penitentes) with a Xbox Kinect. *EGU General Assembly Conference Abstracts*

Nienow PW, Sharp MJ and Willis IC (1998) Seasonal changes in the morphology of the subglacial drainage system, Haut Glacier d'Arolla, Switzerland. *Earth Surface Processes and Landforms*, **23**(9), 825–843

Niethammer U, James MR, Rothmund S, Travelletti J and Joswig M (2012) UAV-based remote sensing of the Super-Sauze landslide: Evaluation and results. *Engineering Geology*, **128**, 2–11

Nye JF (1953) The flow law of ice from measurements in glacier tunnels, laboratory experiments and the Jungfraufirn borehole experiment. *Proceedings of the Royal Society A: Mathematical, Physical and Engineering Sciences*, **219**(1139), 477–489

Nye JF (1976) Water flow in glaciers: jokulhlaups, tunnels and veins. *Journal of Glaciology*, **17**(76), 181–207

Perutz MF (1950) Direct measurement of the velocity distribution in a vertical profile through a glacier. *Journal of Glaciology*, **1**(7), 382–383

Pimentel S and Flowers GE (2011) A numerical study of hydrologically driven glacier dynamics and subglacial flooding. *Proceedings of the Royal Society A: Mathematical, Physical and Engineering Sciences*, **467**(2126), 537–558

Riesen P (2011) *Variations of the surface ice motion of Gornergletscher during drainages of the ice-dammed lake Gornersee.* Ph.D. thesis, ETH Zürich

Röthlisberger H (1972) Water pressure in intra- and subglacial channels. *Journal of Glaciology*, **11**(62), 177–203

Roux PF, Marsan D, Metaxian JP, O'Brien G and Moreau L (2008) Microseismic activity within a serac zone in an alpine glacier (Glacier d'Argentière, Mont Blanc, France). *Journal of Glaciology*, **54**(184), 157–168

Ryan JC, Hubbard AL, Box JE, Todd J, Christoffersen P, Carr JR, Holt TO and Snooke N (2015) UAV photogrammetry and structure from motion to assess calving dynamics at Store Glacier, a large outlet draining the Greenland ice sheet. *The Cryosphere*, **9**(1), 1–11

Samyn D, Fitzsimons SJ and Lorrain RD (2005) Strain-induced phase changes within cold basal ice from Taylor Glacier, Antarctica, indicated by textural and gas analyses. *Journal of Glaciology*, **51**(175), 611–619

Schoof C (2010) Ice-sheet acceleration driven by melt supply variability. *Nature*, **468**(7325), 803–806

Schoof C, Rada CA, Wilson NJ, Flowers GE and Haseloff M (2014) Oscillatory subglacial drainage in the absence of surface melt. *The Cryosphere*, **8**(3), 959–976

Shreve R (1972) Movement of water in glaciers. *Journal of Glaciology*, **11**(62), 205–214

Shreve RL (1984) Glacier sliding at subfreezing temperatures. *Journal of Glaciology*, **30**(106), 341–347

Snavely N, Seitz SM and Szeliski R (2008) Modeling the world from internet photo collections. *International Journal of Computer Vision*, **80**(2), 189–210

Solgaard AM, Messerli A, Grinsted A, Jackson M, Zwinger T and Dahl-Jensen D (2014) Inferring basal conditions at Engabreen from surface measurements. In *International Symposium on Contribution of Glaciers and Ice Sheets to Sea Level Change, Chamonix, France, 26–30 May 2014*, 1–1

Sørensen H (1955) A petrographical and structural study of the rocks around the peridotite at Engenbræ, Holandsfjord, Northern Norway. . Technical Report 191, NGU

Sugiyama S, Bauder A, Weiss P and Funk M (2007) Reversal of ice motion during the outburst of a glacier-dammed lake on Gornergletscher, Switzerland. *Journal of Glaciology*, **53**(181), 172–180

Sundal AV, Shepherd A, Nienow PW, Hanna E, Palmer S and Huybrechts P (2011) Melt-induced speed-up of Greenland ice sheet offset by efficient subglacial drainage. *Nature*, **469**(7331), 521–524

Theakstone WH (1967) Basal sliding and movement near the margin of the glacier Østerdalsisen, Norway. *Journal of Glaciology*, **6**(48), 805–816

Theakstone WH (1979) Observations within cavities at the bed of the glacier Østerdalsisen, Norway. *Journal of Glaciology*, **23**(89), 273–281

Van Der Veen CJ and Whillans IM (1989) Force Budget: I. Theory and Numerical Methods. *Journal of Glaciology*, **35**(119), 53–60

Vivian R (1997) La mesure de l'érosion des glaciers tempérés: Essai de synthèse/Measuring the erosion of temperate glaciers: a synthesis. *Revue de Géographie Alpine*, **85**(1), 9–32

Vivian R and Bocquet G (1973) Subglacial cavitation phenomena under the glacier d'Argentière. *Journal of Glaciology*, **12**(66), 439–451

Wachs JP, Kölsch M, Stern H and Edan Y (2011) Vision-based hand-gesture applications. *Communications of the ACM*, **54**(2), 60–71

Waeber M (1944) Observations faites au glacier de Tré-la-Tête à l'occasion d'une prise d'eau sous-glaciaire. *Géologie Alpine*, **24**(3), 1–25

Weertman J (1957) On the sliding of glaciers. *Journal of Glaciology*, **3**(21), 33–38

Weertman J (1972) General theory of water flow at the base of a glacier or ice sheet. *Reviews of Geophysics*, **10**(1), 287–333

Werder MA, Hewitt IJ, Schoof C and Flowers GE (2013) Modeling channelized and distributed subglacial drainage in two dimensions. *Journal Of Geophysical Research-Earth Surface*, **118**(4), 2140–2158

Westoby MJ, Brasington J, Glasser NF, Hambrey MJ and Reynolds JM (2012) 'Structure-from-Motion' photogrammetry: A low-cost, effective tool for geoscience applications. *Geomorphology*, **179**, 300–314

Winsvold SH, Andreassen LM and Kienholz C (2014) Glacier area and length changes in Norway from repeat inventories. *The Cryosphere*, **8**(5), 1885–1903

Wold B and Østrem G (1979) Morphological activity of a diverted glacier stream in Western Norway. *GeoJournal*, **3**(4), 345–349

Wu C (2011) VisualSFM: A visual structure from motion system

Zryd A (1991) *Conditions dans la couche basale des glaciers tempérés: contraintes, teneur en eau et frottement intérieur*. Ph.D. thesis, ETH Zurich

Part II

Journal Publications

Part III

Appendices

A Map of the SSL

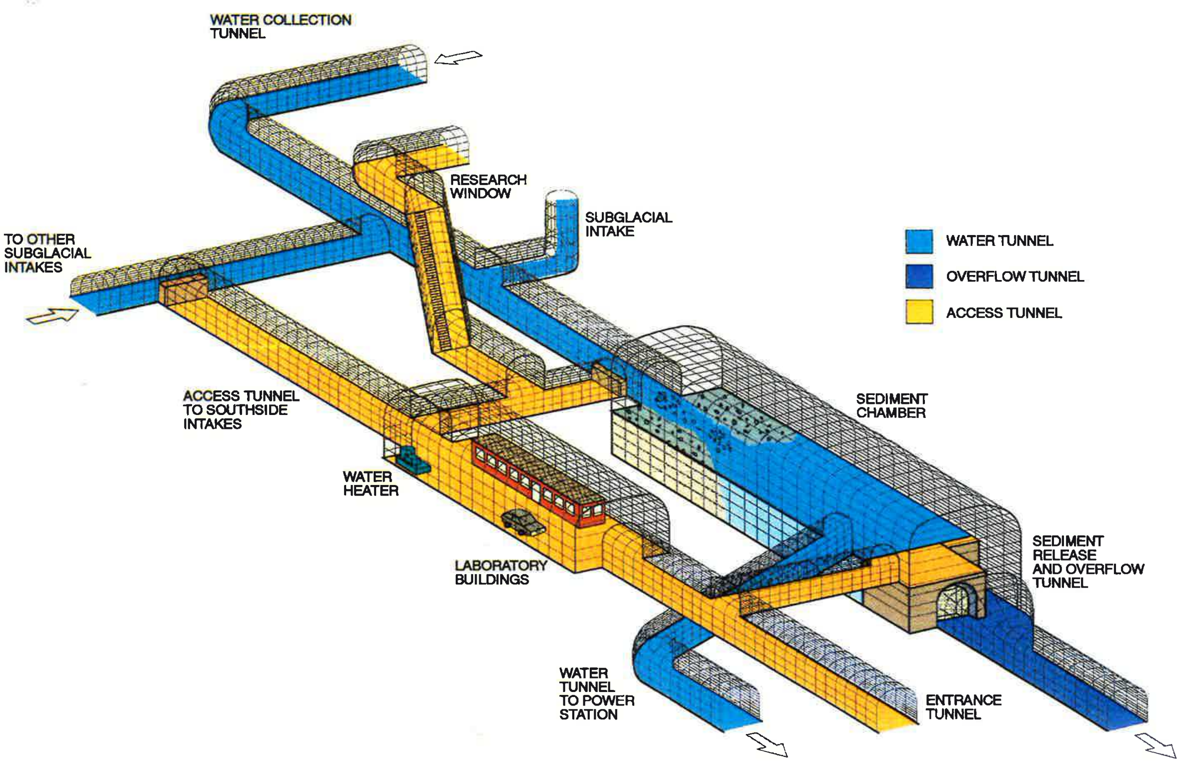
WATER COLLECTION TUNNEL
RESEARCH WINDOW
SUBGLACIAL INTAKE
TO OTHER SUBGLACIAL INTAKES
WATER TUNNEL
OVERFLOW TUNNEL
ACCESS TUNNEL
ACCESS TUNNEL TO SOUTHSIDE INTAKES
SEDIMENT CHAMBER
WATER HEATER
SEDIMENT RELEASE AND OVERFLOW TUNNEL
LABORATORY BUILDINGS
WATER TUNNEL TO POWER STATION
ENTRANCE TUNNEL

Figure A.1: Map-Sketch of the Svartisen Subglacial Laboratory and research shaft (credits: NVE).

B Data Overview

Figure of the data overview is on the next page.

B Data Overview

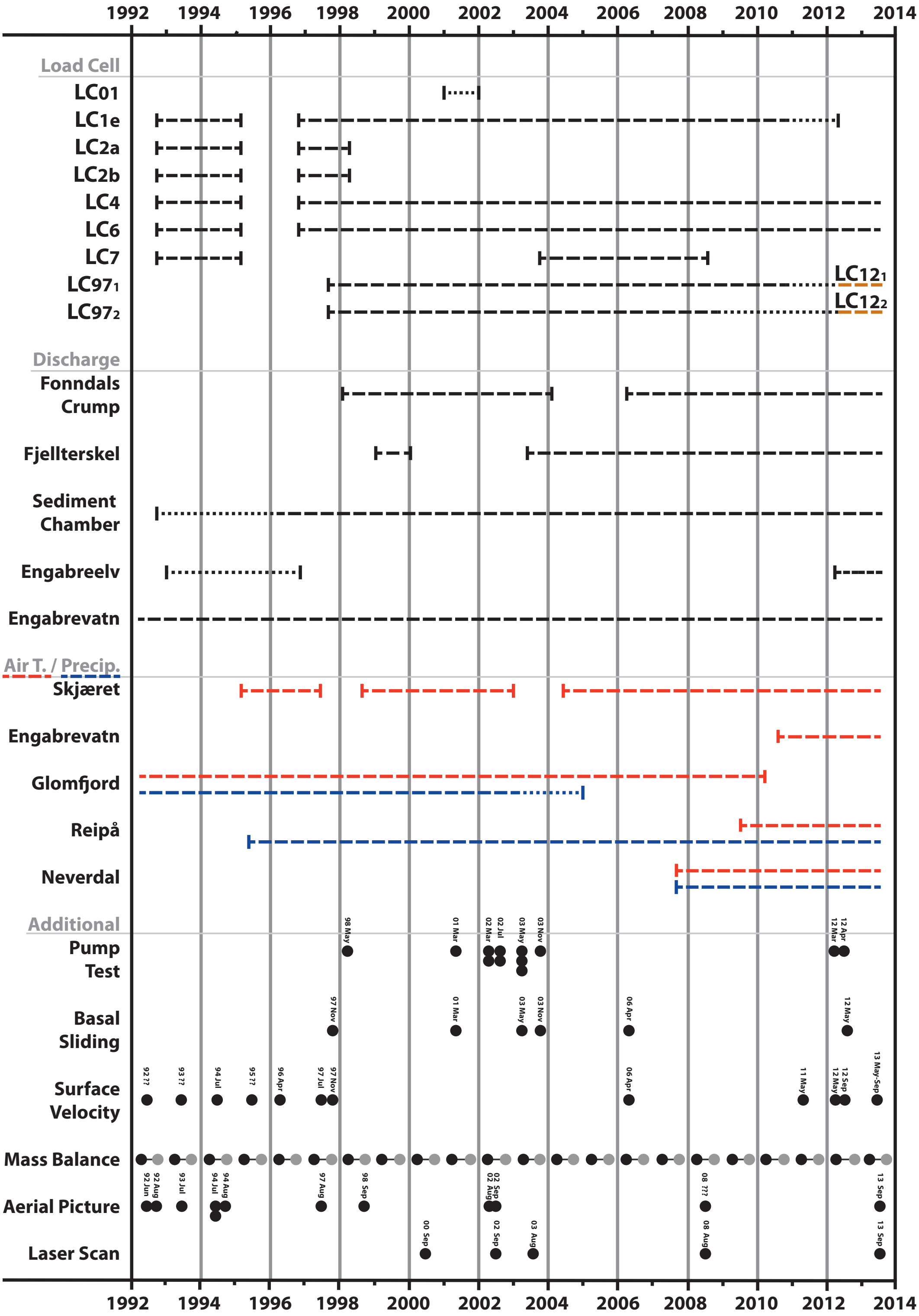

Figure B.1: Overview of pressure data, hydro-meteorological data and surface measurements.

C Pressure Events

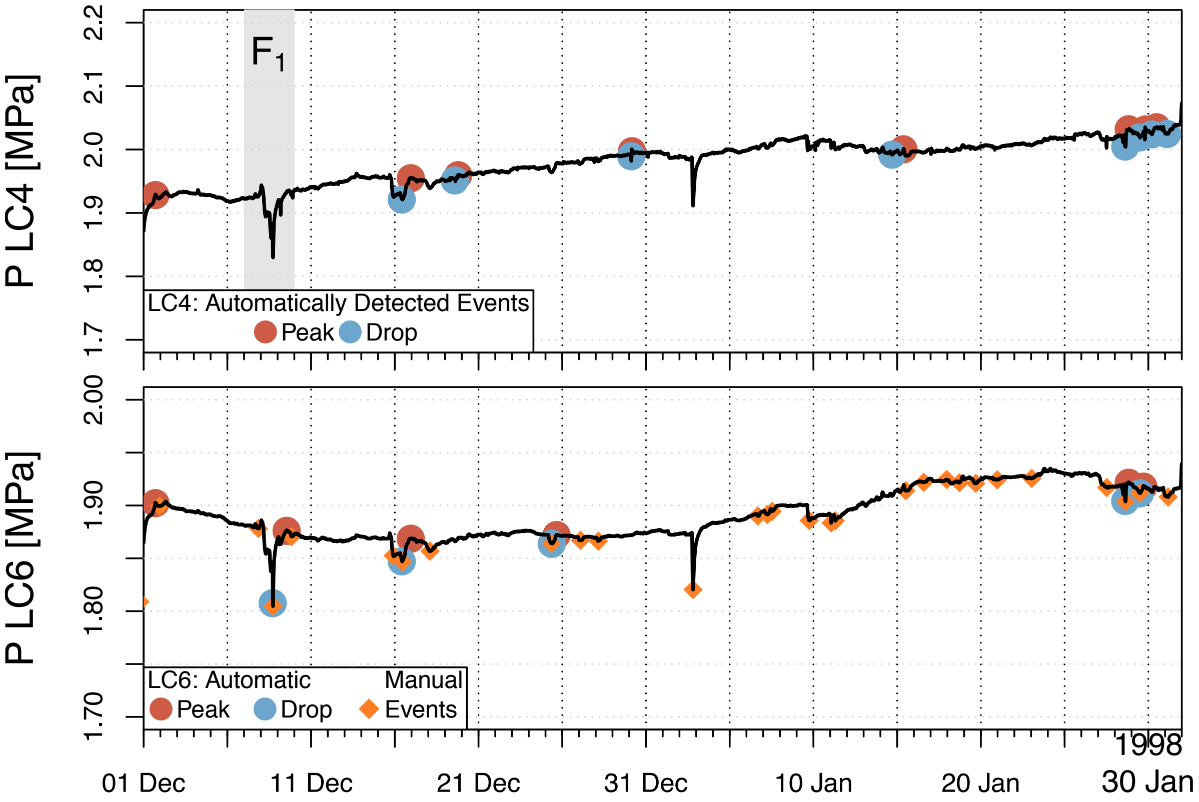

Figure C.1: Pressure events identified using the automatic detection method for LC4 (top) and LC6 (bottom) for a two month period in winter 1998. The manual method was applied to LC6 only (diamond). The automatic method discards the smallest events and fails to identify the event F_1 due to the noise in the pressure data.

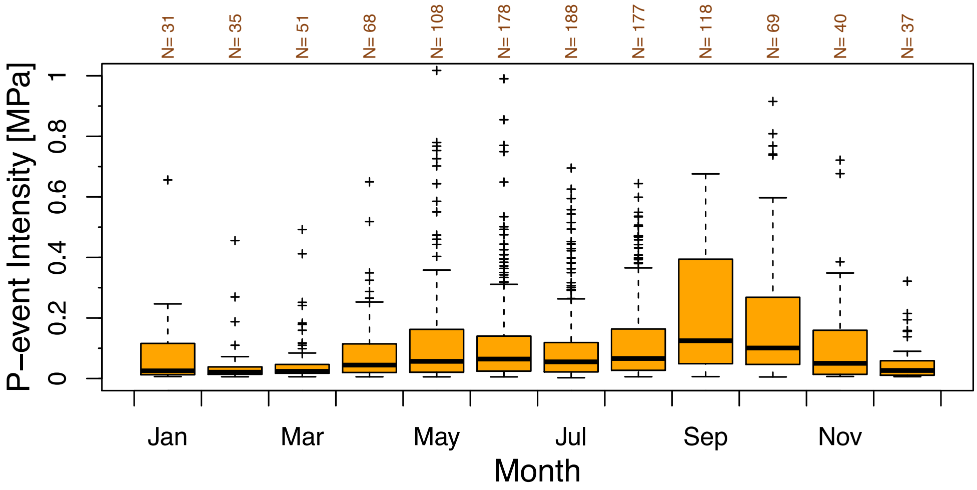

Figure C.2: Monthly distribution of the intensity of pressure events at LC4 obtained from the difference between the minima and maxima of pressure events over the entire measurement period 1993-2014.

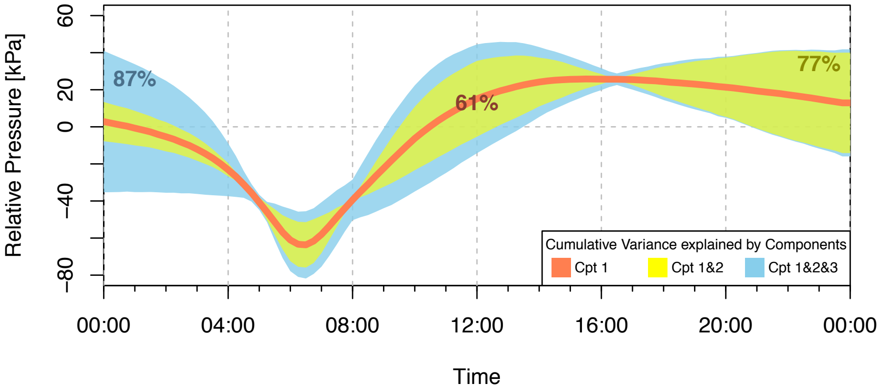

Figure C.3: Envelope of variance explained by the first three components of the principal component analysis based on 795 daily pressure events automatically identified in **LC4** records between 1993 and 2014. The studied time window for the pressure events is defined by the time of the minima, starting 6 hours earlier and ending 12 hours later. The start in time is set to 12:00 in order to fit the timing of the drop as found in figures 4.4b and 4.4d.

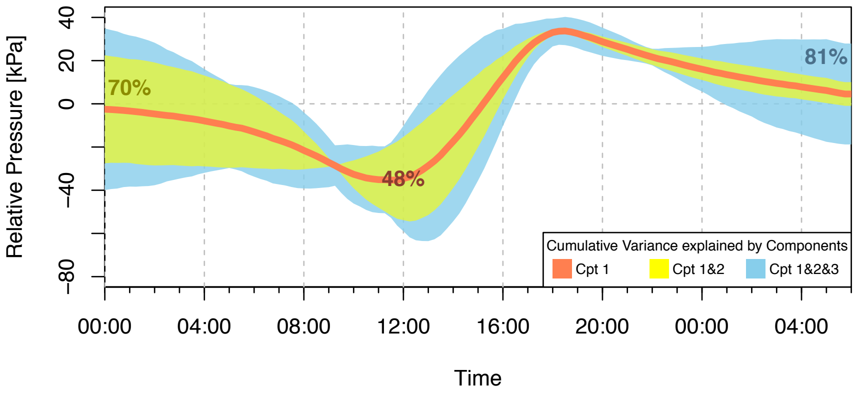

Figure C.4: Envelope of variance explained by the first three components of the principal component analysis based on 795 daily pressure events automatically identified in LC6 records between 1993 and 2014. The studied time window for the pressure events is defined by the time of the maxima, starting 18 hours earlier and ending 12 hours later. The start in time is set to 12:00 in order to fit the timing of the peak as found in figures 4.4c and 4.4e.

D Spring Melt Events

Year	Start	End	Days
1993	16-May	21-May	5
1994	26-Apr	28-Apr	2
1994	07-May	12-May	5
1995	-	-	-
1996	-	-	-
1997	09-May	14-May	5
1997	15-May	18-May	3
1997	02-Jun	03-Jun	1
1997	06-Jun	08-Jun	2
1998	15-May	21-May	6
1998	04-Jun	11-Jun	7
1998	14-Jun	20-Jun	6
1999	-	-	-
2000	-	-	-
2001	30-May	11-Jun	12
2002	22-Apr	25-Apr	3
2002	08-May	14-May	6
2003	12-May	21-May	9
2004	19-Apr	23-Apr	5
2004	04-May	09-May	2
2005	04-May	09-May	5
2005	04-Jun	13-Jun	-
2006	26-Apr	07-May	-
2007	14-Apr	19-Apr	5
2007	26-Apr	07-May	3
2007	19-May	22-May	1
2008	30-Apr	05-May	2
2009	25-Apr	01-May	6
2009	15-May	23-May	7
2010	14-May	20-May	6
2011	10-May	13-May	-
2011	02-Jun	08-Jun	-
2012	24-May	27-May	12
2012	04-Jun	07-Jun	3
2012	16-Jun	25-Jun	6
2013	11-May	20-May	9

Table D.1: Duration of Pressure events associated with Spring melt events between 1993 and 2013. A year may contain several high intensity pressure events between April and June that show response similar to the main spring melt event.

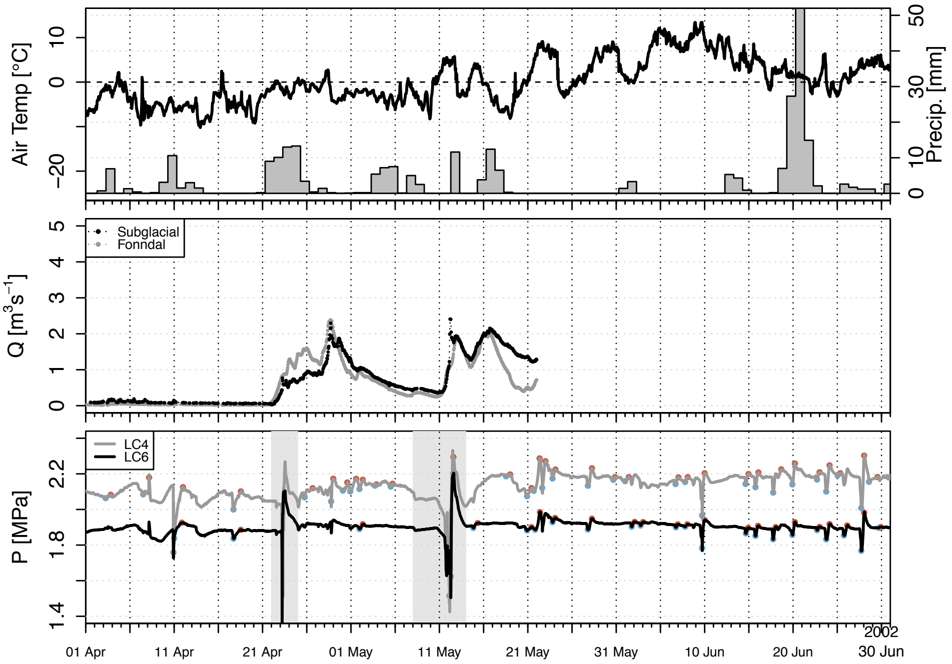

Figure D.1: Spring Melt event in 2002 with air temperature from Skjæret station, precipitation from Glomfjord station, discharge data and pressure data.

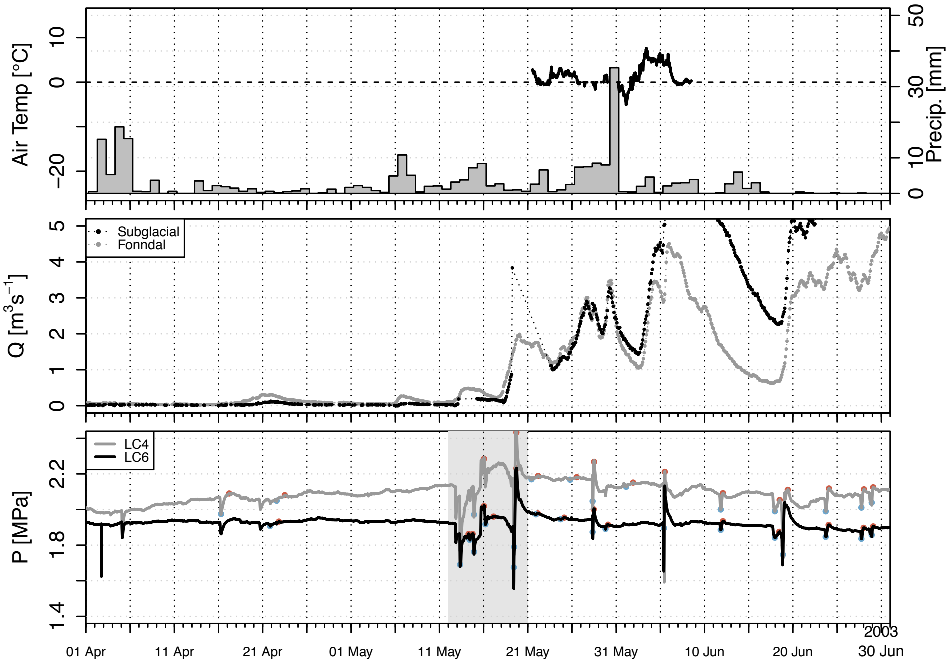

Figure D.2: Spring Melt event in 2003 with same data as figure D.1.

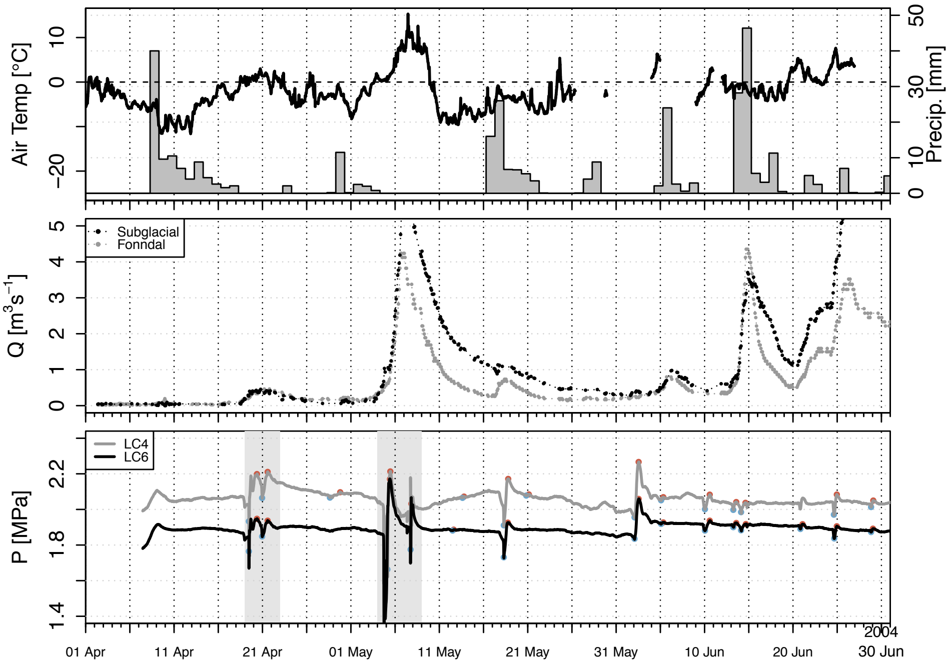

Figure D.3: Spring Melt event in 2004 with air temperature from Skjæret station, precipitation from Reipå station, discharge data and pressure data.

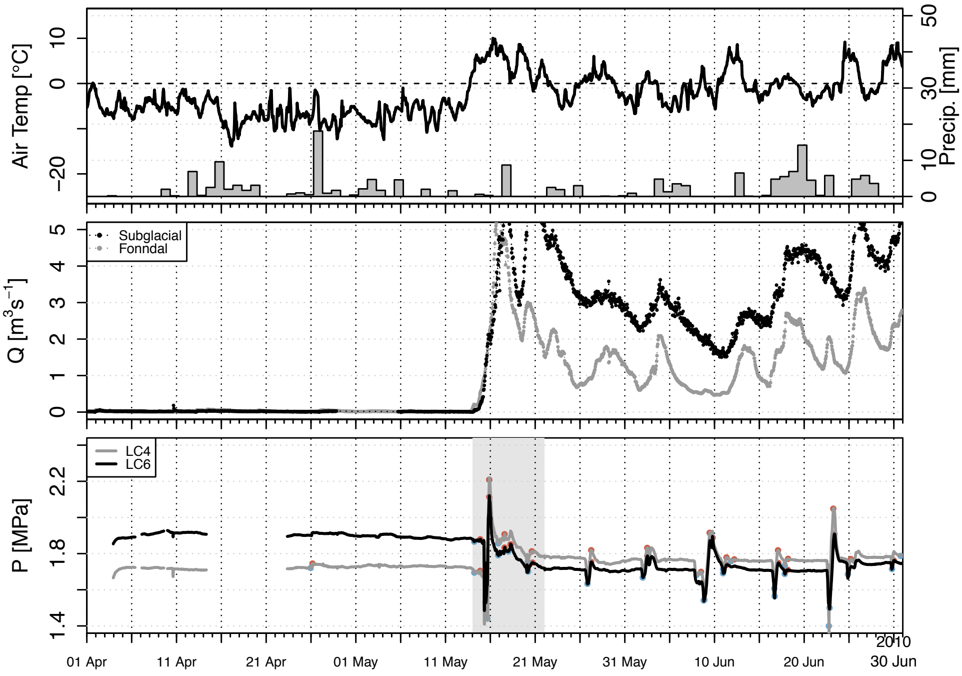

Figure D.4: Spring Melt event in 2010 with same data as figure D.3.

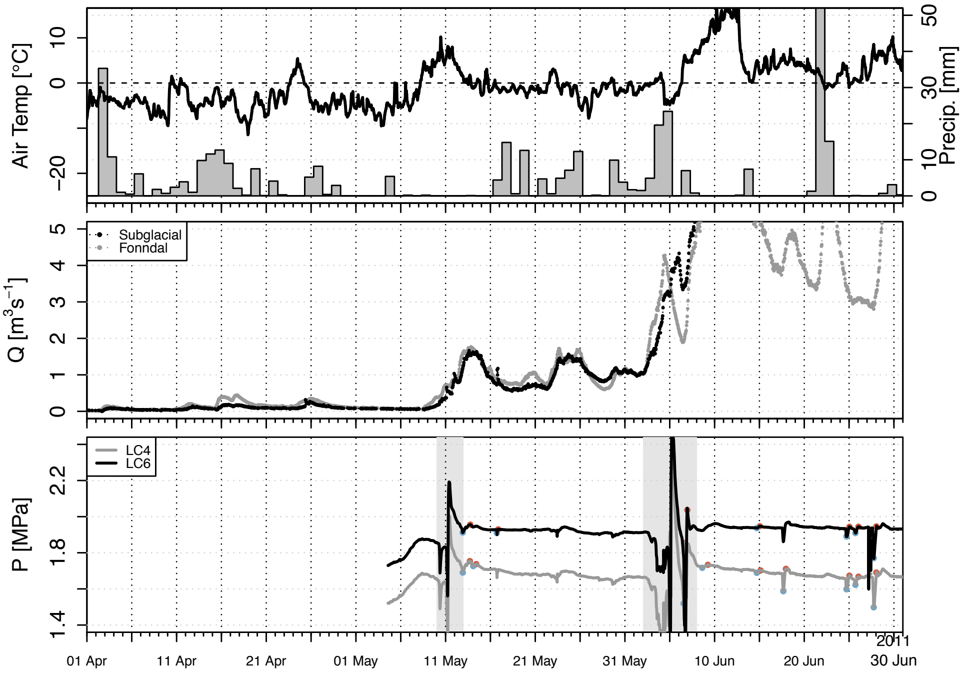

Figure D.5: Spring Melt event in 2011 with same data as figure D.3.

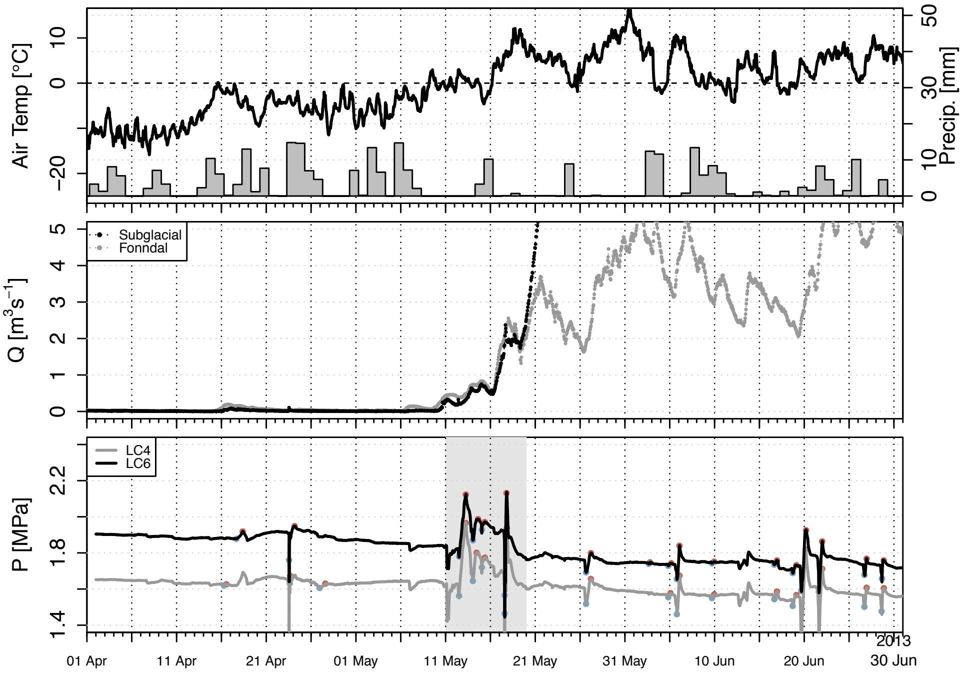

Figure D.6: Spring Melt event in 2013 with same data as figure D.3.

E Mapping Bedrock

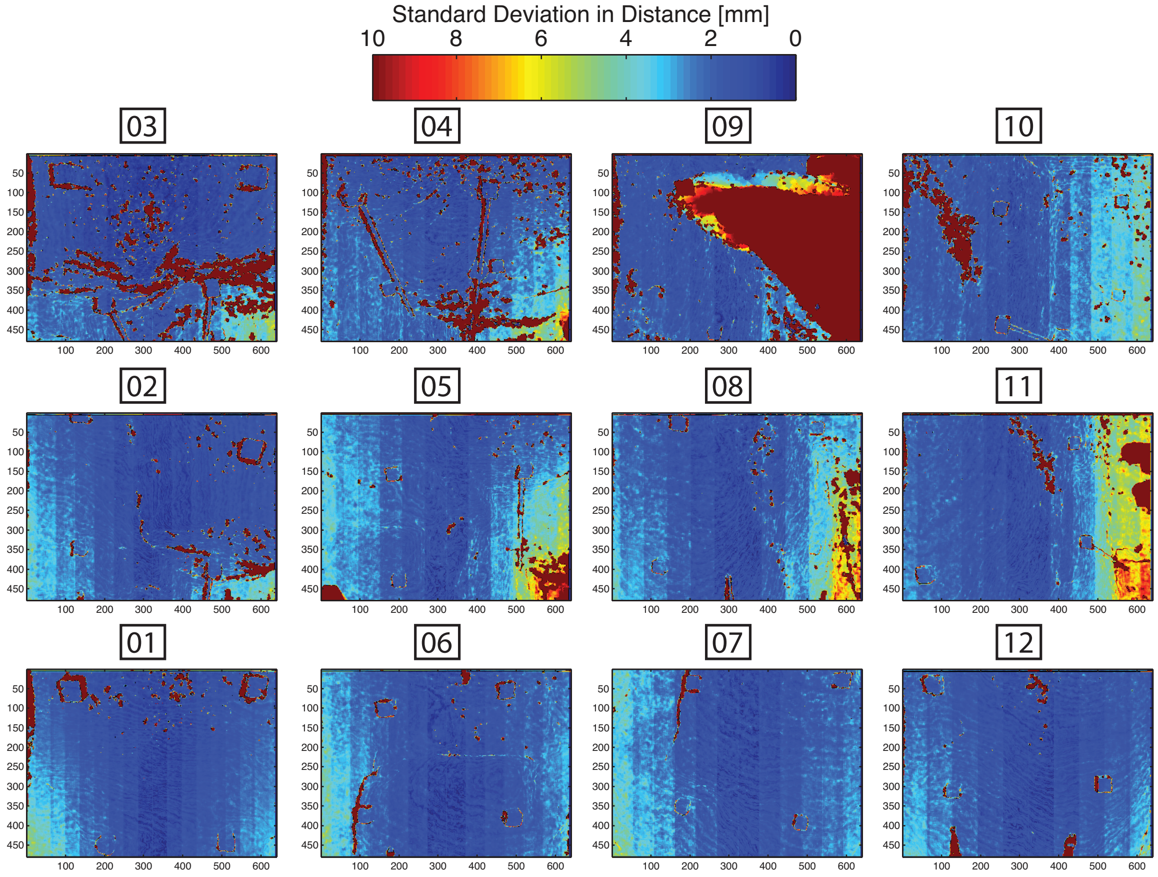

Figure E.1: Samples of standard deviation computed for 1600 images at each different sub-set near the load cell LC97_1. The location of each numbered map is indicated in figure 5.4.

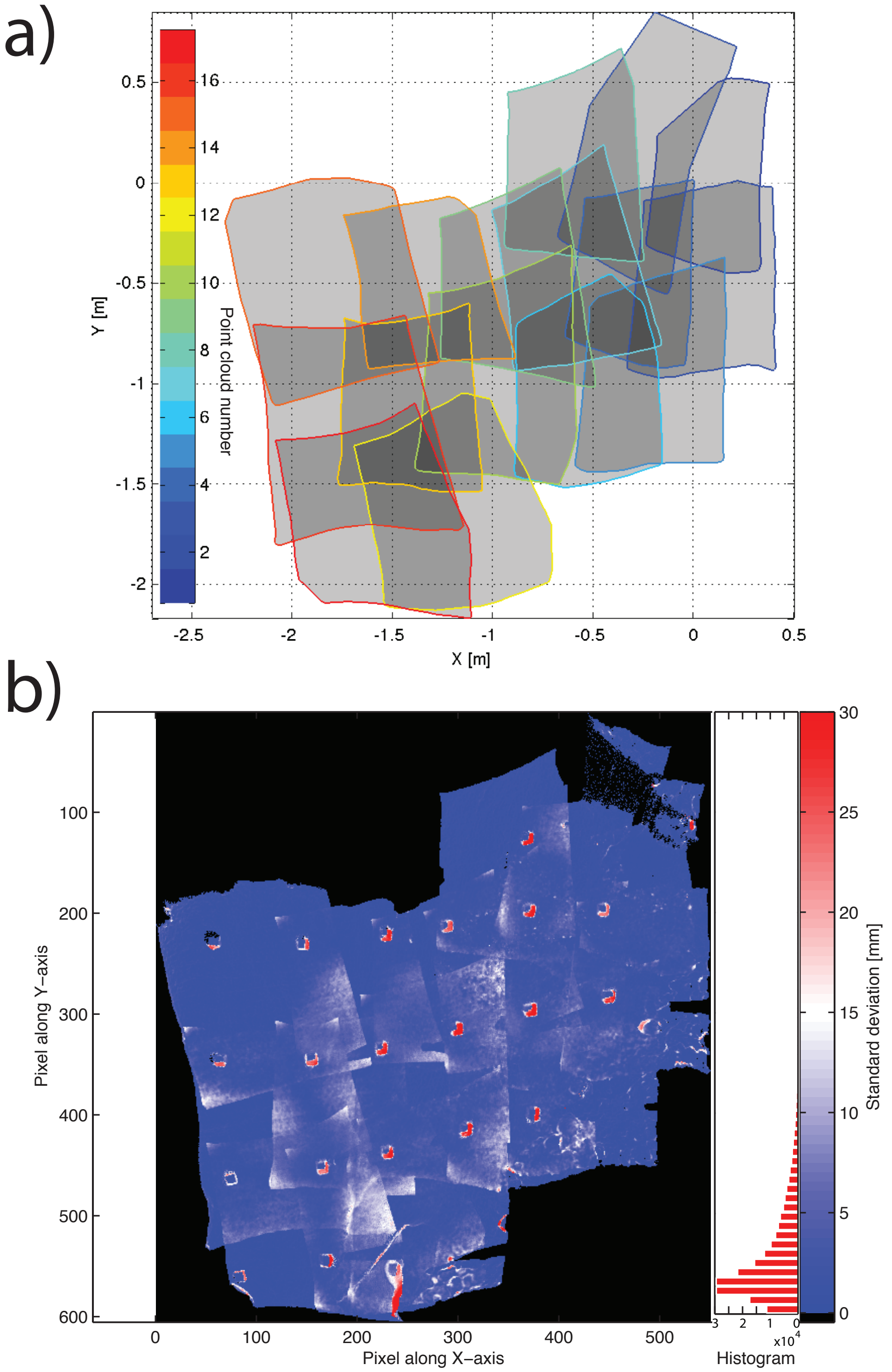

Figure E.2: Effect of aligning Kinect tiles on non-propagated elevation errors for the area close to LC1e. a) Outline of each mapped sub-set. The covered areas are shaded and transparent. Darkening of the map indicates an increase in point density. b) Standard deviation computed from a 5 mm radius moving sphere.

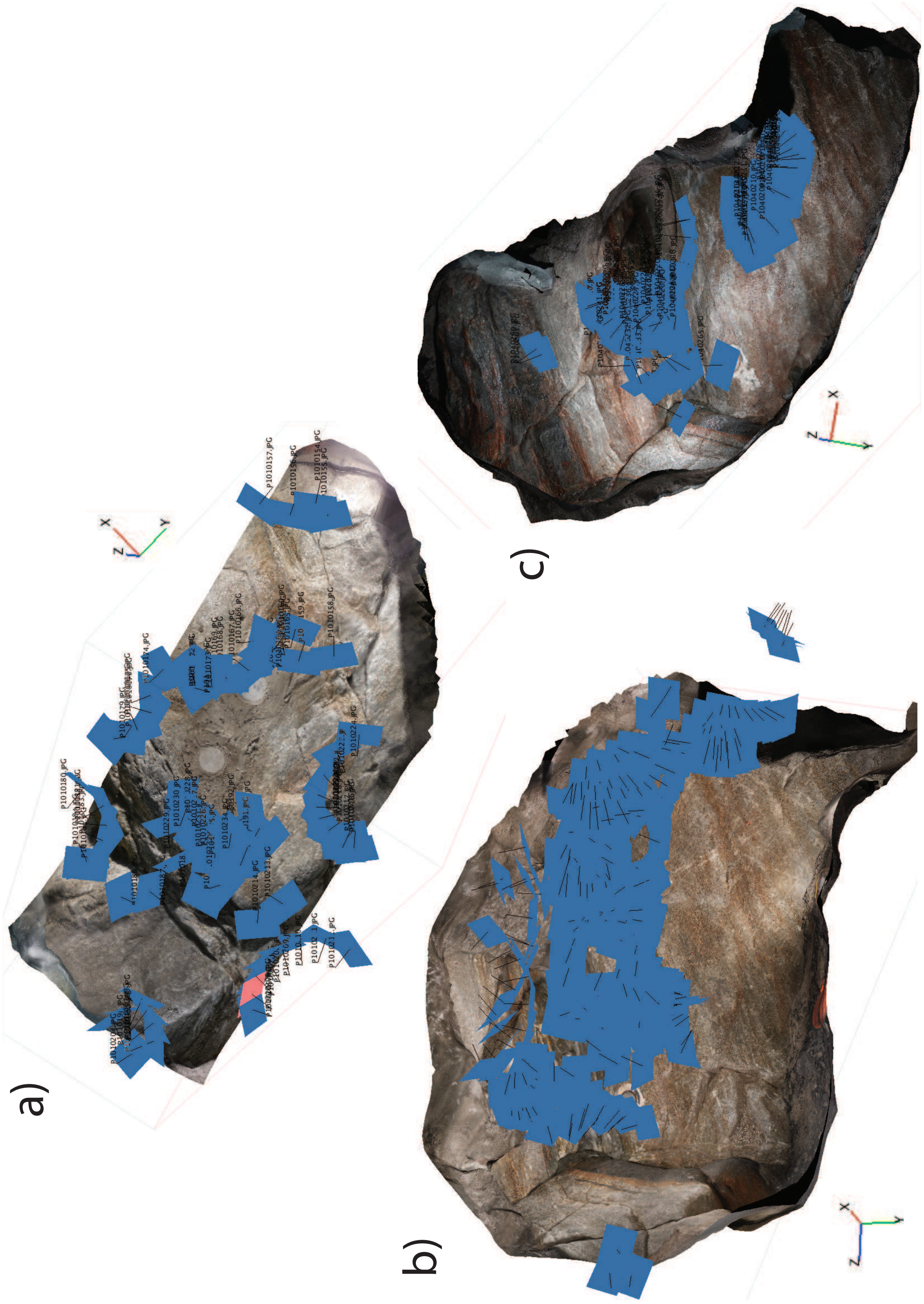

Figure E.3: Location and orientation of camera poses for each SFM produced point cloud: a) LC97 map (82 images), b) LC1e map from the 2012 campaign (69 images) and c) LC1e map from the 2013 campaign (240 images)

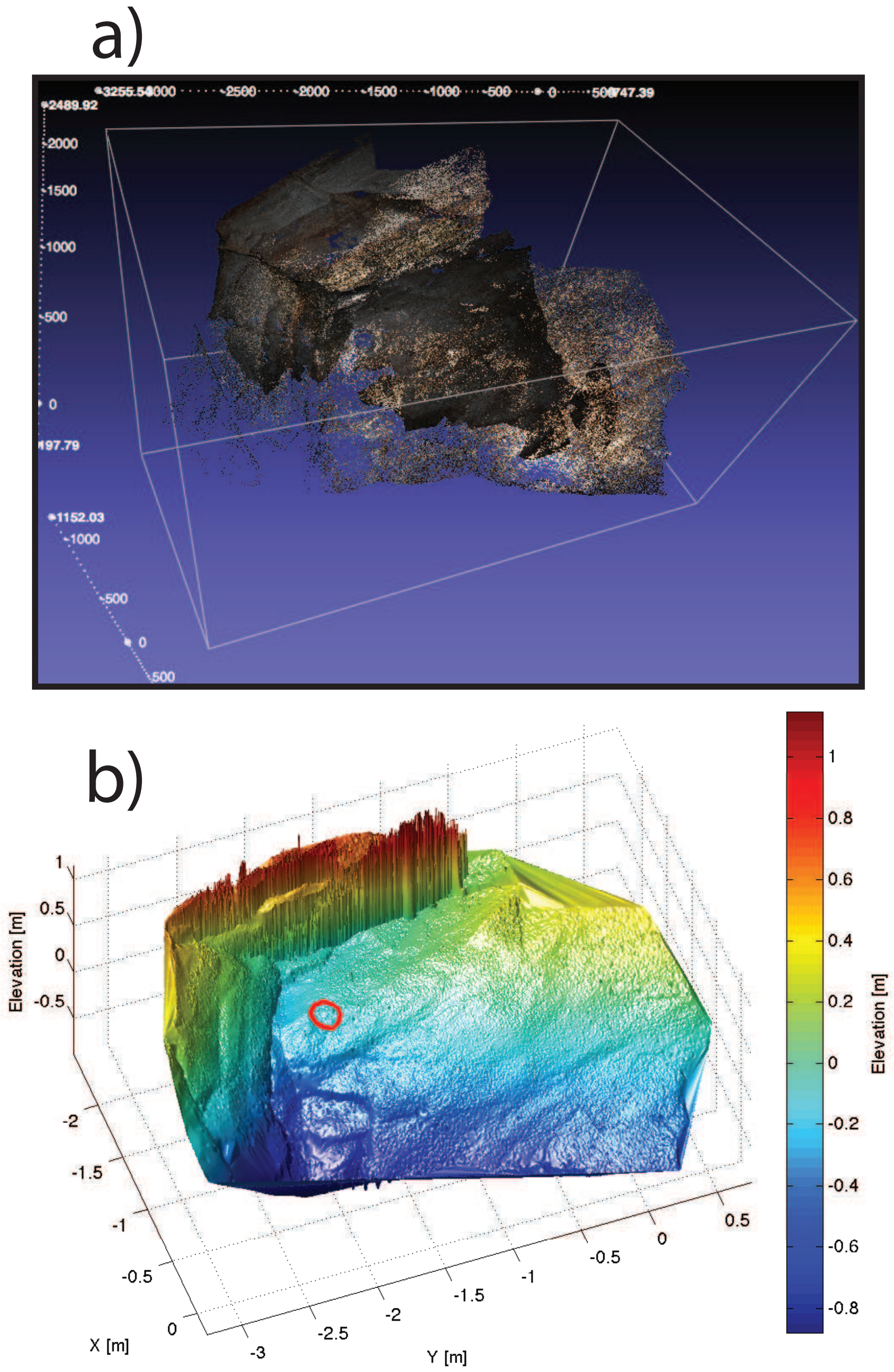
a)
3255.54000
2500
2000
1500
1000
500
0
500747.39
2489.92
2000
1500
1000
500
0
97.79
1152.03
1000
500
0
500
b)
Elevation [m]
1
0.5
0
-0.5
-2
-1.5
-1
-0.5
0
X [m]
-3
-2.5
-2
-1.5
-1
-0.5
0
0.5
Y [m]
1
0.8
0.6
0.4
0.2
0
-0.2
-0.4
-0.6
-0.8
Elevation [m]

Figure E.4: Results of the SfM method near the load cells LC1e (circle) presenting the referenced and scaled point clouds. The campaigns conducted in 2012 and 2013 are merged to produce the above figures. 3D view of a) the two overlaid point clouds with RGB values and b) the obtained elevation map (errors are due to processing problems and dealing with a 3D structure in a vertical wall).

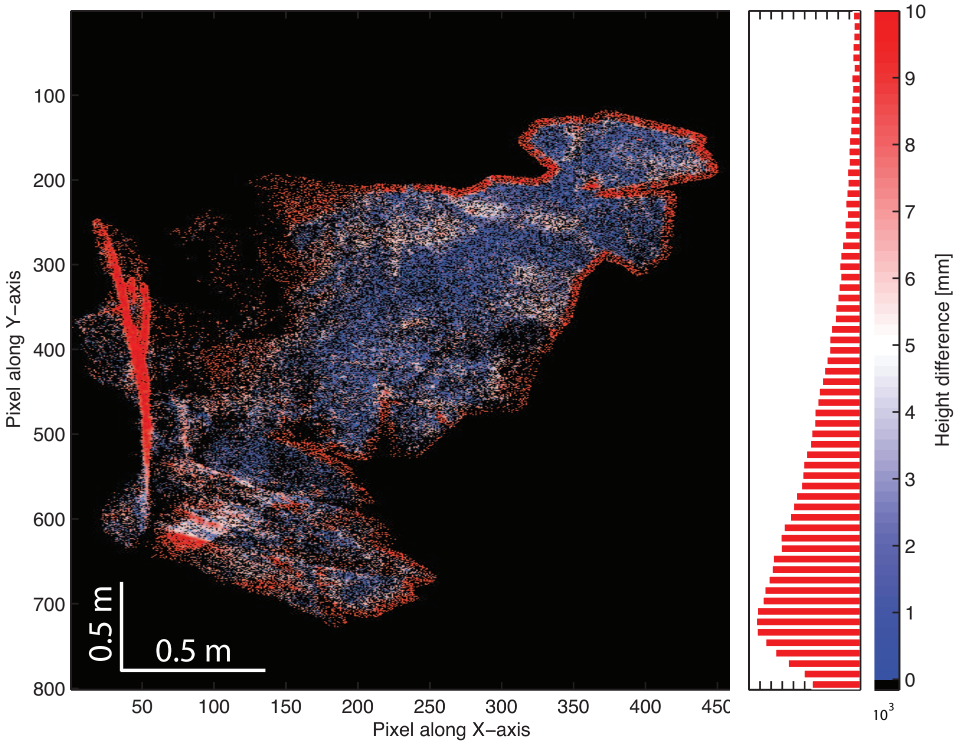

Figure E.5: Difference in absolute height (millimetre) for the two SFM point cloud surrounding LC1e that were collected a year apart (April 2012 and April 2013). Axes are not equal for plotting purposes.

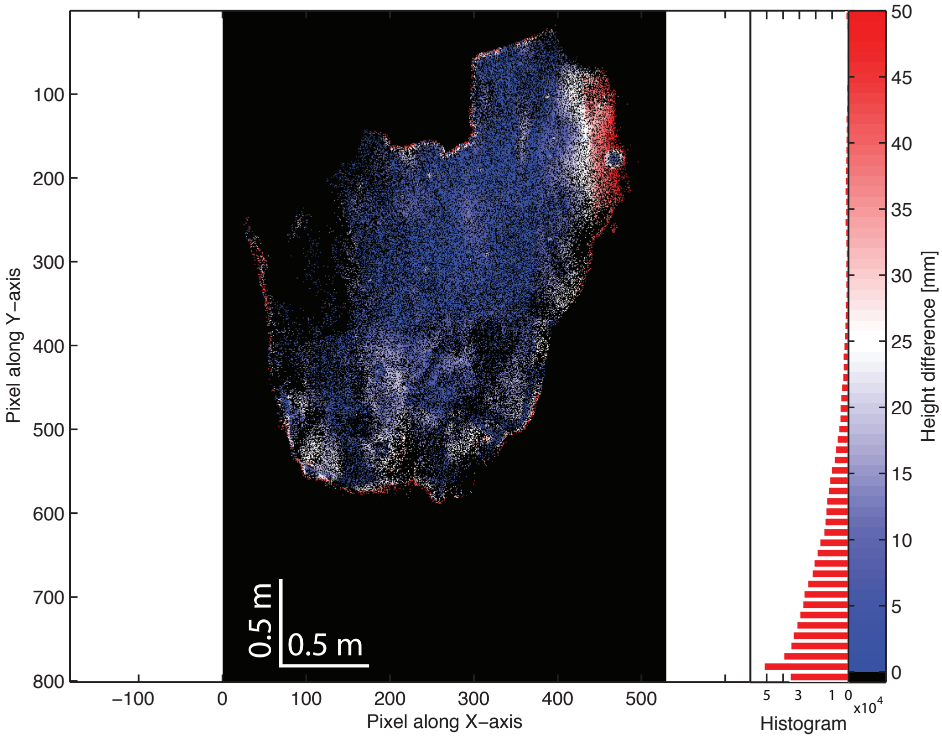

Figure E.6: Absolute height difference between the reference Kinect map and SFM point cloud (data collected in 2013) near the load cell LC1e.

F Cavity Closure and Stress Bridging

Date Start	Date End	Mean	Median	Q25	Q75
13/11 14:25	13/11 17:00	19.14	19.24	14.69	23.83
13/11 17:00	13/11 23:57	19.12	19.11	16.09	22.23
13/11 23:57	14/11 09:10	20.64	20.67	17.45	23.78
14/11 09:10	14/11 11:58	19.1	19.01	14.9	23.18
14/11 11:58	14/11 14:57	20.54	20.51	16.81	24.2
14/11 14:57	14/11 18:10	20.47	20.54	17.09	23.98
14/11 18:10	14/11 21:21	20.8	20.82	17.66	24.06
14/11 21:21	14/11 23:00	20.41	20.42	170.2	24.03

Table F.1: Kinect measurements of closure rate given in cm.day^{-1} for the period 13-14 November 2012. The mean, median, 25% quartile, 75% quartile and standard deviation are computed from the distribution in closure rate between start and end date.

Date Start	Distance	Date End	Closure Rate
13/11 10:10	162.2	14/11 17:25	50.3
14/11 17:25	147.0	14/11 21:25	54.0
14/11 21:25	138.0		

Table F.2: Closure rate measurements in cm.day^{-1} obtained from the distance between two markers screwed on each side of the cavity (in cm) for the period 13-14 November 2012.

Date Start	Manual	ICP	Day End	Mean	Q25	Median	Q75
15/11 16:50	10.81	3.13	15/11 18:01	54.70	34.74	15.51	66.04
15/11 18:01	11.44	3.49	15/11 19:14	18.31	14.92	6.98	26.45
15/11 19:14	Ref.	Ref.	15/11 20:03	22.27	23.31	14.56	28.42
15/11 20:03		3.26	15/11 21:00	24.70	24.02	19.63	29.73
15/11 21:00		2.12	16/11 00:01	27.54	28.26	24.23	31.58
16/11 00:01		2.07	16/11 09:24	30.00	30.92	27.14	33.61
16/11 09:24		1.85	16/11 12:00	27.36	28.40	24.42	31.59
16/11 12:00		1.48	16/11 15:15	28.08	29.62	24.86	32.79
16/11 15:15		1.41	16/11 18:05	92.84	93.77	54.15	128.24

Table F.3: Details of the Kinect measurements of closure rate (cm.day^{-1}) for the period 15-16 November 2012. The root mean squares (mm) of the manual and Iterative Closest Point (ICP) alignment assess the uncertainty in the registration between bedrock from each collected epoch and the bedrock of reference (Ref.: 15/11/2012 19:14). The absolute displacement rate is computed between two Kinect point clouds from the start date and end date. The obtained distribution of closure rate gives the above mean, median, 25% quartile, 75% quartile and standard deviation.

Date Start	Distance	Date End	Closure Rate
15/11 16:30	239.2	15/11 18:25	61.4
15/11 18:25	234.3	15/11 19:20	55.0
15/11 19:20	232.2	15/11 20:11	53.7
15/11 20:11	230.3	15/11 21:07	48.9
15/11 21:07	228.4	16/11 00:10	53.5
16/11 00:10	221.6	16/11 09:44	51.9
16/11 09:44	200.9	16/11 12:10	48.3
16/11 12:10	196.0	16/11 15:22	45.0
16/11 15:22	190.0	16/11 19:15	55.0
16/11 19:15	181.1		

Table F.4: Closure rates calculated from the distance of markers drilled into the ice (Fig. 6.2). The data are given in cm and cm.day^{-1} for the period 15-16 November 2012.

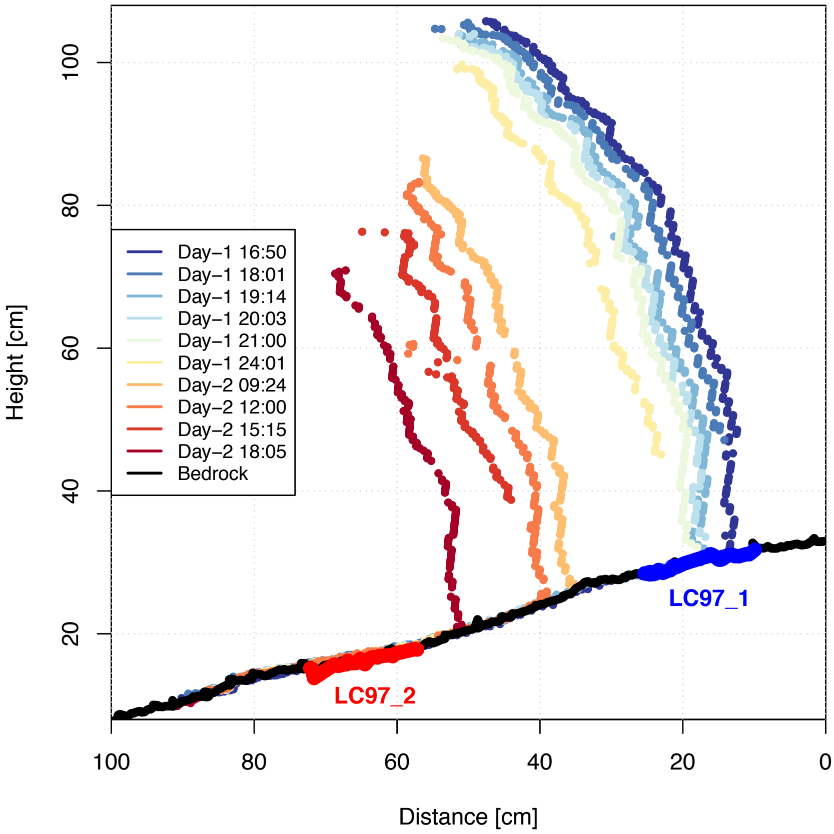

Figure F.1: Temporal variation in cross-section of the 15-16 Nov. cavity (Day 1 and 2) as measured by the Kinect on the same line as in figure 6.6, parallel to the sliding direction.